Universidad de Concepción
Dirección de Postgrado
Facultad de Ciencias Físicas y Matemáticas
Programa de Doctorado en Ciencias Físicas

Estudiando los procesos de alimentación y retro-alimentación en galaxias activas cercanas
(Probing the feeding and feedback processes in nearby active galaxies)

Tesis presentada a la Facultad de Ciencias Físicas y Matemáticas de la
Universidad de Concepción
para optar al grado académico de Doctor en Ciencias Físicas

Carolina Elizabeth Finlez Ruiz
CONCEPCIÓN-CHILE
Julio 2019

Profesor Guía: Neil Nagar
Dpto. de Astronomía, Facultad de Ciencias Físicas y Matemáticas
Universidad de Concepción

Resumen

La presencia ubicua de agujeros negros supermasivos (SMBH, por sus siglas en inglés) en el centro de la mayoría de la galaxias con un componente de bulbo, y las correlaciones observadas entre el SMBH y las propiedades de su galaxia-anfitrión, indica una conexión y posible co-evolución entre el SMBH y su galaxia-anfitrión.

El estudio de los procesos que llevan la evolución del SMBH y su efecto en la galaxia es un tema importante en el estudio de la evolución de galaxias. La retro-alimentación ha sido sugerida usualmente como el proceso que lleva la co-evolución, ya que la energía liberada por el SMBH en la galaxia puede calentar y remover gas de la galaxia, regulando el crecimiento y la formación estelar en la galaxia. El proceso de alimentación precede al de retro-alimentación. El nivel de actividad nuclear dependerá de la disponibilidad de gas para alimentar al SMBH. El gas debe caer desde la galaxia a gran escala hasta la región central, para lo cual debe perder todo su momento angular. Interacciones entre galaxias y potenciales no-axisimétricos son algunos de los mecanismos posibles que pueden transportar gas hacia la región central.

Un método para estudiar los procesos de alimentación y retro-alimentación es buscar por flujos de gas hacia el centro o gas expulsado desde el centro, ya que estas pueden ser señales de la presencia de alimentación o retro-alimentación, respectivamente. Herramientas actuales como espectroscopía integral de campo e interferometría de ALMA pueden entregar observaciones de alta resolución que nos permiten estudiar estos procesos en gran detalle.

En este trabajo presentamos observaciones de GMOS/IFU y ALMA en dos galaxias activas cercanas. Estos datos nos permiten estudiar la cinemática de la región cntral del gas molecular e ionizdo en estas galaxias con gran detalle. Observamos la presencia de flujos de gas expulsados desde el centro y las posibles firmas cinemáticas de barras estelares en la región central de estas galaxias. Mostramos que la región nuclear the galaxias activas puede ser un ambiente complejo y multi-fase, donde las señales de alimentación y retro-alimentación pueden ocurrir de manera simultánea y por lo tanto mostrar una cinemática compleja. Para desentrañar y entender estos procesos necesitamos construir una base de estudios de galaxias en gran detalle, lo que sólo se puede lograr en galaxias cercanas debido a la sensibilidad y resolución que este tipo de análisis requiere. En esta tesis presentamos dos casos de estudio en alto detalle de galaxias activas cercanas con cinemática compleja en el centro.

Dissertation Advisor: Neil Nagar Carolina Elizabeth Finlez Ruiz

Probing the Feeding and Feedback process in Nearby Active Galaxies

Abstract

The ubiquitious presence of a super massive black hole (SMBH) at the centre of most galaxies with a bulge component and the observed correlations between the SMBH mass and its host galaxy properties indicate the connection and possible co-evolution between the SMBH and its host galaxy.

The study of the processes that lead the evolution of the SMBH and the effect it has on the host galaxy is an important topic in galaxy evolution. Feedback has often been suggested as the process leading the co-evolution as the energy released by the SMBH into the host galaxy can heat and remove gas from the galaxy, regulating the growth and the star formation in the galaxy. Feeding precedes the feedback process, the level of nuclear activity will depend of the availability of gas to feed the SMBH. The gas supply must fall from the large-scale of the galaxy into the centre, for which it must loose all of its angular momentum. Galaxy interactions and non-axysimmetric potentials are some of the possible mechanisms that can drive gas to the central region.

A method to study the feeding and feedback processes is to search for inflows and outflows in the central region of active galaxies, as this can be the signatures of ongoing feeding and feedback respectively. Currently tools such as integral field spectroscopy (IFS) and interferometry from ALMA can provide high resolution observations that allow us to study these processes in detail.

In this work we present high resolution GMOS/IFU and ALMA observations of two nearby active galaxies. This datasets allow us to study the kinematics of the central region of the molecular and ionized gas in these galaxies at great detail. We observe the presence of outflows and the possible kinematical signatures of stellar bars in the central region of these galaxies. We show that the nuclear region of active galaxies can be a complex multi-phase environment, where signatures of feeding and feedback can occur simultaneously and thus present complex kinematics.

To disentangle and understand these processes we need to build up detailed studies of galaxies, this can only be achieved in nearby galaxies because of the sensitivity and resolution required to analyse the kinematics in detail. In this thesis we present two detailed case studies of nearby active galaxies with complex central kinematics.

List of Figures

3

Acknowledgments

To my advisor, Neil, for your endless patience and good disposition and for all the amazing opportunities that enriched my life beyond what I thought was possible. From all the lessons I learned from you, and they were plenty, the one I will always keep with me is that kindness goes a long way. And finally for believing in me all these years when I was not able to believe in myself.

A mi familia por su apoyo incondicional, por estar ahí para mi siempre, por guiarme y entregarme los valores que siempre llevo conmigo. Espero algún día poder llegar a ser una persona digna de todo el esfuerzo que han hecho por mi. Los quiero muchísimo.

A la Marce por las incontables horas de conversación, una década entera!, tu corazón y tu mente son inigualables y ha sido un inmenso privilegio contar con tu amistad.

A todas las hermosas mujeres que me ensearon la belleza del arte, el feminismo y la sororidad, las adoro.

Y finalmente, a mi persona favorita, Felipe, por tu infinita paciencia y tu apoyo constante durante todos estos años, tu compañía lo es todo para mi, realmente no hay palabras para contener todo mi amor y agradecimiento.

El desarrollo de esta tesis ha sido financiado por la Comisión Nacional de Investigación Científica y Tecnológica mediante el proyecto CONICYT-PCHA/Doctorado Nacional/2015-21151141.

Contents

Chapter 1

Introduction

1.1 Galaxy evolution

A major goal in modern astrophysics is the understanding of the formation and evolution of galaxies. Galaxies can be classified and studied over a large range of different physical properties, such as luminosity, morphologies, colours, kinematics, etc.

Edwin Hubble created the first classification of galaxies, based on their morphologies in 1936. This classification scheme divides the galaxies into three main groups: ellipticals, normal spirals and barred spirals. These categories form the so called Hubble's tuning-fork diagram or Hubble sequence (Fig. 1.1). This diagram is now modified to include irregular galaxies as well.

Based on this diagram Hubble suggested that this classification showed an evolutionary sequence and thus identified the galaxies from 'early type' (starting from right to left) to 'late' type. Currently we know this not to be the case, and Hubble sequence is only a morphological classification.

Spiral galaxies contain a large amount of gas in their arms which usually leads to the formation of new stars, these hot and bright stars generate optical-UV emission and give the spiral galaxies their typical blue color. Elliptical galaxies are usually less gaseous, and their stellar population is old which translate into their usual red color. This tell us that the gas content which can lead to different star formation rates, play an important role in the physical properties of the galaxy.

1.1.1 Bimodality distribution

Most of the galaxies in the local universe fall into one of these two categories: blue and young or red and old (e.g. Strateva et al. 2001; Balogh et al. 2004), this bimodality (Fig. 1.2) was discovered from the analysis of the distribution of colour versus absolute magnitude of a sample of $z \leq 0.1$ from the Sloan Digital Survey (SDSS) (Baldry et al. 2004).

The blue cloud consists of star-forming, low-mass galaxies, which are disk dominated. The red sequence consists of massive spheroidal galaxies with low to zero star formation. A transitional region known as the green valley contains a population between the blue and red sequences. The lack of galaxies populating this region suggests there is a fast evolutionary track that goes from blue to red sequence (Martin et al. 2007), where a typical galaxy evolves along the blue cloud, increasing in mass through the accretion of gas from the cosmic web and through mergers with other galaxies. When this galaxy reaches a critical mass the star formation is quenched and the gas supply is shut off, and the galaxy moves quickly into the red sequence and evolves passively.

1.1.2 Super massive black holes

A black hole that is a final product of stellar evolution can have a mass in the order of ~ 10 M$_\odot$ while super massive black holes (SMBH) can have masses in the range $10^6 - 10^9$ M$_\odot$, which can translate into event-horizon radii of $10^{-7} - 10^{-5}$ pc. direct evidence of this comes from the proper motions of the stars around our Galactic centre (Sgr A*) (Schödel et al. 2002; Ghez et al. 2008; Genzel et al. 2010). The mass of SMBHs has been estimated using stellar or gaseous kinematics (Kormendy & Gebhardt 2001; Ferrarese & Ford 2005a, e.g.). SMBHs are thought to be ubiquitous in the centre of most, if not all, galaxies in the local universe. Furthermore, there are indications that the SMBH might have an important role to play in the host galaxy evolution.

1.2 Active Galactic Nucleus

An active galactic nucleus (AGN) is a very bright compact region at the centre of a galaxy. These objects can reach about 10^4 times the luminosity of its galaxy, and its luminosity cannot be attributed to star emission. This radiation is produced in a very small volume (< 1 pc^3) covering a wide range of frequencies. The first

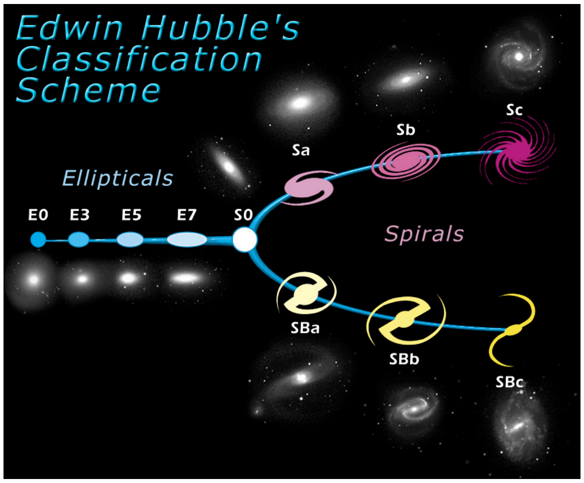

Figure 1.1: Hubble galaxy classification diagram. Source: Hubble telescope website.^{1}

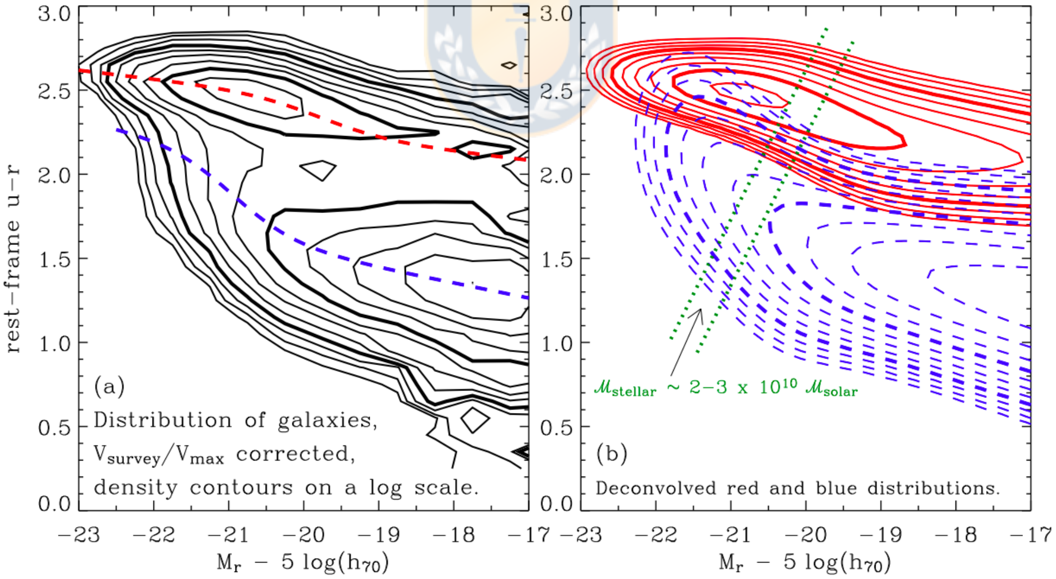

Figure 1.2: bimodal distribution of the sample of galaxies from the SDSS in rest-frame color vs. absolute magnitude. The contours are determined for galaxy number counts in 0.1 color × 0.5 mag bins. The upper and lower dashed lines represent a fit to the mean positions of the Gaussian color functions for the red and blue distributions, respectively. Source: Baldry et al. (2004)

observation of what we now know as an AGN was obtained by Fath (1909) and the object (NGC 1068 which at that point was not yet known to be extragalactic) exhibited strong emission lines. It was Carl Seyfert who, 25 years later, published the spectral analysis of six objects with similar characteristics (strong and broad high-excitation emission lines) and attributed the width of the lines to Doppler shifts, these objects came to be known as Seyfert galaxies, and were later classified into type I and type II, where the former type exhibit broader emission lines than the latter. The first attempts to understand the physics of these objects indicated a size of 1-100 pc and if the material producing the broad emission lines was gravitationally bound the central mass should be the order of 10^{10} $M_{\odot}$. Early radio surveys lead to the discovery of quasars, extremely bright radio sources that appear to be associated with optical point sources, i.e. star-like, it was later accepted that these were a brighter and more distant version of Seyfert galaxies. It became evident that the activity observed in the centre of some galaxies could cover a wide range of scale, luminosity and properties. This lead to different types of AGN classifications, according to a) Radio emission: radio loud, radio quiet. b) Optical spectrum: narrow-line (Seyfert type II), broad line (Seyfert type I). c) Special types: Blazars, optically violently variable objects.

1.2.1 Unified model

The discovery of polarized broad lines in the spectra of Seyfert 2 galaxies (Miller & Antonucci 1983) led to the unified model which is based on the idea that the phenomenological differences observed in the different kind of AGN could be explained by a small number of physical parameters. The first version of this unification scheme attempts to combine all the observed categories of AGN into a general picture that depends on two components: the inclination of the AGN with respect to the line-of-sight (LOS) and the source luminosity (Fig. 1.3). This scheme is based on a morphology where the SMBH is surrounded by an accretion disk, which itself is surrounded by a 'donut-shaped' dusty torus, which if observed edge-on will obscure the broad emission lines generated closer to the nucleus giving rise to a type II Seyfert, while if seen face-on the nucleus would be exposed, producing a type I Seyfert.

1.2.2 On the origin of nuclear activity

As we have seen from the range of properties presented by AGNs all of them have in common an extreme energy output that comes from a very small volume. The fundamental question is: how is this energy produced. This question was highly debated after the discovery of quasi-stellar objects (QSOs) currently the prevailing idea is that energy is produced via accretion onto the SMBH (e.g. Hoyle & Fowler 1963; Salpeter 1964; Lynden-Bell 1969; Rees 1984). Many arguments support the claim that AGNs are fuelled by gravitational accretion onto the SMBH, among which we find: a) the instability of another object that is both so massive as well as compact, b) the observed bolometric luminosities can only be explained with radiative efficiencies as the ones obtained from accretion, c) assuming an isotropic distribution of radially accreting material only subject to gravitation and radiation pressure, considering an isotropically radiating point source, the equilibrium between radiation pressure and gravitational force will define the upper limit of the Eddington luminosity, which gives a lower limit for the mass of the source:

$$M_\bullet > 10^6 M_\odot \frac{L_{bol}}{10^{44} ergs^{-1}}$$

.

1.2.3 AGN components

The AGN phenomenon is a complicated one, that can be broadly studied by the following scheme:

Accretion

It is now widely accepted that AGNs are fuelled by accretion onto the SMBH. We assume that this fuelling occurs in a smooth time-steady manner, because if the fuelling was discrete, for example if the BH accreted stars, it would be difficult to obtain the energies observed, as the efficiency of accretion as an energy release mechanism is strongly dependent on the compactness of the accreting object.

Spherical accretion

The simplest way in which this accretion can occur is via a spherical geometry (known as Bondi or spherical accretion). In this scenario we assume the gas starts in a large sphere, where at large radius the gas is moving very slowly compared to the BH. The gas radial motion will depend on the force of gravity combined with the radiation pressure. The density of the gas required for the accretion process is very modest ($\sim 10^{-24}$ gm cm^{-3}). Spherical or quasi-spherical accretion can occur when the infalling material has a small angular momentum, this geometry can provoke a steady flow of matter to the centre without the formation of shocks. However, Bondi accretion does not consider the accretion of a turbulent, non-uniform gas, it also assumes the gas momentum is negligible, and the BH cannot be considered as an isolated object, as they reside at the bottom of the galactic potential well.

Eddington limit

For further discussion of the accretion flow we must now consider the fact that the central object is generating a large amount of radiation which will produce a radiation pressure. An spherical accretion process of fully ionized gas can proceed as long as the gravitational force (f_g) is larger than this radiation pressure (f_{rad}). This condition will have a limit when $f_g = f_{rad}$ which leads to the so-called 'Eddington luminosity' or 'Eddington limit', this luminosity is described by the relation:

$$L_E = \frac{4\pi c G M \mu m_p}{\sigma_T} = 1.51 \times 10^{38} (M/M_\odot) ergs^{-1}$$

This means that for any given mass, there is a critical luminosity (L_E) beyond which the radiation pressure will overpower the gravitational force.

Accretion disk

The most accepted model is that accretion usually takes place via a disk due to its efficiency. The infalling material will have some non-zero angular momentum, at the last stable orbit of a 10^8 M$_\odot$ BH the gas will have a momentum of $\sim 10^{24} cm^2 s^{-1}$, for the material to be able to fall into the BH it needs to loose this angular momentum. Each gas particle would have its own angular momentum and its own velocity vector. The sum of the angular momentum vectors of all the particles must be conserved, even in the presence of collisions. This total vector would point to a specific direction which will be perpendicular to the position and velocity vectors. Collisions in the plane of intersection between the particles will drive the angular momenta of the individual particles closer to the average vector and this will bring their orbits into the same plane, perpendicular to the total angular momentum. An accretion disk is thus naturally formed. To transport the material in the disk towards the centre the gas must loose angular momentum which can occur via a redistribution of the angular momentum, this is, gas at smaller radii loses angular momentum that is gained by gas further away from the centre, this can occur via internal torques, due to, for example, the viscosity of the disk. Or, the entire system can loose angular momentum, for example via hydromagnetic winds.

One strong piece of evidence for the presence of accretion disk surrounding the BH are the observations of double peak emission line profiles. Occasionally the orbiting gas in the accretion disk would produce a radio maser from transitions of the water molecule, this can be spatially resolved using interferometry for very nearby galaxies. The line-of-sight (LOS) velocities can be measured from the Doppler shifts of emission lines and the velocity profile of the disk rotation can be obtained.

Broad line region

The broad line region (BLR) is the area from where the broad component of the emission lines are emitted. The gas in this region is photoionised by the continuum radiation of the AGN. The electron density of this region is $\sim 10^{10}$ cm^{-3} and the gas clouds are situated very close to the SMBH, within light-days to light-months, which means this region has not yet been spatially resolved, even in the nearest AGNs. The temperature of the BLR is estimated to be T $\sim 10^4$ K, this temperature correspond to thermal line widths of order 10 km/s, which implies that the gas in the BLR moves supersonically, the typical velocities observed are in the range $\sim 10^3 - 10^4$ km/s. The emission observed in the BLR originates in permitted transitions, the most relevant ones being Balmer and Lyman Hydrogen series. The kinematics of the BLR is directly connected to the mass of the SMBH as they lay inside the gravitational sphere of influence of the SMBH.

Narrow line region

The narrow line region (NLR) is the area where the narrow component of the emission lines is emitted. The gas of this region does not fall inside the dominating influence of the central black hole. This region extends over a larger scale than the BLR, the size of the region will depend on the luminosity of the AGN, clouds can be observed where $L/4\pi r^2 \simeq 10$ ergs/s/cm^2 ~ 3 kpc for a very luminous AGN, while the NLR can usually extends over 100-300 pc on nearby Seyferts. The gas clouds are ionised and heated by the central source, the density in this region is relatively low ($\sim 10^4$ cm^{-3}) which allows magnetic dipole transitions to occur, these forbidden lines are characteristic in the NLR spectrum. The emission lines generated in this region are only narrow in comparison with the broad lines of the BLR, as they typically range 300-600 km/s but higher velocities (¡ 1000 km/s) have been observed. The temperature is similar to the BLR ($\sim 10^4$ K) and it has been theorised to have a clumpy structure.

Torus

The unification scheme suggests that the central engine is surrounded by a dusty toroidal structure composed of optically thick gas situated 1-100 pc from the SMBH. This region has a density of $10^4 - 10^6$ cm^{-3} and a extremely large column density of 10^{25} cm^{-2}, this optically thick gas can only be penetrated by hard X-rays. This sort of structure would produce an anisotropic obscuration of the central region, exposing it only when observed face-on, and blocking the direct emission from the BLR in type-2 AGNs when observed edge-on. This toroidal structure can collimate the AGN radiation, producing the biconical shapes observed in the NLR, known as ionisation cones. This structure covers a large range in radii and thus can cover a large range of physical conditions, which must be similar to molecular clouds and thus are likely to contain a large amount of dust. The dust re-emission in the IR is a characteristic property of the torus. The thermal radiation from the torus dominates the NIR and MIR emission of the AGN, this is called the 'red bump', and it cuts off at $\sim 1\mu$m where the UV/optical emission from the accretion disk dominates. The dynamic origin and characteristics of the so-called torus are still under debate as the support of obscuring material against gravity presents a dynamical problem. For example, a donut-shaped obscuring structure that was hydrostatically supported and covered a large solid angle would contain gas that had velocities of a least a few tens of km/s, corresponding to a temperature of $\sim 10^5$ K, such a high temperature will lead to the destruction of any dust grains present. A solution to this problem is a clumpy torus model where the dust is arranged in clouds (e.g. Krolik & Begelman 1988), this can account for several of the observed properties of AGN. Other models suggest that the gas is supported by radiation pressure, or that the obscuring material is not static and instead is on a continuous stream in or out the central engine, for example the radiation-driven fountain model suggested by Wada (2012).

1.3 Fuelling the AGN

1.3.1 The fuelling problem

To understand why fuelling the AGN is a very complex problem let us consider an AGN of $\sim 10^{10-11} L_{\odot}$. To power this luminosity for the typical AGN duty cycle of 10^8 yrs, assuming the usual 10% energy conversion rate, we obtain a rate of $.1 M_{\odot} yr^{-1}$.

To sustain the activity of this AGN for that amount of time the necessary amount of gas is $10^7 M_\odot$. This is an important fraction of the total gas in a typical galaxy, and thus the fuelling gas could come from the host galaxy disk, particularly from the ISM, as 10^8 yrs is comparable to the rotational time scale of a galaxy. Since this material is found at the large (kiloparsec) scale of the host galaxy it will contain a large amount of angular momentum. At a given point in the galaxy the momentum per unit of mass of the orbiting material is $\sim 10^{29}$ cm^{2}s^{-1} which is $\sim 10^5$ larger than the specific angular momentum of material in a marginally stable orbit around a black hole of 10^8 M$_\odot$. Even at a radius of 200 pc from the centre the angular momentum is a factor 1000 too large, thus for the gas to be able to fall into the central engine it must loose 99.99% of its angular momentum. To fuel the AGN we need to find mechanisms that are able to remove the angular momentum of the large scale gas so this material can fall to the centre and feed the SMBH.

1.3.2 The fuelling flowchart

A flowchart that describes the possible mechanisms that can achieve angular momentum removal to fuel material to the SMBH was proposed by Shlosman et al. (1990), (Fig. 1.4). This flowchart suggests mechanisms from 10 kpc down to the central engine. Gravitational torques, dynamical friction, viscous and hydrodynamical torques are some of the mechanisms proposed not only by Shlosman et al. (1990) but in the studies made since. Since different mechanisms can be dominant at different scales, and not one of them can bring the gas from large scale to the actual BH on its own, it is possible that there is a hierarchy of torque mechanisms that work in a succession of steps to bring the gas to the central engine. The source of the fuelling also depends on the luminosity of the AGN studied, as the accretion rate required will be widely different for a low luminosity AGN than for high luminosity AGN or quasar, which require larger accretion rates.

1.3.3 Large scale: 10 kpc

The gravitational field of a galaxy can be described with an axisymmetric potential, the angular momentum is conserved in this potential, and thus the material would keep orbiting the central mass. However, if a perturbation or a gravitational instability to this axisymmetric potential was introduced a gravitational torque would be exerted which would cause the removal of angular momentum thus allowing the inflow of material.

Gravitational torques work on a timescale comparable to the orbital timescale and provide the most efficient way to reduce angular momentum on large to intermediate scales (i.e. few kpc scale to the inner kpc).

Galaxy interactions and mergers are one of the most efficient mechanisms to produce strong torques, and thus removal of angular momentum. Interactions can trigger stellar bars, and mergers, especially major mergers, can provoke a striking change in geometry, which breaks the symmetry of the gravitational potential allowing torques to be exerted by the new asymmetric potential, and thus generating large inflows of gas into the inner kpc, and could also trigger intense starburst events in the galaxy. Statistically significant correlations between AGN activity and signs of strong interactions are found only for large accretion rate galaxies ($10M_{\odot}yr^{-1}$), such as very luminous or radio-loud QSOs and FR-II radio galaxies (e.g. Disney et al. 1995; Kirhakos et al. 1999; Yates et al. 1989).

Secular evolution: Bars and spiral arms

Bars can be found in 70% of local spiral galaxies (e.g. Eskridge et al. 2000) and they might even be a common feature up to $z \sim 1$ (Sheth et al. 2003). Bars act as a perturbation to the galaxy axisymmetric gravitational potential, and thus they can exert torques and drive dynamical evolution and remove angular momentum from gas, allowing it to flow to the central 100 pc. The advantage of bars over spiral waves and other non-axisymmetric features is that they are long-lived and usually represent a stronger perturbation.
If we consider an axisymmetric potential $\Phi_0(r)$ in the plane $z = 0$. An orbit in this potential would be circular and have an angular velocity of

$$\Omega^2 = \frac{1}{r}\frac{d\Phi}{dr}$$

To add the bar to this approximation we consider the bar as a bisymmetric gravitational potential (Φ_1) which acts as a weak perturbation to the axisymmetric potential of the galaxy, the total potential will be described by

$$\Phi(r) = \Phi_0(r) + \Phi_1(r)$$

The bar perturbation has a predominant Fourier component $m = 2$, which rotates in the galaxy with a patter speed Ω_b.

Let us consider the linearisation of this potential close to the circular orbit we can approximate, in first order, the motion of a particle in the orbit with an epicyclic oscillation, this oscillation will have a frequency κ, and is given by:

$$\kappa^2 = \frac{d^2\Phi}{dr^2} + 3\Omega^2 = r\frac{d\Omega^2}{dr} + 4\Omega^2$$

The orbit thus can be described as the combination of a circle and an epicycle. There will be a region in which the patter speed is equal to the frequency of rotation $\Omega_b = \Omega$, this is known as the corotation resonance (CR). Apart from this resonance the rotating bisymmetric bar can create two other fundamental resonances known as inner (ILR) and outer (OLR) Lindblad resonances (Lindblad 1964), which can occur when $\Omega_b = \Omega \pm \frac{\kappa}{m}$. The importance of these resonances is that they define regions where periodic orbits change orientation. The families of periodic orbits can be separated in 2 groups (Fig. 1.5):

- x_1: is the main family supporting the bar. Orbits are elongated parallel to the bar and extends between the centre and CR.
- x_2: resides between the two ILRs, the inner ILR (IILR) and outer ILR (OILR), in case they exist, or between the centre and the ILR if only one exists. They are more round and oriented perpendicular to the bar.

The orientation of the periodic orbits will rotate by 90° at each resonance crossing, this will generate some areas where the orbits cross, which is not a problem for the stars as they are collisionless, however, the situation is different for the gas as it is collissional and dissipative. The gas will attempt to follow the orbits but gas clouds can collide where orbit cross, causing gas orbits to change more gradually from one direction to the other. This will lead to spiral-shaped streamlines that have an offset with respect to the stars (Fig. 1.5). A negative torque is exerted between the CR and the outer ILR and this removes angular momentum from the gas and let it flow towards the inner 1kpc - 100 pc.

A correlation between bar incidence and starburst has been observed by Hunt & Malkan (1999) from the analysis of the extended 12 μm Galaxy sample (E12GS). Large-scale bars are present on $82-85\%$ of the starburst nuclei while they are present on $61-68\%$ of quiescent galaxies that do not present signatures of HII, starburst, LINER or Seyfert I, II. Given that powerful starburst can exist in the inner 1 kpc - 100 pc radius where large amount of gas can accumulate. This correlation can be the result of large-scale bars fuelling gas to the central region of galaxies.

Comparisons between bar fraction in active galaxies versus inactive galaxies have shown no correlation between bar and activity (e.g. Ho et al. 1997b; Martini & Pogge 1999a). Knapen et al. (2000) found a larger fraction of barred active galaxies (79%) than in inactive galaxies (59%) using NIR data with a significance of 2.5σ. Cisternas et al. (2013) studied the accretion rated between barred and non-barred active galaxies and found similar values for both groups.
One explanation for this lack of correlation is that while the bar is efficient in bringing gas to the central region, this gas can get stalled at the ILR and thus it would further depend on other mechanisms to bring this gas into the SMBH itself. The necessity of more than one mechanism to feed the AGN could dilute the correlation between bar and activity.
Nuclear spirals could trace the feeding channels of the gas journey to the SMBH beyond the 100 pc limit (Martini & Pogge 1999a). A larger presence of dusty spirals and structures in the nuclear region in active galaxies than in inactive galaxies (Simões Lopes et al. 2007).

1.3.4 The inner region: 1 kpc to 100 pc

We have established that bars are an efficient mechanism to fuel gas to the inner region, the question that follows is: what happens when the gas is able to reach the inner 1 kpc - 100 pc region. An important parameter that defines the fate of the gas in the inner region is not only the presence of Lindblad resonances but the types of Lindblad resonances present in the galaxy, these would depend on the patter speed of the bar (Ω_b). If the galaxy contains an ILR a ring is expected to form at the ILR radius, this is because at this radius the radial flow starts to slow down as it crosses the ILR because the shocks associated with the large-scale bar are becoming more weak, the gravitational potential is becoming more symmetric and the gravitational torques in the vicinity of the ILR are weaker or even reverse. Gas rings near the ILR radius have been observed (e.g. Kenney et al. 1992; Jogee et al. 2001) and numerical simulations show that rings form in a few dynamical times (e.g. Combes & Gerin 1985a; Schwarz 1981)

If the galaxy contains a central region that is rotating rigidly we expect to find two Lindblad resonances around the core radius. A gas ring can form between IILR and OILR. If this ring has enough mass it can develop instabilities and that would cause the ring to fragment and create a ring starburst. If the gas mass is larger than $\sim 10\%$ of the dynamical mass, the fragmented ring can collapse and this gas can flow to the central 100 pc.
If the gas inside the IILR is massive this can fall towards the central engine before

the ILR ring is formed and thus rapidly fuelling the AGN. Another type of fuelling can occur if the central region contains a large mass concentration which can give raise to a nuclear ILR (nILR), offset shocks can be form around the nILR which connect to a ring usually smaller than the nILR, gas can flow due to shocks in the ridges and settle in this smaller ring.

When the galaxy does not have an ILR the mass of the gas disk or its self-gravity takes on a more important role. If the disk is massive it can provoke a bar-mode instability of the gas core accumulated by the large-scale stellar bar. If the disk is stable against a bar-mode instability the gas disk can still be unstable on local scales and it can fragment into many clumps, these clumps would suffer from dynamical friction with the stellar component causing them to eventually fall to the centre.

Another mechanism was proposed by Shlosman et al. (1989) the so-called bars-within-bars mechanism. This double-barred system may theoretically be more efficient than a single bar in transporting gas to the centre. A number of nearby barred galaxies show signatures of an inner bar within the inner few hundred parsecs, these inner bars appear to be randomly oriented with respect to the large scale bar. A secondary bar can formed through decoupling. It is possible that the bars share one resonance, and that they exchange energy with each other. The nuclear bar can exert new torques and thus bring the fuelling material closer to the centre.

1.3.5 Parsec and sub-parsec scale

Once the gas reaches the $\sim$ 100 pc scale our understanding of the necessary mechanisms to further drive gas to the nucleus is much more limited. At a radius of 100 pc the material still needs to loose angular momentum to reach the nucleus. Some of the mechanisms able to achieve this are: dynamical friction and feedback from star formation occurring in the inner 100 pc, tidal disruption of gas clumps, runaway self-gravitational instabilities which can lead to the formation of nested bars, stellar mass loss and disruption of stellar clusters.
When the gas is able to reach subpc scales other type of mechanisms should come into play such as viscous torques, warping induced in an accretion disk due to radiation pressure from the nuclear source, and hydromagnetic winds.

1.4 AGN feedback

The large amounts of energy released in the AGN can have an impact on its host galaxy. AGN feedback is the process that links this energy with the surrounding gaseous medium and its further impact on the galaxy.

The cold dark matter mechanism (CDM) is proven to be successful in the reproduction of a large number of observations, especially at large scale. This paradigm predicts the formation of dark haloes in a 'bottom-up' fashion, that is, via a hierarchical evolution. The star formation histories of galaxies, however, do not seem to follow this same 'bottom-up' evolution.

Hierarchical galaxy formation predicted that small galaxies would form first, and larger galaxies after. However, it has been discovered that mainly giant elliptical galaxies are redder (de Vaucouleurs 1961) and haver higher metallicities than expected (Faber 1973) which indicates the presence of old stellar populations, they also have high $[\alpha/Fe]$ ratios (e.g. Faber et al. 1992; Ziegler et al. 2005), which can be an indication of a shorter star formation time-scales. This is called 'downsizing' as the galaxies have their stellar population in place early (by $z \sim 2$), while the low mass galaxies evolved more slowly (e.g. van Dokkum et al. 2004; Treu et al. 2005).

One of the explanations for downsizing includes feedback from both star formation and AGN which would help suppress star formation, either by removing or heating the gas in the ISM.

Two main modes in which feedback can occur have been identified: radiative and radio mode, the name of which depend on the source of the energy, the energy injected in the environment near the AGN can regulate the feeding of the SMBH itself thus regulating the AGN duty-cycle.

1.4.1 Radiative mode

The radiative mode, also called quasar or wind mode, occurs when the accretion rate and thus AGN luminosity is high, close to Eddington luminosity. This type of luminosity is found only in high-redshift ($2 \sim 3$) QSOs. The radiative pressure can heat or expel the gas from the AGN creating an outflow that pushes gas out of the bulge of the galaxy thus quenching star formation. The heat and momentum the wind carries can also prevent the galaxy from cooling rapidly (Silk & Rees 1998). Because of the large accretion rate this mechanism requires it is thought to be an initial mechanism by which star formation is halted, since it would occur at the early stages of the quasar evolution. This process could move galaxies from the blue-cloud, where the galaxy is actively forming stars, to the red sequence, where passive evolution takes place (e.g. Granato et al. 2001).

1.4.2 Radio mode

The second mode, known as radio or kinetic mode depends on the presence of radio jets. This mode takes place at lower luminosity AGNs ($L < 0.01L_E$). The radio jets or lobes can deposit energy in the ambient medium and heat the gas. The radio mode is more effective in preventing cooling flows temporarily in massive galaxies at lower redshifts. This mode is considerate to be a 'maintenance mode' as is not destructive and can keep a balance between cooling a heating. X-ray and radio observations show the presence of bubbles that can carve large cavities in the hot gas (e.g. McNamara et al. 2008; McNamara & Nulsen 2012), the presence of shock fronts is also observed. The size of the cavities in clusters can typically be ~ 20 kpc but can reach as much as 200 kpc. These cavities often coincide neatly with a radio source, which suggests that the radio lobes caused the bubble inflation that displaced the hot gas and created the cavities.
FR I-type sources are on average strongly dominated by mechanical energy, and this modest sources can be mechanically powerful enough (Cavagnolo et al. 2010). Feedback from modest radio sources can play a very important role on the environments of their host galaxy, by driving outflows, quenching star formation and cooling flows.

1.4.3 Observations

Gas outflows are one of the main signatures of feedback and they have been observed in different wavelengths. AGN driven outflows are thought to be launched from the accretion disk or the dusty torus, in the form of a radiatively-driven wind when in quasar mode, or a radio jet if in radio mode. The radio jets can sweep gas in the ISM creating kpc-scale outflows (e.g. Springel et al. 2005; Hopkins et al. 2006).

Strong outflows are found at low redshift (e.g. Morganti et al. 2005a, 2007). IFU observations of nearby Seyferts show outflowing gas in the inner 100 pc (e.g. Storchi-Bergmann et al. 2007a; Bergmann 2012; Schnorr-Müller et al. 2014; Riffel et al. 2014). High-velocity outflows that originate close to the accretion disk have been observed in a low-redshift quasar (Young et al. 2007). Some of the high-velocities outflow observed have kinetic energies that are an important fraction of the AGN bolometric luminosity (e.g. Morganti et al. 2005b; Pounds et al. 2003).

Molecular outflows are now frequently observed in the local universe (e.g. Alatalo et al. 2011; García-Burillo et al. 2014; Cicone et al. 2014; Davies et al. 2014). Tracing outflows at radio wavelengths can help us understand how this outflows affect the kinematics of the galaxy. Outflows with sizes of a few kpc have been observed, which is significant enough to impact the host galaxy and cause star formation quenching. Outflows more powerful than those observed at low redshifted are observed at higher redshift (Maiolino et al. 2012). Unexpectedly fast outflows have been observed in molecular gas (Feruglio et al. 2010).

1.5 The connections between AGNs and their host galaxy

The SMBH mass (M.) correlates with properties of the host galaxy bulges, in the local universe, these include luminosity, mass, and velocity dispersion (Gebhardt et al. 2000; Ferrarese & Ford 2005a; Ferrarese & Merritt 2000; Marconi & Hunt 2003; Kormendy & Ho 2013a, e.g.), the latter is a very tight correlation, with rms ~ 0.3. In contrast, the SMBH mass does not correlate with disk properties. (Madau & Dickinson 2014) The global galaxy star formation history (and thus the galaxy stellar mass growth) peaks at redshift $z \sim 2-3$ and then declines rapidly, the same tendency is observed for cosmic BH accretion history (e.g. Zheng et al. 2009). The ubiquity of SMBHs at the centre of galaxies in the local universe might be an indication that every galaxy went through a short-lived quasar phase leaving the SMBH as a relic (Yu & Tremaine 2002, e.g.).
These studies indicate a strong connection and possible co-evolution between the black hole and its host galaxy.

As we saw in the previous section a fraction of the energy released by the accretion process into the SMBH might have a strong influence in the host galaxy, this feedback process can regulate the growth of the BH itself but also quench star formation and prevent the growth of too many massive galaxies.

Sanders et al. (1988) followed by Hopkins et al. (2006) proposed an evolutionary sequence which started in the early universe ($z \sim 4-6$) with gas rich disk galaxies with a BH in their centre, while the BH remains below the critical mass the BH keeps accreting and the galaxy forms stars, as no feedback mechanisms is yet activated.

The galaxy continues to grow via galaxy interactions like minor mergers or accretion of gas from the inter-galactic medium, then if a major-merger takes place it can produce important tidal torques that would bring large amounts of gas to the central region triggering starburst and an important SMBH growth. This evolutionary pathway is relevant because the most luminous AGNs are mostly observed in major mergers. Moderate-luminosity AGNs will follow a different evolutionary sequence, such as secular evolution, which can be driven by internal mechanisms such as non-axisymmetric gravitational potentials.

The full effect of AGN feedback in galaxies and how the BH alters the evolutionary pathway of the galaxy is yet to be completely understood.

1.6 Thesis objectives

As described in this introduction the processes of feeding and feedback and their signatures often occur simultaneously and are thus difficult to disentangle in the central region of galaxies. To study and understand these processes we need to build up detailed studies of galaxies, this can only be achieved in nearby galaxies because of the sensitivity and resolution required to analyse the kinematics in detail.

The advent of ALMA and integral field units (IFUs) have opened new opportunities to carry these studies at great detail, as it is possible to obtain sub-arcsecond resolution observations which allow us to map inflows and outflows and disentangle the often complex kinematics observed in the central region of nearby galaxies. Existent surveys, (e.g. CALIFA and SDSS IFU), do not yet have the required sub-arcsecond resolution to fully explore the details of the feeding cycle occurring in active galaxies. Therefore, intensive studies of individual galaxies, even in smaller samples, play an important role in expanding our understanding of the feeding and feedback processes, and allowing a better synergistic interpretation of the lower resolution larger sample studies.

The aim of this thesis is to carry intensive and detailed studies of the kinematics in a small sample of nearby active galaxies, and search for signatures of feeding and feedback using IFUs and ALMA data.

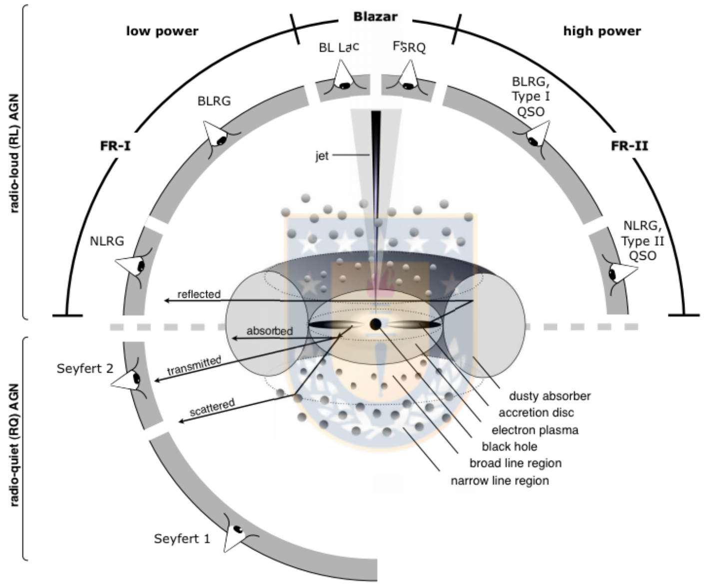

Figure 1.3: Schematic representation of the unified model of the AGN phenomenon. Source: Marie-Luise Menzel (MPE) (Beckmann & Shrader 2012).

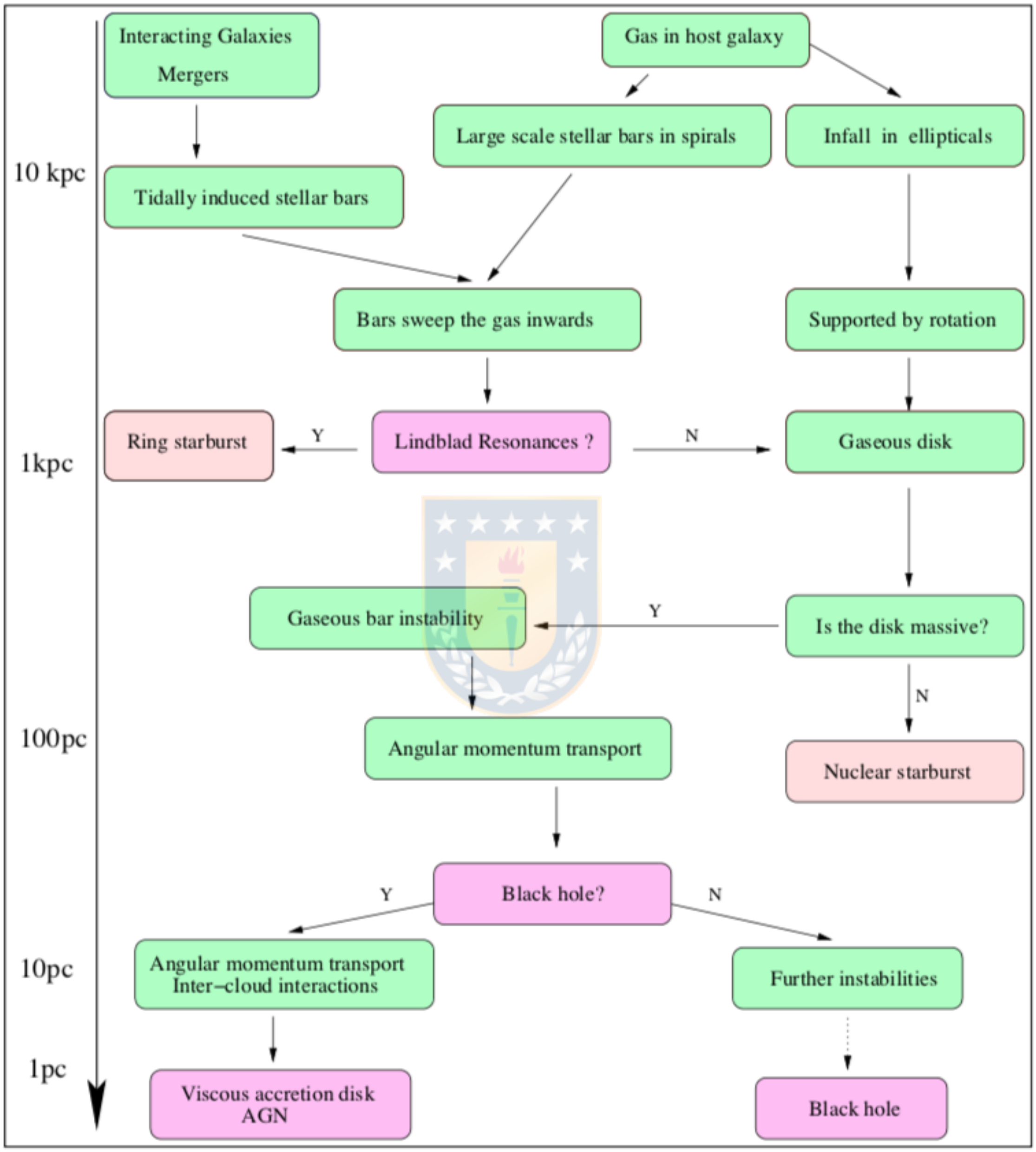

Figure 1.4: Flow chart that represents various process possibly involved in AGN fuelling at different scales from the centre. Source: Shlosman et al. (1990).

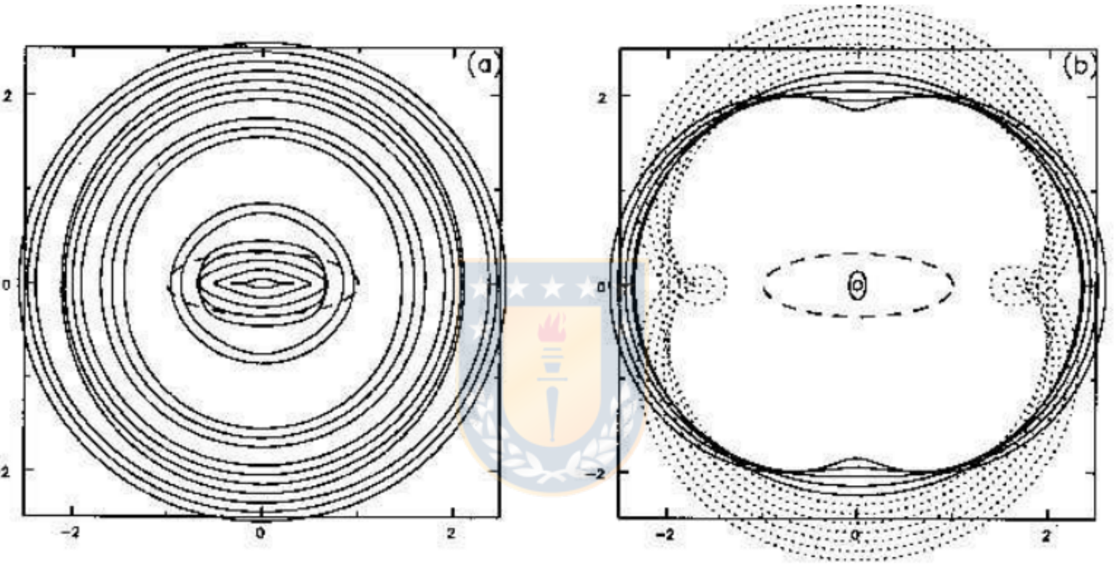

Figure 1.5: Some periodic orbits in a bar model. Full (dotted) lines are stable (unstable) orbits. The boundary of the elliptical bar is marked as a dashed curve. Left: Orbits from the main x_1 family. Right: small orbits near the bar correspond to the x_2 family. Source: Sellwood & Wilkinson (1993)

Chapter 2

The complex jet- and bar-perturbed kinematics in NGC 3393 as revealed with ALMA and GEMINI-GMOS/IFU

This thesis chapter originally appeared in the literature as
Finlez, C., Nagar, N., Storchi-Bergmann, T., Schnorr-Müller A., Riffel, R., Lena D., Mundell C.G., Martin S., *MNRAS 479,3,p.3892-3908*

2.1 Introduction

It is widely accepted that most – if not all – nearby galaxies with a bulge component host a super massive black hole (SMBH) in their center (e.g. Ferrarese & Merritt 2000; Kormendy & Richstone 1995; Ferrarese & Ford 2005b). A considerable amount of observational evidence supports a connection between SMBH and the host galaxy growth, the main one being a strong correlation between the mass of the SMBH and the properties of the bulge of the host galaxy (Gebhardt et al. 2000); nevertheless, the details of coevolution of the SMBH and the host galaxy remain the subject of an ongoing debate.

Despite the ubiquity of SMBHs at the center of galaxies, only a small fraction of these are active galactic nuclei (AGN) in the local universe (e.g. Kewley et al. 2006; Ho et al. 1997a). The questions of what triggers activity in a galactic center and if this ignition mechanism is related to the host galaxy properties, arise naturally.

The lack of activity in the nucleus can be related to a lack of accretion material or the absence of a fueling mechanism. The amount of gas needed to fuel an AGN over a normal duty cycle is a large fraction of the total gas contained in the galaxy (Combes 2001), thus a fueling mechanism must be able to remove most of the angular momentum of a large amount of gas so this can be transferred from the kpc-scale into the sub-pc central region to feed the AGN.

Gravitational mechanisms such as galaxy interactions can drive gas inwards. Major mergers are thought to be responsible for the high accretion rate observed in luminous quasars, while minor mergers can produce Seyfert-level luminosities. Alternatively, secular mechanisms can also remove angular momentum and drive gas towards the nucleus. Observations point to secular processes being the most common triggering mechanisms for medium to low luminosity AGNs. (e.g. Hopkins et al. 2014; Treister et al. 2012; Fan et al. 2016; Goulding et al. 2017a)

Non-axisymmetric potentials, such as spiral structures and bars can produce radial inflows to the central region, which can be observed as line-of-sight velocity distortions (Lin & Shu 1964; Lindblad 1964). Gas transport via bars is efficient (e.g. Mundell & Shone 1999) from large scale down to the inner kpc, where gas can get stalled in rings at the inner Lindblad resonance region (Combes & Gerin 1985b). From this scale to the center other mechanisms can be invoked to transport gas to the AGN, such as inner spiral structures and bars within bars (Shlosman et al. 1989).

The incidence of bars is similar in both active and non-active galaxies and thus a strong correlation between bar presence and activity is yet to be found (e.g. Knapen et al. 2000; Cisternas et al. 2013; Galloway et al. 2015; Cheung et al. 2015; Goulding et al. 2017b) . However a difference between active and inactive galaxies has been observed by Simões Lopes et al. (2007) and Martini & Pogge (1999b). Using a sample of active and control galaxy pairs, they observed nuclear dust spirals and structures in 100% of the active early-type galaxies, but in only 25% of the control sample. This dust excess has been confirmed by Martini et al. (2013), and is thought to trace the feeding channels to the AGN (Ferrarese & Ford 2005b; Kormendy & Ho 2013b; Storchi-Bergmann et al. 2007b). Similarly, in a study of ionized gas dynamics in a matched sample of active and inactive galaxies, Dumas et al. (2007), identified increased kinematics disturbance as a function of accretion rate in the inner 1 kpc of AGN, where activity and dynamical timescales become comparable.

The non-axisymmetric gravitational potential created by a bar can produce important kinematic effects on the gas which have been studied by hydrodynamical (e.g Lindblad et al. 1996; Kim et al. 2012; Athanassoula 1992) and/or N-body simulations (e.g. Sellwood 1981; Emsellem et al. 2001b). A different method to gain insigth on these kinematic effects is to quantify the line-of-sight deviations from pure rotation, which can be achieved from linear perturbation theory (Lin & Shu 1964). The non-axisymmetric distortions to the planar flow can be decomposed in their harmonic components. Franx et al. (1994) and Schoenmakers et al. (1997a) pioneered an approach to interpret these harmonic coefficients based on epicycle theory, and thus only valid for small departures from circular orbit speed. Since then, this harmonic decomposition analysis has been carried by several authors, e.g., Wong et al. (2004); Emsellem et al. (2001a).

One aspect of the SMBH-host galaxy connection is the interaction between the gas of the host galaxy and the energy generated by the AGN, which produces a feedback process that has been theorized as an important component in galaxy evolution as it can help to regulate the growth of the galaxy, preventing it from becoming too massive (Di Matteo et al. 2005; Wagner & Bicknell 2011; Fabian 2012). This interaction can occur, broadly, in two main modes: radiative or quasar mode and kinetic or radio mode (Croton et al. 2006; Fabian 2012). The former is driven by a wind caused by the accretion of material into the SMBH, producing wide-angle sub-relativistic outflows. The latter is driven by relativistic radio jets. Both these winds and jets can have important consequences in the galaxy evolution as they can heat and ionize cold gas when colliding with it, preventing the gas from collapsing under self-gravity, thus halting the accretion onto the SMBH and quenching star formation (e.g. Hardcastle et al. 2013; Best et al. 2005). The jets can also directly expel gas from the galaxy removing the components for further star formation (Nesvadba et al. 2006). However, some simulations (e.g. Antonuccio-Delogu & Silk 2010; Silk & Nusser 2010) reveal that jet activity is able to trigger star formation by producing high density cavities with low temperature, which are embedded in a cocoon around the jet (e.g. Best et al. 1998; Jarvis et al. 2001), a scenario known as positive radio mode feedback. The alignment of the outflowing gas with the jet suggests that the outflows are driven by the transfer of energy and momentum from the radio jet to the ISM, as shown by hydrodynamical simulations (Wagner et al. 2012). Jet-driven outflows have been observed in neutral and molecular gas (e.g. Morganti et al. 2005a; Dasyra & Combes 2012) and in the ionized gas (e.g. Holt et al. 2011; Riffel et al. 2006; Couto et al. 2017). Kinematic features consistent with gas inflows and outflows have been found in the ionized and molecular gas of the central region of nearby galaxies (e.g. Lena et al. 2016; Schnorr-Müller et al. 2016, 2017; García-Burillo et al. 2005, and references therein).

In this work we analyze the bar- and jet- induced perturbations on the molecular and ionized gas in NGC 3393 using new data from ALMA (CO J:2-1) and Gemini GMOS/IFU (optical spectra with information from stars and gas). NGC 3393 is a nearby, bright ($m_b = 13.1$ according to de Vaucouleurs et al. 1991), spiral (Sa) galaxy, at an estimated redshift of 0.012442 (optical), or 0.012509 (from the 21 cm line) which corresponds to a luminosity distance of 52 Mpc and a scale of 0.25 kpc/arcsec, assuming $H_o = 73$ km s^{-1} Mpc^{-1}. It is nearly face-on: Cooke et al. (2000) estimates an inclination of 13° by fitting a kinematical model (given by Bertola et al. 1991) to the [NII] emission line, and of 21° by fitting the narrow component of the [OIII] emission line in the central region. The galaxy covers over one arcmin on the sky, and it has been classified optically as a Seyfert 2 (Véron-Cetty & Véron 2003). It is interacting weakly with a nearby companion that is 60 kpc away (Schmitt et al. 2001).

From HI single dish observations the maximum rotation velocity corrected by inclination is 158 ± 7 km/s, and the central velocity dispersion is 197 ± 28km/s (Paturel et al. 2003). NIR images show a stellar bar in PA $\sim 159° - 165°$, with maximum ellipticity $e_{max} = 0.2$, and semi major axis (SMA) 13″. A faint nuclear bar has also been posited in position angle (PA) $\sim 145° - 150°$, $e_{max} = 0.46$, and SMA 2″ (Alonso-Herrero et al. 1998; Jungwiert et al. 1997). Läsker et al. (2016) modeled the light distribution of the galaxy using HST imaging and found two prominent rings: the first is actually a partial ring formed by two asymmetric tightly-wound spiral arms in an outer disk of radius 40″; the second is an inner ring that appears elongated, with a radius of 13″, i.e. coincident with the outer bar identified by Alonso-Herrero et al. (1998). These authors derive a PA of 140° for the 2″ SMA inner bar.

A high resolution HST [OIII] emission line image of the NLR (Schmitt et al. 2003) shows an S-shaped morphology with an opening angle of 90°, and an extension of 5.6″ pc (1410 pc along the ionization axis PA) × 3″ (740 pc), with the ionization axis oriented in PA 65°. Their derived PA is only slightly different from the value of 55° quoted by Schmitt & Kinney (1996) and Cooke et al. (2000). The sense of curvature of this S-shape is the same as the large-scale spiral arms. The [OIII] emission extends up to $r \sim 15''$ (3750 pc) along PA 44°. This S-shaped structure of high-excitation gas surrounds a three-component radio structure, as observed with the VLA at 1.5, 4 and 8.4 GHz (Cooke et al. 2000). The central radio source is unresolved and has a flatter spectrum than the lobes. Chandra data was also obtained by Bianchi et al. (2006) and Levenson et al. (2006), who found soft X-ray emission that has strong morphological correlations with the extended [OIII] emission.

The kinematics of the NLR has been studied by Cooke et al. (2000) using Fabry-Perot [NII] data. They found a skew between the velocity fields of the inner region and that of the outer arms, and fitted a rotation curve which indicates that the major axis of the galaxy goes from NE to SW along PA 68°, with the NE gas receding and the SW gas approaching. Assuming trailing arms, Cooke et al. (2000) conclude that the galaxy is rotating counter clockwise.

Using Chandra X-ray observations, Fabbiano et al. (2011) reported the presence of two X-ray sources which they suggested were obscured AGNs, separated by ~ 130 pc, with lower mass limits of $\sim 8 \times 10^5$ $M_\odot$ for the NE (primary) source and $\sim 10^6$ $M_\odot$ for the SW (secondary) source. More recent observations and analysis by Koss et al. (2015) found the same morphological correlations between the [OIII], X-ray and radio emission, but they conclude that the double SMBH detection is most likely spurious, resulting from the low number of X-ray counts (< 160) at $6 - 7$ keV and data smoothing with a few counts per pixel on scales much smaller than the PSF.

NGC 3393 is a Compton thick galaxy (Koss et al. 2015) and has polarized broad H_α and H_β emission lines (Kay et al. 2002; Ramos Almeida et al. 2016). A water maser emitting disk has been observed in the nuclear region using VLBI observations (Kondratko et al. 2008): this water maser disk is observed edge on, with a major axis in $PA \sim -34°$, i.e. perpendicular to the NLR axis. The kinematics of the water masers in the disk are consistent with Keplerian rotation, with an enclosed mass of $(3.1 \pm 0.2) \times 10^7 M_\odot$.

2.2 Observations and Data Reduction

2.2.1 Gemini GMOS/IFU

The observations were obtained with the Integral Field Unit of the Gemini Multi Object Spectograph (GMOS-IFU; Allington-Smith et al. (2002); Hook et al. (2004)) at the Gemini South Telescope on June 20, 2015 (project GS-2015A-Q-12). The observations were made in ”single-slit” mode, using the IFU-R mask, and the B600+G5323 grating with four exposures of 720 s each, adding small spatial ($0\farcs5$) and spectral ($50\mathring{A}$) offsets for every exposure. The spectral coverage of the observations was $\lambda4092 - \lambda7336\mathring{A}$, at a spectral resolution of $R = 1688$, covering the emission lines H_β, [OIII]$\lambda4959, 5007$, [OI]$\lambda6300$, H_α, [NII]$\lambda6548, 6583$, and [SII]$\lambda6717, 6731$, in addition to several stellar absorption lines. The field of view of

the observations was 3.″8 × 4.″9, which corresponds to a size of 0.96 kpc × 1.24kpc in the galaxy, sampled at 0.″08
Seeing during the observations was 0.″62 as measured from the FWHM of a spatial profile of the stars in the acquisition image, at the galaxy this corresponds to 155 pc.

The data reduction process was performed using the tasks from the GEMINI.GMOS packages for IRAF, following Lena (2014). This process includes bias subtraction, flat fielding, sky subtraction, wavelength calibration, flux calibration, differential atmospheric dispersion, and finally, the building of the data cubes with a sampling of 0.″2 × 0.″2. The four individual data cubes are combined to avoid the detector gaps, obtaining the final data cube used throughout this paper. The standard star used for flux calibration is LTT 7987, which was observed on May 30, 2015. Following the calibration pipeline results in a ~ 5 times overestimation of the flux, we correct for this factor in the final data cube.

2.2.2 ALMA: CO J:2-1

NGC 3393 was observed on May 3, 2016 as part of Project 2015.1.00086.S (P.I. Nagar). Four basebands (spw's) were used: each set to an effective bandwidth of 1.875 GHz. Spw1 was centered on the CO J:2-1 line (ν_{rest} = 230.538 GHz), with a channel width of 2.5 km/s. Spw2 was set to 'TDM' mode, for highest sensitivity, and used to cover the continuum centered on ν_{rest} = 232.538 GHz with 40.8 km/s channels. Spw3 was centered on the CS J:5-4 line (ν_{rest} = 244.935 GHz), with a channel width of 5.1 km/s. Spw4 was set to 'TDM' mode, for highest sensitivity, and used to cover the continuum centered on ν_{rest} = 246.936 GHz with 31.3 km/s channels. Forty one antennas were used and the total integration time on NGC 3393 was ∼26 min. Six minute scans on NGC 3393 were interleaved with one minute scans on the nearby 'phase-calibrator' J1037-2934. The latter is a well-studied compact quasar at redshift 0.312 with a position accurate to better than 1 mas. No flux calibrator was observed within this 'scheduling block'.

Data were calibrated and imaged using CASA version 4.7, and mostly followed the calibration script provided by the ALMA observatory (the CASA calibration pipeline was not available at the time of the release of this dataset). Since a flux calibrator was not observed for this project, flux calibration was performed by setting the flux of the phase calibrator J1037-2934 to 602 mJy at 235.7 GHz (a value provided in the ALMA observatories calibration script). The ALMA calibrator database shows that this source had a measured flux of 630 mJy when observed 12 days later at the same frequency. The continuum was imaged from line-free channels in all four spws. This continuum image, at an effective frequency of 239

GHz, was made using 'Briggs weighting' with robust=2, i.e. 'natural' weighting. The synthesized beam of this image has a major (minor) axis of $0\farcs71$ ($0\farcs61$) in PA 85° and the r.m.s. noise is 0.023 mJy/beam. The continuum-subtracted uv-data were then used to image the CO J:2-1 line. The final CO J:2-1 data we use and show in this work come from two datacubes: (a) a higher spatial and spectral resolution cube, made using 'Briggs weighting' with robust=0.2, and using the intrinsic spectral resolution. This datacube has a synthesized beam with major (minor axis) of $0\farcs58$ ($0\farcs5$) with a beam PA of $-72°$and an r.m.s. noise of 0.7 mJy/beam per 2.5 km/s channel; (b) a lower spatial and spectral resolution (but higher signal to noise) cube, made using 'natural' weighting, and 4-channel spectral averaging. This datacube has a a synthesized beam with major (minor) axis of $0\farcs73$ ($0\farcs62$) with a beam PA of 86°and an r.m.s. noise of 0.45 mJy/beam per 10 km/s channel.

2.3 Results

2.3.1 Stellar kinematics

The stellar kinematics was obtained from the absorption lines in the Gemini GMOS/IFU datacube. To model the stellar kinematics we used the penalized pixel-fitting (pPXF v5.2.1) routine developed by Cappellari & Emsellem (2004) and upgraded in Cappellari (2017), where the line-of-sight velocity distribution (LOSVD) is recovered by fitting an optimized template to the galaxy spectrum. We used the INDO-US spectral templates library (Valdes et al. 2004). To reach the highest possible S/N to measure the stellar kinematics reliably, we spatially binned the data cube (S/N = 50) by using the Voronoi binning method described in Cappellari & Copin (2003). The spectra show no absorption lines in the region near the northern radio lobe: this region was thus masked before running pPXF.

The pPXF-derived stellar kinematic velocity map is shown in Fig. 2.2. Throughout this paper we adopt an inclination of 25° based on the axis ratio $a/b = 1.1$ (v1.10, de Vaucouleurs et al. 1991). We model the stellar velocity field obtained from pPXF using a spherical potential with pure circular rotation, assuming that the kinematical center is cospatial with the peak in the continuum emission. The observed radial velocity from this potential is given by (Bertola et al. 1991):

$$V = V_{sys} + \frac{AR\cos(\psi-\psi_0)\cos^p\theta}{(R^2[\sin^2(\psi-\psi_0)+\cos^2(\psi-\psi_0)]+c^2\cos^2\theta)^{p/2}} \, ,$$

where V_{sys} is the systemic velocity, R is the radius, θ is the disk inclination, ψ_0 is the position angle of the line of nodes, A is the amplitude of the rotation curve, c is the concentration parameter regulating the compactness of the region with a strong velocity gradient, and p regulates the slope of the 'flat' portion of the velocity curve. We perform a least-square minimization using the IDL routine MPFIT2DFUN (Markwardt 2009) to obtain the best fitting parameters. The resulting model is shown in Fig. 2.2, where we kept center and inclination (25°) fixed, and the free parameters of the fit and the best fitted values were: $A = 207$ km/s, $c = 0.82$, $p = 1$, $\Psi_0 = 40°$.

2.3.2 Ionized gas

To model the ionized gas emission in the GMOS-IFU data we use custom IDL routines, based on the routine PROFIT (Riffel 2010), fitting a Gaussian profile to the emission lines of the GMOS-IFU spectra. We begin our analysis by generating moment images for the most prominent spectral emission lines, [OIII]λ5007 and the [NII]$\lambda 6549, \lambda 6585$ doublet.

The moment zero, i.e., integrated flux maps (Fig. 2.3) show an S-shaped morphology of the ionized gas, where two arm-like features leave the center as a straight line along PA 55° and then curve, to the NW in the NE arm, and to the SE in the SW arm. The brightest emission is observed within an opening angle of 90° from the nucleus. The black contours in the [NII] moment zero map (Fig. 2.3) correspond to the 8.4 GHz VLA map, and indicate that the gas in the S-shaped arms seems to surround both NE and SW radio lobes. This morphology, and the interaction between radio jet and ionized gas, was previously observed and analyzed by Cooke et al. (2000), and Maksym et al. (2017).

Moment one, i.e., velocity maps, are shown in the second column of Fig. 2.3, where a gradient can be observed from NE to SW. However, given the complex kinematics of the NLR a precise determination of its PA is not possible using this moment image. Two high-velocity features are found to the NE and SW of the nucleus. The moment one map for the [OIII] emission line shows that a redshifted component covers a large fraction of the FOV.

The moment two (velocity dispersion) maps, shown in the third column of Fig. 2.3, presents a large dispersion in the central region, extending from the center in a section along the minor axis (referred to as the equatorial region hereafter), and a second high dispersion area is seen in the inner part of the NE arm. The dispersion is higher for the [OIII] emission line.

The moment 3 (h3) map (bottom-right corner in Fig. 2.3) obtained from a one-component Gaussian fit, describes asymmetric deviations from a Gaussian profile, presents some skewness in the equatorial region, where negative values are indicative of a blueshifted wing or component. A large area in the SE region present a positive skewness, which indicates a strong redshifted wing or component. Similar distributions were observed for all moment maps of all strong emission lines fitted with a single Gaussian using PROFIT ([SII], Hα, Hβ, [OI]; not shown).

To better examine the kinematics we defined a curved 'slit' along the S-shaped arms: the aperture positions extracted for the slit and the position-velocity (pv) diagrams extracted centered on $H\alpha$ are shown in Fig.2.4. In these diagrams we clearly see the presence of multiple kinematic components. The main component seems to follow the rotation pattern of a disk. Redshifted components can be observed near both NE and SW radio lobes. A high (1000 km/s) weak component can be observed near the NE radio lobe. A high-velocity blueshifted component is visible south from the nucleus.

The kinematics of NGC 3393 were classified as turbulent by Fischer et al. (2013), based on HST spectroscopy, since they could not be satisfactorily fitted with a biconical outflow model. Given the complex kinematics of the NLR, the large velocity dispersion, the Gaussian skewness observed in the equatorial region, the multiple kinematical components observed in the pv-diagram, and a visual inspection of the spectra in the mentioned areas (Fig. 2.5), the need for a multiple-component Gaussian fit is clear.

For the multi-component analysis we performed a three-component Gaussian fit to the emission lines. We use a narrow component ($\sigma < 115$ km/s), a broad redshifted component ($115 < \sigma < 230$ km/s), and a third broad blueshifted ($115 < \sigma < 230$ km/s) component, based on a visual inspection of the spectra in the equatorial region (Fig. 2.5) and the large velocity dispersion of this area. Note that the 'broad' nomenclature used here should not be confused with the broad component typical of a Type 1 AGN.

The result of the multiple-component fit is shown in Figure 2.6; the narrow component traces gas rotating in a disk, with kinematic major axis in PA 40°, and the broad components trace complex kinematics closely related to the radio jets. Two outflows can be inferred from the broad redshifted components in the far side of the galaxy (marked as 'O1', 'O2' and 'O3' in Fig. 2.6). These components are most likely connected to the NE and SW radio lobes. A third, high-velocity outflow can be inferred from the third broad blueshifted component (velocity peak is marked as 'O4' in Fig. 2.6); this blueshifted emission extends along the equatorial region.

2.3.3 Molecular gas : CO J:2-1

To illustrate the distribution of the molecular gas relative to the other components of the galaxy we show in Fig. 2.8 both the CO J:2-1 (ALMA; cyan) and [NII] (Gemini-GMOS/IFU; black) integrated flux maps overlaid on an HST F606W image to which we applied an unsharp-mask filter, with the goal of emphasizing structures, such as dusty regions (we refer to this filtered image as 'structure map' from now on). It can be observed that the ionized and molecular gas barely overlap, due to the limited FOV of our GMOS-IFU data. There is little to no CO J:2-1 molecular gas observed in the central region, which can be a critical density effect or a true lack of molecular gas. The outer distribution of CO J:2-1 seems to follow the inner ring-like structure, where the structure map shows the presence of dust. The observed molecular gas morphology in the nuclear region could be a result of the molecular gas and radio jet interaction: the latter can produce entrainment of the gas along the jet P.A, and push gas away from the center perpendicular to this PA. Alternatively, the molecular gas density is high enough that the CO J:2-1 transition is 'dark' and a dense molecular gas tracer is required.

The CO J:2-1 moment 0 map is shown in Fig. 2.9: the distribution of the molecular gas is fragmented and does not cover a large fraction of the field of view. The SE component close to the center is the region with the brightest CO J:2-1 emission. The outer region show large scale spiral arms that broadly resemble a ring. There is some emission present in the region between the SE component and the outer arms.

Figure 2.9 presents the CO J:2-1 moment 1 map. We classified the kinematics in two regions, an inner region inside a circle of $5''$ (marked in gray in Fig. 2.9) and an outer region, outside this circle. We can see a gradient in velocity from NE to SW in the outer distribution of gas, as it is expected for gas rotating in the disk. However, in the inner region the kinematics does not follow the outer region's rotation: in the SE inner component there seems to be a gradient of velocity in PA $-45°$, and the NW inner component shows mainly blueshifted velocities.

We model the kinematics in the outer region with a pure circular rotation model obtained from an exponential disk potential, defined by:

$$\Phi(R,z) = -2\pi G\Sigma_0 r_d^2 \int_0^\infty \frac{J_0(kR)e^{-k|z|}}{[1+(kr_d)^2]^{3/2}} dk \ ,$$

where (R,z) are cylindrical coordinates, G is the gravitational constant, Σ_0 is the central surface brightness, r_d is the disk scale length, and J_0 is the zeroth order cylindrical Bessel function. For this model we assume an infinitesimally thin disk ($z \to 0$). The rotation velocity from this potential is given by

$$V_{ROT}^2(R) = R\frac{\partial \Phi}{\partial R}$$

We perform a least-square minimization (using the MPFIT2DFUN routine in IDL) to obtain the parameters that best fit the observed CO J:2-1 velocity field (Fig. 2.10). The PA cannot be well constrained due to the scarcity of the data along the major axis, we thus fix the major axis PA to 40° (See Sect. 5) after verifying that the velocity profiles of the CO J:2-1 along, and near, the minor axis is most consistent with this major axis PA (e.g., Fig. 2.11), and also fix the inclination to $i = 25°$. Based on the rotation curve along the minor axis, we use a -26 km/s offset from the systemic velocity (Meyer et al. 2004, $V_{sys} = 3746$ km/s from HIPASS;), to better fit the CO J:2-1 data. For the free parameters r_d and M_d, the mass and scale length of the disk respectively, the best fitted values obtained are $r_d = 1$kpc and $M_d = 2.7 \times 10^{10}$ $M_\odot$. For comparison, the values obtained by the HST light distribution modeling of Läsker et al. (2016) are $r_d = 1.38$ kpc and $M_d = 2.04 \times 10^{10}$ M_d. The resulting exponential disk model and the residual from the model subtraction to the CO J:2-1 velocity map are shown in Fig. 2.10. The rotation curves of the CO J:2-1 and the exponential disk model are shown in Fig. 2.11.

The velocity dispersion (moment 2) map is shown in the rightmost panel of Fig. 2.9: the highest values are observed in the inner region, with the highest dispersion found in the SE component. Example spectra of this region can be found in Fig. 2.12.

The pv-diagram taken along a slit of PA $-50°$ (Fig. 2.15), centered on the SE feature, shows a clear gradient in velocity along the SE feature. A second pv-diagram extracted along the minor axis, centered on the galaxy center, using a natural weighted, 4-channel averaged image (10 km/s) is shown in Fig. 2.15. The clear gradient of the SE component seems to follow a PA close to the minor axis, and to the PA of the nuclear bar (Fig. 2.8). The unusual kinematics of this inner region is addressed in Sect. 2.4.5, where we argue that it is a possible result of the interaction between the large scale bar and the nuclear bar. The total CO mass of the SE feature is $M(H_2) = 5.4 \times 10^7$ $M_\odot$, asumming $\alpha_{CO} = 4.6 M_\odot$ (K km s^{-1} pc^2)$^{-1}$. If the all the molecular mass enclosed in the SE feature was inflowing with a velocity of 10 km/s, the potential accretion rate produced would be 0.32 $M_\odot$/yr.

2.4 Discussion

The main nuclear radio features of the galaxy are the nuclear component, with a flat spectrum, and two hotspots, NE and SW from the nucleus, with a steeper spectrum. This structure is indicative of a two-sided jet. The larger flux in the SW lobe is attributed to Doppler boosting by Koss et al. (2015), assuming that the NE component is receding and the SW is approaching. There are no other previous studies that allude to the jet position in the galaxy in greater detail.

Based on the kinematics presented here, the maser disk orientation, which is edge on and in PA roughly parallel to the minor axis of the galaxy, which indicates that the jet is aligned almost along the major axis, and the relatively low inclination of the galaxy disk, we interpret the jets as being launched into the disk of the galaxy and in PA close to the major axis of the galaxy, with the SW radio lobe starting to leave the galaxy disk. This scenario implies a maximum interaction between the radio jet and the dense gas in the galaxy disk.

2.4.1 Jet driven outflow

The multi-component Gaussian fit to the [OIII] emission line shows three high-velocity redshifted regions in the broad redshifted component, $1''$ NE, $1''\!.8$ NE and $1''\!.4$ SW of the nucleus, near the NW and SE radio lobes (marked as 'O1', 'O2' and 'O3' in Fig. 2.6). The narrow [OIII] component, originated in the rotating gas is also perturbed in these areas. The 'O3' outflow is located near the SW radio lobe, in an area with lower extinction and higher densities as indicated by the $[SII]\lambda6716/\lambda6731$ and $H\alpha/H\beta$ line ratios respectively (Fig. 2.7), which can indicate that the SW radio jet is coming out of the disk of the galaxy, pushing the gas on the disk behind it, away from the line of sight. The 'O2' outflow seems to be gas being pushed by the jet, the velocities observed in the redshifted gas suddenly increase by a factor of 2.5 (this can also be observed in Fig. 2.4b), which is to be expected by the galaxy inclination of 25° and may indicate that the 'O1' outflow is caused by the bending of the NE jet towards the line of sight, which seems to leave the galaxy at the middle of the radio lobe and thus the 'O1' velocities are true velocities from gas leaving the galaxy disk.

To estimate the ionized gas outflow rate we estimate the mass of the gas and the velocity of the outflow, following Lena et al. (2015). The gas mass is given by

$$M_g = N_e m_p V f \tag{2.1}$$

where N_e is the electron density, m_p is the proton mass, V is the volume considered and f is the filling factor, which can be estimated by

$$L_{H_\alpha} \sim f N_e^2 j_{H_\alpha}(T) V \tag{2.2}$$

where L_{H_α} is the H_α luminosity emitted by the volume V, and $j_{H_\alpha} = 3.534\times10^{-25}$ erg cm^{-3} s^{-1} (Osterbrock 1989). Combining these two equations we obtain:

$$M_g = \frac{m_p L_{H_\alpha}}{n_e j_{H_\alpha}(T)} \tag{2.3}$$

To estimate the outflow rate we use an aperture of $0\farcs6$ for each component. For the 'O1' outflow, the mean $[SII]\lambda6716/\lambda6731$ line ratio of the broad redshifted Gaussian component is 0.87, which corresponds to an electron density of 910 cm^{-3}, the Hα luminosity of the same Gaussian component in this aperture is 2×10^{40} erg s^{-1}, and the gas mass that is outflowing, assuming a luminosity distance to the galaxy of 52 Mpc, is 5×10^4 $M_\odot$; The mean radial velocity in the aperture is 232 km/s, which we assume to be the true velocity. This gives an outflow rate for 'O1' of $\dot{M} = 0.08$ M$_\odot$/yr. For 'O2', the electron density is 638 cm^{-3}, the mass is 1.4×10^4 M$_\odot$. The mean radial velocity is 168 km/s, and assuming the gas remains in the disk, the deprojected velocity is 226 km/s. Thus, the outflow rate for 'O2' is $\dot{M} = 0.08$ M$_\odot$/yr. The 'O3' outflow has an electron density of 1513 cm^{-3}, a Hα luminosity of 7×10^{39} erg s^{-1}, and a mass of 1×10^4 $M_\odot$, the mean velocity in the aperture is 274 km/s, which we assume to be gas outside the disk and travelling along our line of sight (i.e. we directly observe the intrinsic velocity). Under these assumptions, the outflow rate for this aperture is $\dot{M} = 0.02$ M$_\odot$/yr.

2.4.2 Equatorial outflow

The [OIII] multi-component Gaussian fits shows the presence of a strong broad blueshifted component along the equatorial region, on a strip $\sim 1''$ wide along PA 147°. The velocity map of this component is shown in Fig. 2.6 (center marked as 'O4') where high blueshifted velocities can be observed in the equatorial region, perpendicular to both the galaxy disk PA and the radio jet axis. The presence of a weak redshifted component can be inferred from a redshifted wing, visible on a large fraction of the equatorial region, however the low flux in this wing does not allow for a confident Gaussian fit. This distribution and the presence of a blue component (and possibly a redshifted component as well) in the region perpendicular to the radio jet axis indicates the presence of an equatorial outflow along PA 147°, which is in good agreement with the water maser disk PA. In this scenario the redshifted component will be behind the galaxy disk and thus will appear weaker due to obscuration in the disk (Fig. 2.7). Although the presence of outflows along the radio jet is more common (e.g. Das et al. 2007; Barbosa et al. 2009; Storchi-Bergmann et al. 2010), equatorial outflows have been included in theoretical models of accretion disk winds (Li et al. 2013), and outflowing torus models (Hönig et al. 2013; Elitzur 2012), and observationally found in NGC 5929 (Riffel et al. 2014, 2015).

In this scenario, and given that the galaxy is almost face-on, we assume that the blueshifted gas is in front, and possibly leaving, the disk and the redshifted gas is behind. The mean $[SII]\lambda6716/\lambda6731$ line ratio of the blue component in the equatorial region is 0.9 which corresponds to an electron density of 800 cm^{-3}. The H_α luminosity of the region is 1.3×10^{40} erg s^{-1}. From Eqn. 2.3 we obtain a mass of $M_g = 3.5 \times 10^4\ M_\odot$, the mean observed velocity is -250 km/s and we consider this to be the true velocity of the gas, i.e. this outflowing gas is not in the plane of the disk.
The estimated equatorial outflow rate, under these assumptions, is $\dot{M} = 0.2$ M$_\odot$/yr. An alternative method to derive the equatorial outflow rate is to assume a hollow cylinder geometry that is expanding from the center, with a height of $0\farcs5$. In this case the estimated outflow rate is 5 M$_\odot$/yr, assuming a filling factor $f = 0.01$ (following Riffel et al. 2015). The differences in these two outflow rate estimates suggests the need of a filling factor closer to $\sim$0.001 or a significantly smaller height.

If we consider a symmetric component (behind the disk) for the 'O2' and 'O4' outflows considered above, the total mass outflow rate can reach $\dot{M} \sim 0.66$ M$_\odot$/yr. The outflow rates presented here are a lower limit, as we only consider the ionized

gas.
To contrast the outflow rates estimated here, we now estimate the inflow rate necessary to feed the SMBH. The bolometric luminosity estimated using the 2-10 keV luminosity is $2.4 \times 10^{44} - 7.6 \times 10^{44}$ erg/s (Kondratko et al. 2008). Assuming a standard accretion efficiency of 10% the accretion mass rate required is $\dot{M} = 0.04 - 0.1$ $\mathrm{M}_{\odot}$/yr, a factor ~ 7 lower than our estimated outflow rate, which is not unusual in nearby galaxies (Barbosa et al. 2009; Müller-Sánchez et al. 2011). The difference between inflow and outflow rates can indicate that the outflowing gas does not originate from close to the central engine, but is circumnuclear ISM gas that is being pushed away by the radio jet. While we do not find direct evidence of inflows in the ionized gas, as discussed in Sect. 2.3.3, if the SE component of the observed CO J:2-1 molecular gas was inflowing with a velocity of 10 km/s the necessary inflow rate could be achieved.

2.4.3 Bar perturbations

To understand the role of the bar-induced perturbations to the molecular gas kinematic we have applied the harmonic decomposition formalism described in Schoenmakers et al. (1997b) and Wong et al. (2004). It is important to remark that this formalism is based on linear epicycle theory, and thus it is only valid for weak bars, as the departure from circular orbits must be small compared to the circular velocity. The line of sight velocity towards a given point in a galaxy velocity field can be decomposed in a Fourier series as:

$$V_{LOS}(R) = c_0 + \sum_{j=1}^{n} [c_j \cos(j\psi) + s_j \sin(j\psi)] \sin i \ ,$$

where (R, ψ) are polar coordinates, i is the inclination of the disk, c_0 corresponds to the systemic velocity (V_{sys}), and j is the harmonic number. The coefficients c_j and s_j are a function of the circular velocity (V_c), the bar pattern speed (Ω_p), ellipticity of the potential (ϵ) and the bar viewing angle (θ_{obs}), which corresponds to the bar PA from the minor axis of the galaxy disk (see e.g. Fig. 2 of Wong et al. 2004, for a definition of this angle). A bar creates a bisymmetric gravitational potential which has a predominant $m = 2$ Fourier component, and thus we only consider the harmonics $j = m - 1$ and $j = m + 1$ (Schoenmakers et al. 1997a). For the circular velocity (V_c) we used the value obtained from the best fit exponential disk potential (Fig. 2.10 and Sect. 2.3.3).

A constant damping term (λ), simulating a radial frictional force, is introduced (e.g. Lindblad & Lindblad 1994; Wada 1994) to avoid sudden changes in orbit axes and thus multiple orbits at a given point. Usual values for this parameter are in the range $0.05 < \lambda < 0.4$. Note that the epicycle approximation breaks down at corotation, where the orbits change direction.

For the case of NGC 3393, Ω_p and λ are the parameters with the largest uncertainties. We thus build a library of models with different parameter combinations, a section of which is shown in Fig. 2.13, where the two parameters are varied over $0.01 < \lambda < 0.2$ and $25 < \Omega_p < 85$ km/s/kpc. The primary effect of changing Ω_p is the variation in the radii of the resonances, but it also effects the magnitude of twists in the isophotes. The effect of increasing λ is to smoothen the sudden twists seen near the resonances.

We attempted to fit the full CO velocity field to this perturbation theory model, with Ω_p and λ as free parameters, and the perturbations terms set by the large-scale bar PA and ellipticity. However, we could not find any suitable set of parameters (even if the bar PA was varied) which could match both the outer CO velocities and the highly perturbed velocities in the SE inner CO component. We are thus forced to conclude that a single $m = 2$ (i.e. bar) mode is unable to explain the complex molecular kinematics seen in NGC 3393. The remaining option is thus to attempt to separately fit perturbations in the large-scale molecular kinematics (driven by the large-scale bar) and in the inner molecular kinematics (driven by the nuclear bar), which we do in the following subsections.

2.4.4 Large-scale bar

To obtain the (large-scale) bar perturbation model which best fits the outer CO kinematics we fit the observed CO velocity field (outside the grey circle in Fig. 2.9) to the predictions of our bar-perturbation models by using the same least-square minimization routine as explained above, in order to obtain the best-fitted parameters. We fix the exponential disk model parameters to those obtained above. We also fix the ellipticity of the potential ($\epsilon = 0.15$) and the bar PA ($PA_{bar} = 160°$) to the values obtained for the large-scale bar by Jungwiert et al. (1997). The free parameters are thus the damping term (λ) and the bar pattern speed (Ω_p).

The resulting best-fit model obtained and its velocity residuals are shown in Fig. 2.14. The r.m.s. of this residual map is lower than that obtained when only the pure rotational model of the exponential disk is used, though the difference is not large. To further test the suitability of the best fit model we compare the model with data extracted along the minor axis in the pv-diagram shown in Fig. 2.15. In the outer region, both model and data are close to zero as expected along the minor axis, however the model does not fit the data in the inner region, where the large velocity gradient of the SE feature is observed.

An interesting aspect of the best fitted model, as well as many of the models shown in Fig. 2.13, is the presence of two resonances, an inner resonance that encloses the nuclear region, including both SE and NW features, and an outer resonance which encloses the outer distribution of molecular gas. These two resonances could help explain the difference in PA of the ALMA and GMOS data compared to the large-scale kinematics position angle (PA = 68 °, according to Cooke et al. 2000). It is also interesting to note that the kinematics enclosed in the inner resonance resemble the observed stellar velocity map, specially the S-shaped zero velocity line (Fig. 2.2).

The primary limitation in the analysis above is the sparse filling factor of CO velocities over the FOV. Deeper integrations with ALMA are thus crucially required. Alternatively, deep observations of the ionized gas kinematics over the full galaxy (using e.g., VLT/MUSE) are required. Indeed, the latter have been recently obtained by another team.

2.4.5 Nuclear bar

The presence of an additional nuclear bar has been suggested by NIR imaging (Alonso-Herrero et al. 1998) and by light distribution modeling from HST imaging (Läsker et al. 2016). The extension of (SMA) this nuclear bar is $\sim 2''$, and it is offset from the large scale bar by $10° - 20°$.
Considering that both the PA and extension of the inner features of our CO J:2-1 data agree with those of the nuclear bar, we build bar perturbation models for the nuclear bar (Fig. 2.16), assuming that the nuclear bar is decoupled from the large-scale bar and thus has a larger pattern speed. The disk parameters (exponential disk parameters, disk PA and inclination) were kept fixed to the values used above. Typical ranges were assumed for the free parameters: $0.15 < \lambda < 0.4$, $0.1 < \epsilon < 0.8$, $10 < \Omega_p < 200$ km/s/kpc. The best fitted values obtained were: $\lambda = 0.1$, $\Omega_p = 73$ km/s/kpc and $\epsilon = 0.35$, and $\theta_{obs} = -85°$. The latter value implies that the large-scale and nuclear bars are almost aligned, and that the nuclear bar is completely embedded in the large-scale bar; which is consistent with the results of Alonso-Herrero et al. (1998), where the PA difference between both bars is in the range $10° - 20°$. The resulting model is overlaid on the PV-diagram along the minor axis (Fig. 2.15),

where it can be observed that it follows the same gradient of the inner SE feature and the Keplerian-like fall-off, while it is also close to the gradient of the inner NW feature.

Considering that we can reproduce a similar gradient as that observed in the inner SE feature, it is possible that an interaction of the large-scale bar and the nuclear bar exists. If these components present kinematical coupling, they can share a resonance, usually the ILR for the large-scale bar coincides with the CR of the nuclear bar. If this is the case for NGC 3393 it is possible that the molecular gas observed is near the ILR of the large-scale bar where it can accumulate into rings. However, the presence of an inner bar could, in principle, allow the gas to overcome this limit and continue to flow to the central regions (Shlosman et al. 1989).

This simple toy model indicates that it is feasible that a large-scale and nuclear bar interaction can produce a feature similar to the one observed in the inner region of our ALMA data. However, the kinematical coupling between both bars and the consequent complex modeling of its effect is beyond the scope of this paper.

Evidence for a secondary SMBH has been presented by Fabbiano et al. (2011). This BH is located $0\farcs6$ SW from the nucleus (Fig. 2.3). As it can be seen in the moment 1 maps of the ionized emission lines, there is no clear kinematical component connected to the position of this posited secondary BH. However, the kinematics of the ionized gas are deeply perturbed by the radio jet and thus any kinematical signature of a secondary SMBH can be easily lost.
An alternative explanation to the unusual gradient observed in the SE component of the molecular gas might be linked to this posited secondary SMBH. A pv-diagram along a PA of 50° centered on the feature (Fig. 2.15) shows a mostly smooth gradient that goes from ~ -100 km/s to ~ 100 km/s, which could indicate a nuclear disk related to the secondary SMBH. However, the kinematic and morphological center of the SE feature does not corresponds to the posited position of the secondary BH. Alternatively, the inner CO emission (i.e. both the SE and NW inner components) could be centered around the secondary SMBH; although we cannot rule out this case, it would require a very special geometry. Simpler explanations, such as the nuclear bar perturbations are thus favored by us. A map of the millimeter continuum close to the CO line (Fig. 2.12) shows three components whose positions correspond closely to the radio lobes observed in the VLA 8.4 GHz data. The 230 GHz total fluxes are 0.2 mJy for the nuclear source, 0.31 mJy for the SW source, and 0.08 mJy for the NE source. The posited secondary SMBH is located in between the nuclear and the SW source, and while there is no clear detection of another source in that position, the presence of another continuum source here cannot be discarded

unequivocally. Thus, while we find no evidence supporting the existence of this secondary SMBH, it is important to note that both the observational and interpretive constraints are not strong enough to disprove the presence of the secondary SMBH.

2.5 Conclusions

We have analyzed the kinematics of the stars, ionized gas, and molecular gas in the central kpcs of the Seyfert 2 galaxy NGC 3393 using optical integral field observations from Gemini/GMOS-IFU and ALMA. From our detailed analysis of these data we conclude that:

- NGC 3393 presents a complex multi-phase ISM, with strong interactions betweeen the nuclear radio jet and the ionized gas produces complex kinematics. We have found that it is necessary to fit the emission line profiles observed with multiple Gaussian components. We identify three components in the ionized gas, which we refer to as the narrow, broad redshifted, and broad blueshifted components.

- The narrow ionized gas component has a low velocity dispersion ($\sigma < 115$ km/s) and mostly follows pure rotation in the galaxy disk; nevertheless this component is perturbed in the regions near the radio lobes.

- The broad redshifted component ($115 < \sigma < 230$ km/s) can be observed in regions near the radio lobes. We identify three outflows in this component named as 'O1', 'O2' and 'O3'. Both 'O1' and 'O2' seem associated to the NE radio lobe, while 'O3' is near the SW radio lobe. The 'O2' outflow is redshifted on the far side of the galaxy which can indicate gas being pushed away by the radio jet. The 'O1' outflow seems to be the result of the jet bending and leaving the galaxy in this region, pushing gas in the disk away from the line of sight. As the SW radio lobe appears to be the approaching component of the radio jet, it's possible that this jet is starting to leave the galaxy in the region of the 'O3' outflow, and thus the redshifted gas observed can be gas in the disk, being pushed away from the line of sight by the radio jet.

- The broad blueshifted component ($115 < \sigma < 230$ km/s) presents large blueshifted velocities distributed along the equatorial region, perpendicular to the radio jet axis. A weak redshifted wing it is also visible in the same region, but due to its low flux we could not fit it with confidence. We interpret this component as being part of an equatorial outflow, expanding perpendicular to the radio jet axis, and whose emission is attenuated by dust in the plane of the galaxy.

- From the measured velocities, H_α fluxes, and electron densities, of the outflowing components, we estimate a total outflow rate of $\dot{M} \sim 0.125$ M$_\odot$/yr for the jet driven outflows, and $\dot{M} \sim 0.2$ M$_\odot$/yr for the equatorial outflow. If we consider a symmetric component for each of the 'O2' and 'O4' outflows observed, the total outflow rate can reach $\dot{M} \sim 0.65$ M$_\odot$/yr for the ionized gas. This outflow rate is 7 times larger than the accretion rate necessary to fuel the AGN. While we found no direct evidence for gas inflows, we note that the necessary inflow rate can be provided if the SE component of the CO J:2-1 emission is inflowing at a velocity of $\sim$ 10 km/s, a velocity which would be close to the detection limit of our observations and analysis.

- We were forced to analyze the kinematics for the CO J:2-1 emission separately for two regions, an inner region within 5$''$ of the nucleus, and the region outside said circle, since we could not find a global model which could fit both regions together. We do not detect CO J:2-1 emission at either position of the SMBH or at the position of the posited secondary SMBH.

- The outer region of the CO J:2-1 emission seems to trace the rotation in the outer disk, and can be fitted with an exponential disk rotation model, though obvious residuals remain. To understand the role of the large-scale bar in the kinematics observed on the CO J:2-1 emission we applied the harmonic decomposition formalism to the CO velocity field. Specifically, we fitted a bar-perturbation model to the outer region of our CO J:2-1 velocity field. We found, over a range of different Ω_p and λ, the presence of a resonance between the inner and outer region, and a resonance that encloses the outer region of the CO emission. These resonances could explain the difference in PA found in the ALMA and GMOS/GEMINI data compared to the large-scale kinematics observed by Cooke et al. (2000), and the observed distribution of CO J:2-1 emission. This model, however, does not fit the observed CO kinematics of the inner region.

- The inner region of the CO J:2-1 emission presents highly disturbed kinematics, with the presence of an off-nuclear velocity gradient centered in the SE component. We found this gradient can not be explained by the large-scale bar model, nor by the presence of the posited secondary SMBH or any disk related to it. We fitted a second bar perturbation model based on the parameters of the nuclear bar and found a good fit to the inner region kinematics. This toy model indicates that the kinematics observed in the inner region of the CO J:2-1 emission can be attributed solely, or at least dominantly, to perturbation by the nuclear bar, together with interactions between the large-scale and nuclear bars.

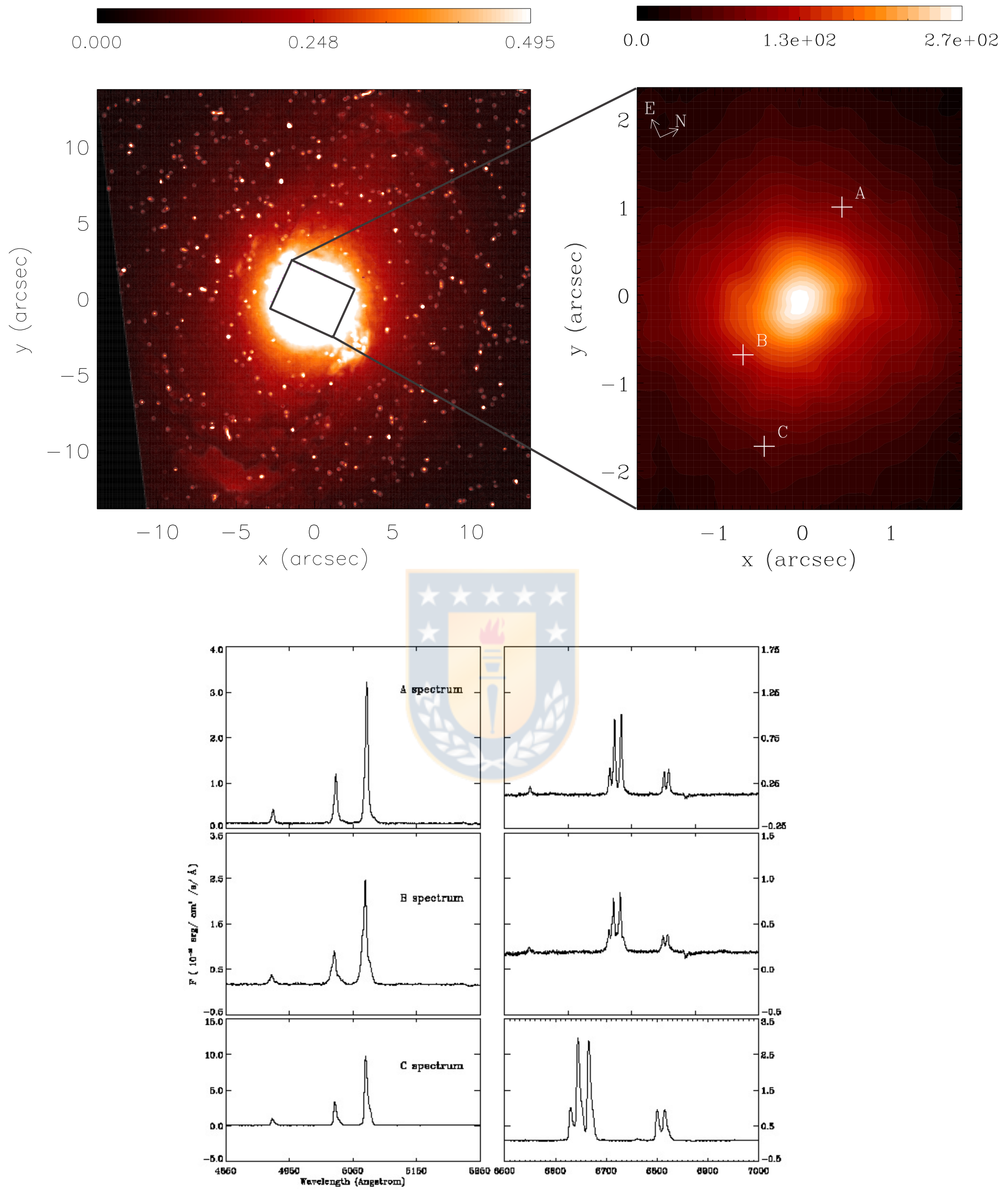

Figure 2.1: Top left: HST F606W image for the galaxy, overlaid with the GMOS FOV; Top right: GMOS continuum image, made by collapsing channels of the data cube that did not include strong emission lines. Lower six panels: Example spectra for the three points marked on the continuum map, showing the most prominent emission lines [OIII], [NII], H_α, and [SII]. Source: Finlez et al. (2018).

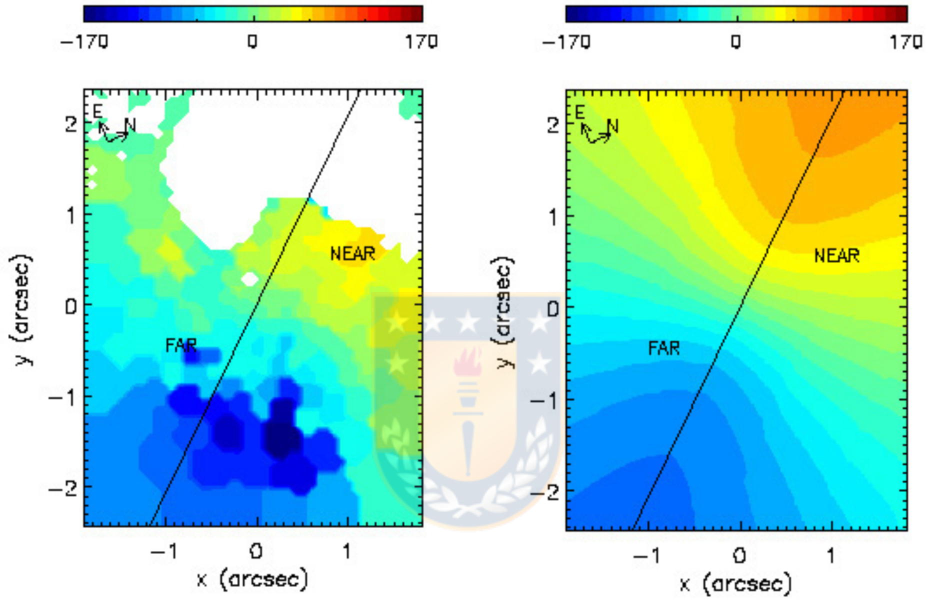

Figure 2.2: Left: Stellar velocity map from pPXF; regions where no absorption line information could be recovered are masked. Right: best-fit Bertola model to the stellar velocity field; center and inclination ($i = 25°$) were kept fixed. The free parameters fitted were $A = 207$ km/s, $C = 0.82$, $p = 1$, and $PA = 40°$. Source: Finlez et al. (2018).

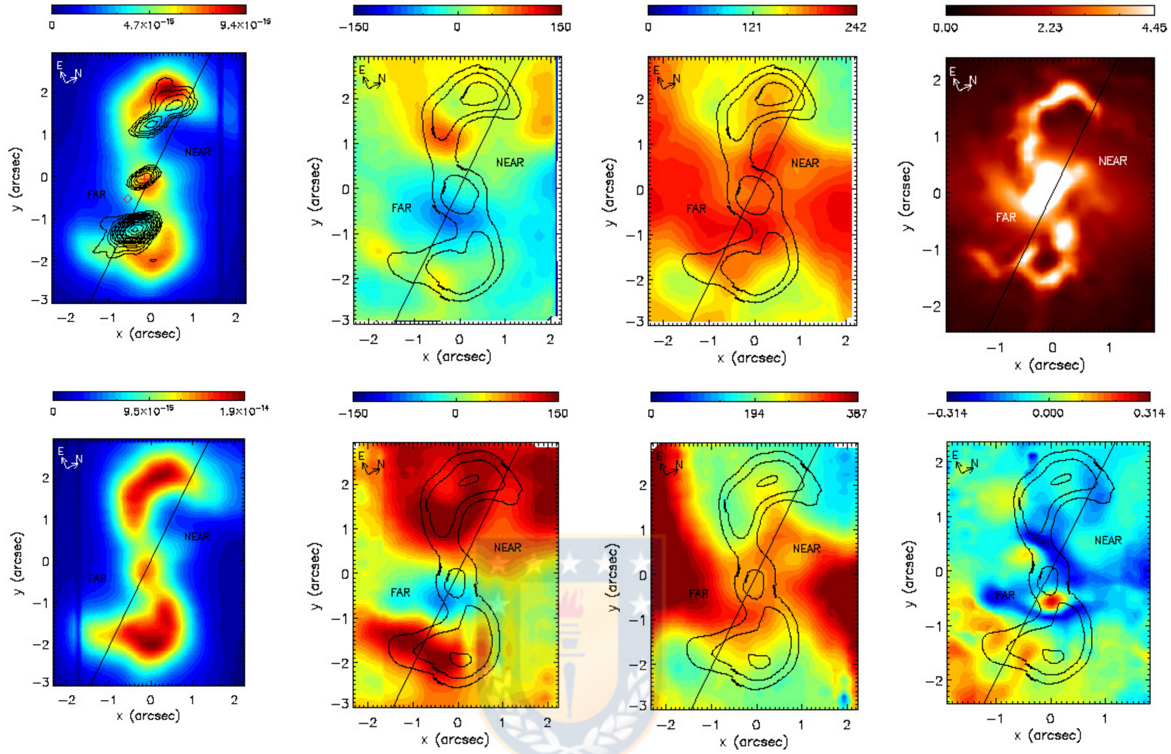

Figure 2.3: Moment maps for the [NII]λ6585 (top) and [OIII]λ5007 (bottom) emission lines. First column: integrated flux, second: velocity map, third: velocity dispersion. The fourth column shows the structure map (top) and the h3 moment (bottom) from a one-component Gaussian-hermite fit to the [OIII] emission line, this moment represents the asymmetric deviations from a Gaussian profile. Black contours superposed on the moment 0 map of the [NII] line correspond to the VLA 8.4 GHz map. Black contours in the moment 1, 2 and 3 maps correspond to the moment 0 of the respective line. The galaxy major axis (PA 40°) is marked as a black line, delimiting the near and far side. The compass shown on top left corner shows the orientation of our GMOS/Gemini data. The red cross marks the position of the stellar continuum peak, which we assume to trace the position of the nucleus. The red diamond shows the position of the SW secondary BH reported by Fabbiano et al. (2011). Source: Finlez et al. (2018).

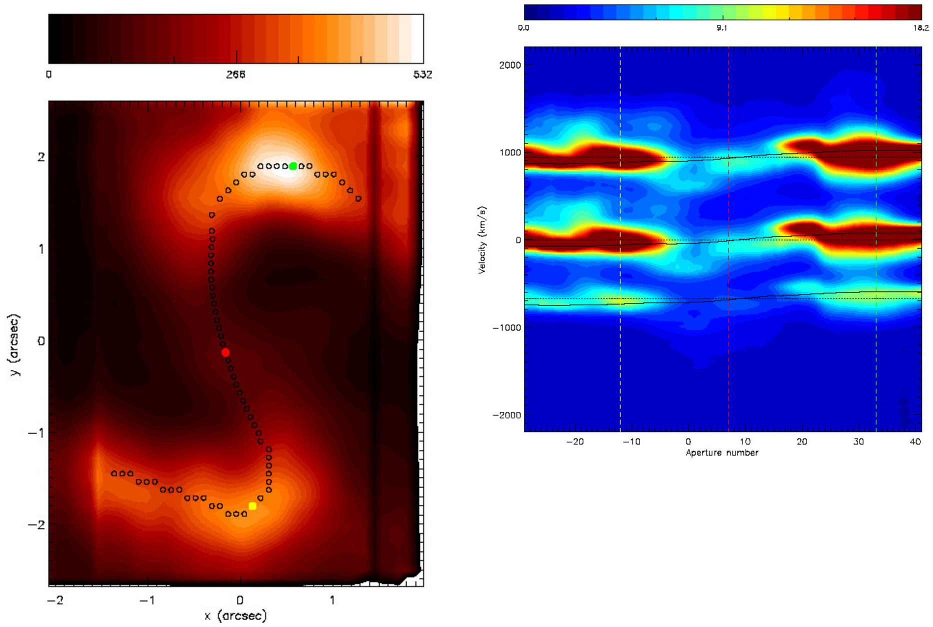

Figure 2.4: Left: our S-shaped 'slit' overlaid on the [NII] moment zero. The colored apertures can be used as reference in the pv-diagram. Right: position-velocity diagram of the continuum-subtracted GMOS data cube, centered on the H_α emission line, extracted along the S-shaped 'slit' shown on the left figure. The solid black line shows the expectations of the Bertola rotation model derived from the stellar kinematics. For reference, vertical green, maroon and blue lines show the position of specific apertures in the left figure. The dashed black lines show the zero-velocity for each emission line. Source: Finlez et al. (2018).

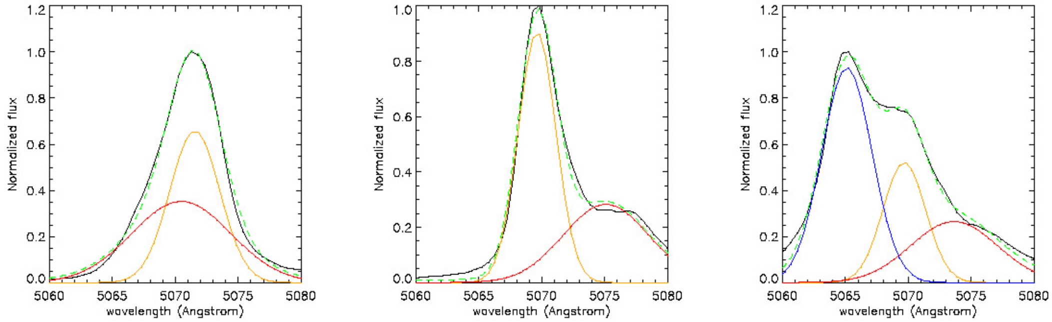

Figure 2.5: Examples of multiple-component Gaussian fits to the [OIII] emission line in the 'O2', 'O3', and 'O4' (left to right) areas shown in Fig. 2.6. The narrow, broad redshifted, and broad blueshifted components are shown in yellow, red, and blue, respectively and their sum is shown by the dashed green line. Source: Finlez et al. (2018).

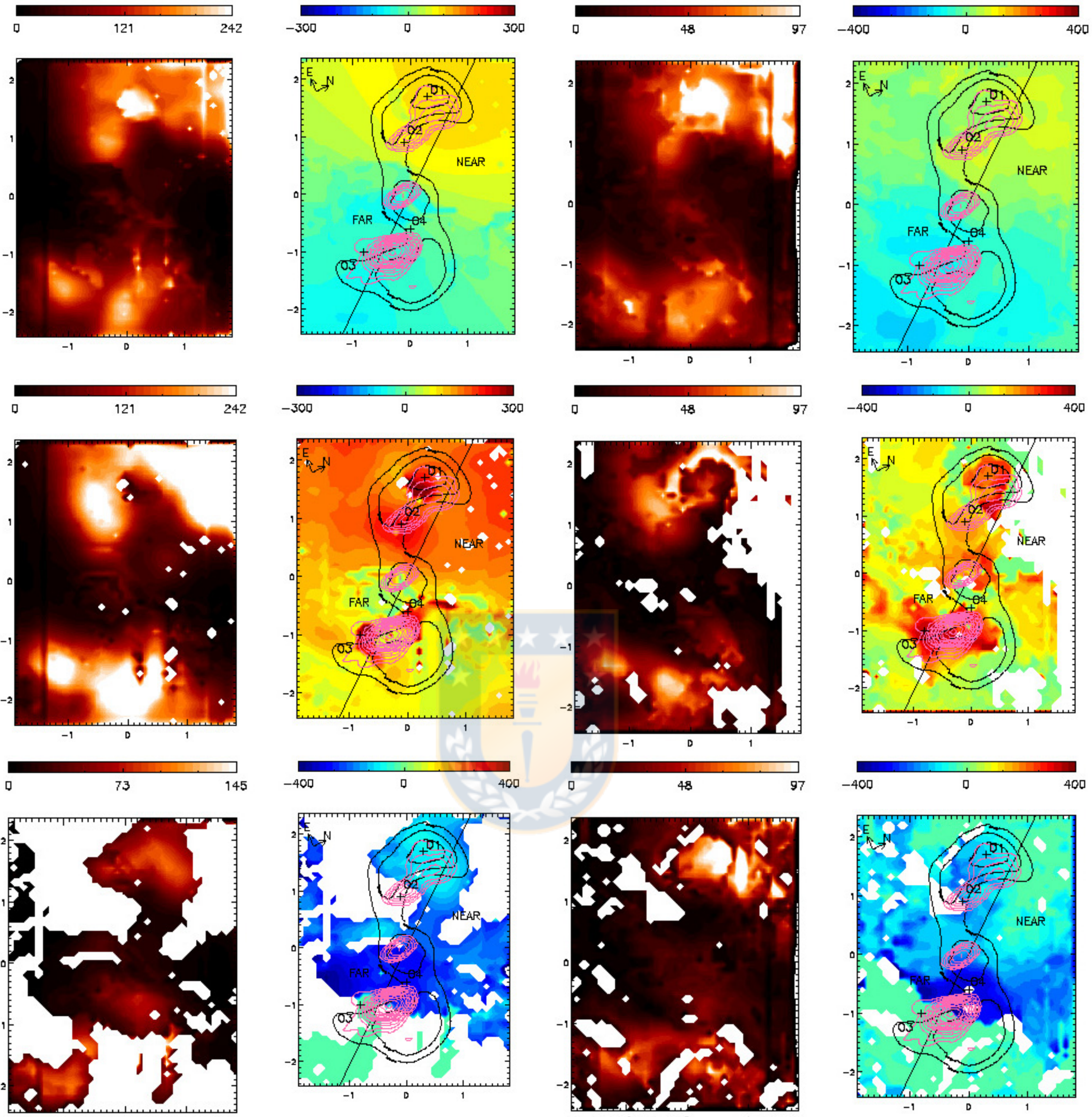

Figure 2.6: Moment 0 and 1 maps from our multiple-component Gaussian fit to the [OIII] and [NII] emission lines. First and second column show the moment 0 and moment 1 map for the [OIII] line. Third and fourth column show the moment 0 and 1 for the [NII] line. First, second and third row show the narrow, broad redshifted and broad blueshifted components respectively. Crosses marked as 'O1', 'O2', 'O3', and 'O4' show the central position of the outflows defined in the text. Black contours in the moment 1 maps show the moment 0 map of each emission line. Pink contours correspond to the VLA 8.4 GHz map. Source: Finlez et al. (2018).

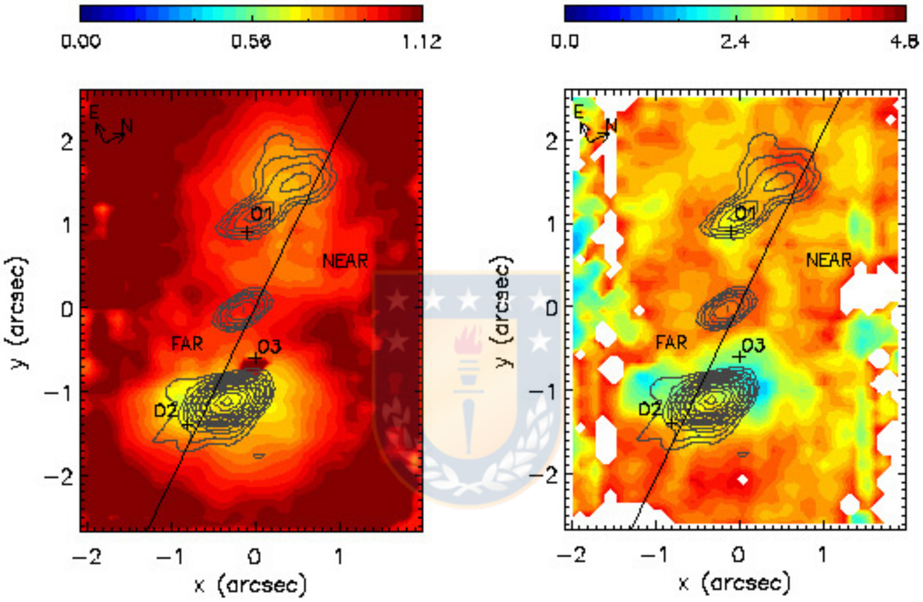

Figure 2.7: Left: $[SII]\lambda6716/\lambda6731$ line ratio from the one-component Gaussian fit to the [SII] doublet. Black contours correspond to the VLA 8.4 GHz map. Right: Hα/Hβ line ratio map from one-component Gaussian fit to these emission lines. Source: Finlez et al. (2018).

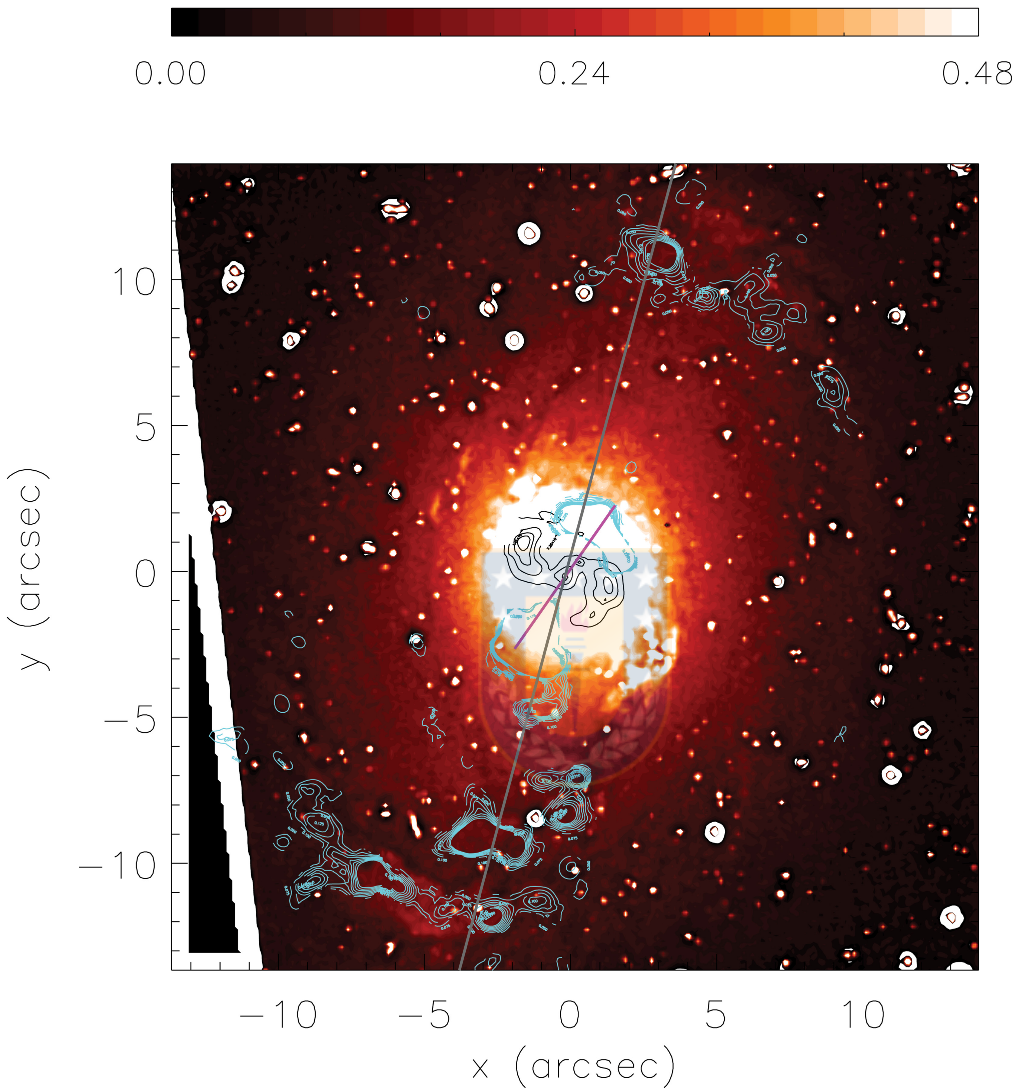

Figure 2.8: The structure map (obtained using a F606W HST image) of NGC 3393 is shown in color, with overlays of the ALMA CO J:2-1 moment 0 map (cyan contours) and the GMOS [NII] moment 0 map (black contours). The gray line marks the PA of the large-scale bar, and the magenta line corresponds to the PA and estimated extension of the nuclear bar. Source: Finlez et al. (2018).

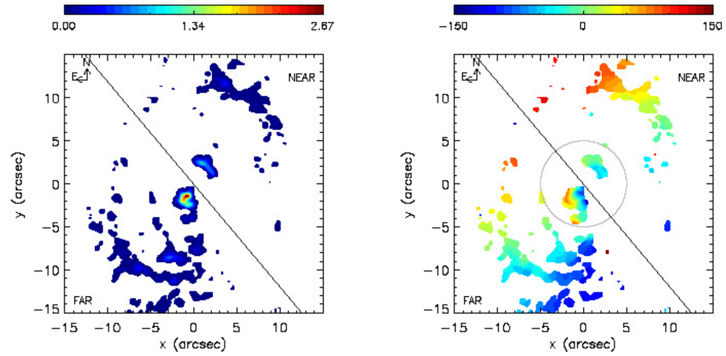

Figure 2.9: Moment maps for ALMA CO J:2-1 data. Top: integrated flux (moment 0) map following the color bar (units of Jy/beam km/s). Middle: velocity map (moment 1) after subtraction of a CO systemic velocity of 3746 km/s; the grey circle separates the inner region and outer region referred to in the text. Bottowm: velocity dispersion (moment 2) map. In all panels N is up and E is to the left, and the black line marks the adopted major axis PA of 40°. Source: Finlez et al. (2018).

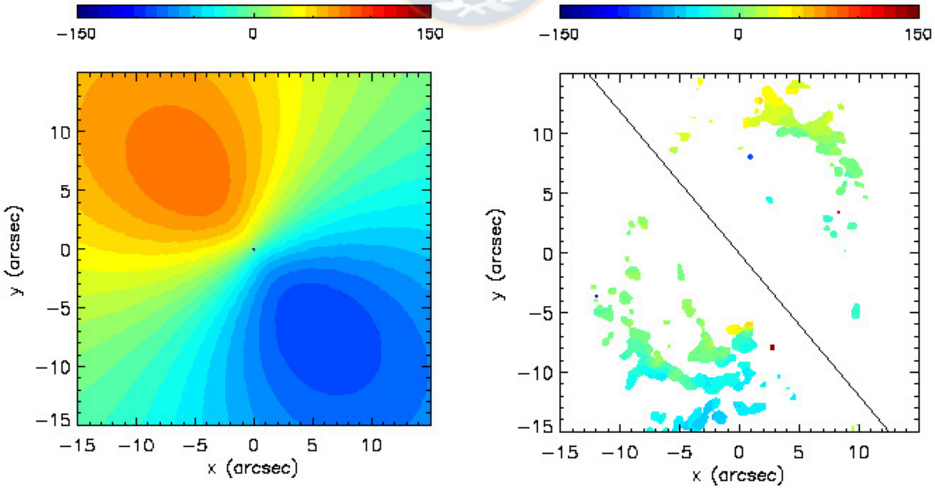

Figure 2.10: Left: Our pure rotation model derived from fitting the outer (outside the grey circle in Fig. 2.9) CO velocity field with a model based on an exponential disk potential (see text). Right: residual (observed - model) velocity field of the outer disk. Source: Finlez et al. (2018).

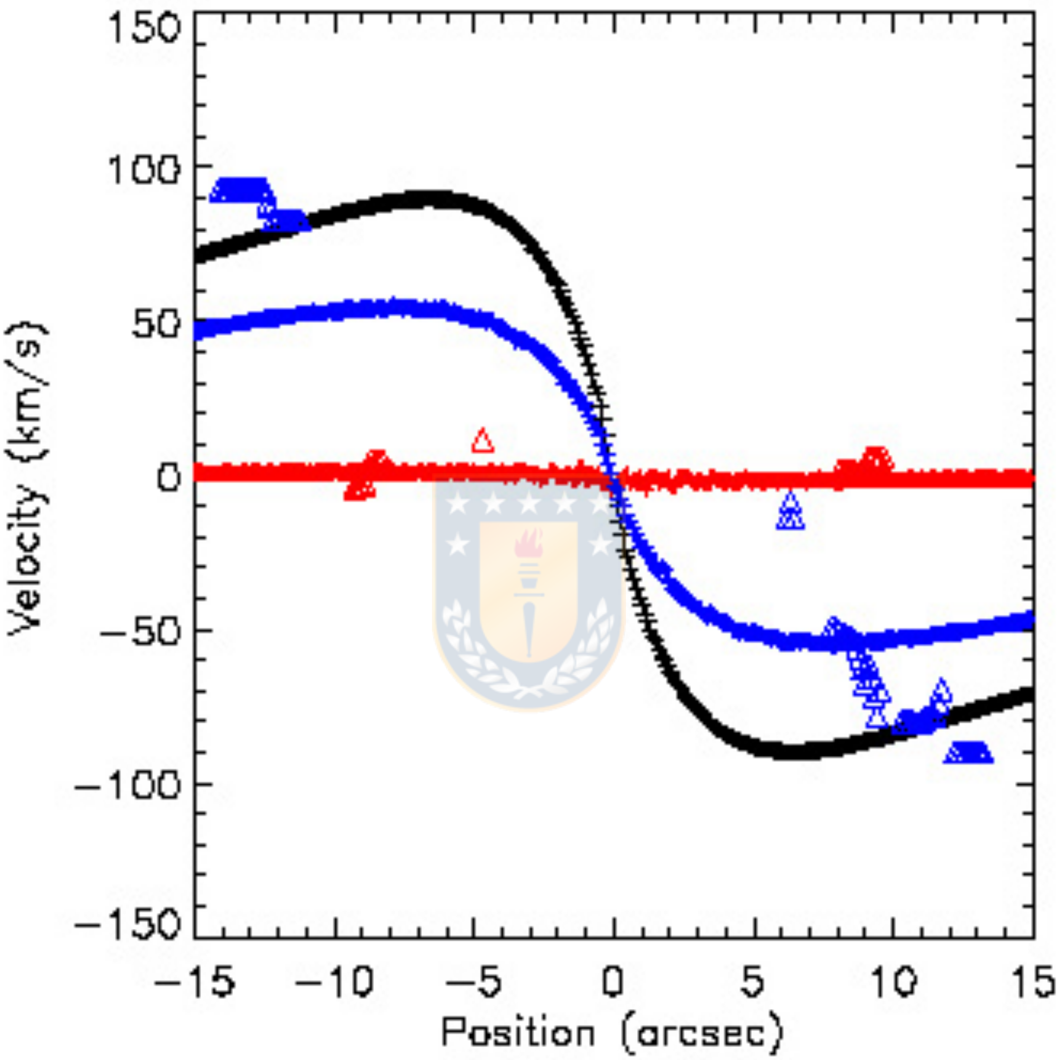

Figure 2.11: CO J:2-1 rotation curves in the outer (outside the grey circle in Fig. 2.9) region along the major axis (black triangles), minor axis (red triangles) and PA 10° (blue triangles). Plus symbols show the best-fitted pure rotation exponential disk model along the same PAs. Source: Finlez et al. (2018).

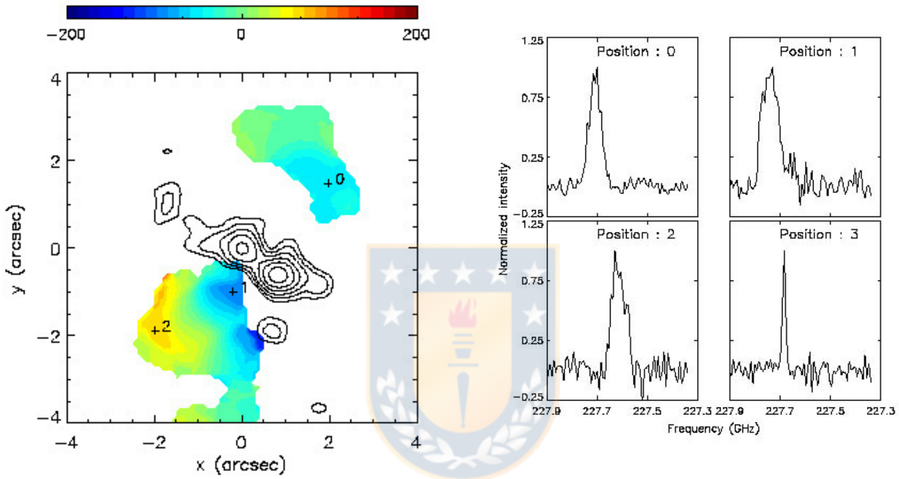

Figure 2.12: Top: observed CO J:2-1 velocity field of the inner region is shown in color following the color bar (units of km/s). Black contours show the ALMA continuum map. Bottom: example CO J:2-1 spectra of five distinct positions (0 to 2) in the inner SE feature as identified in the left panel, plus, for comparison, the spectrum of a sixth position (3) located outside the inner region. Source: Finlez et al. (2018).

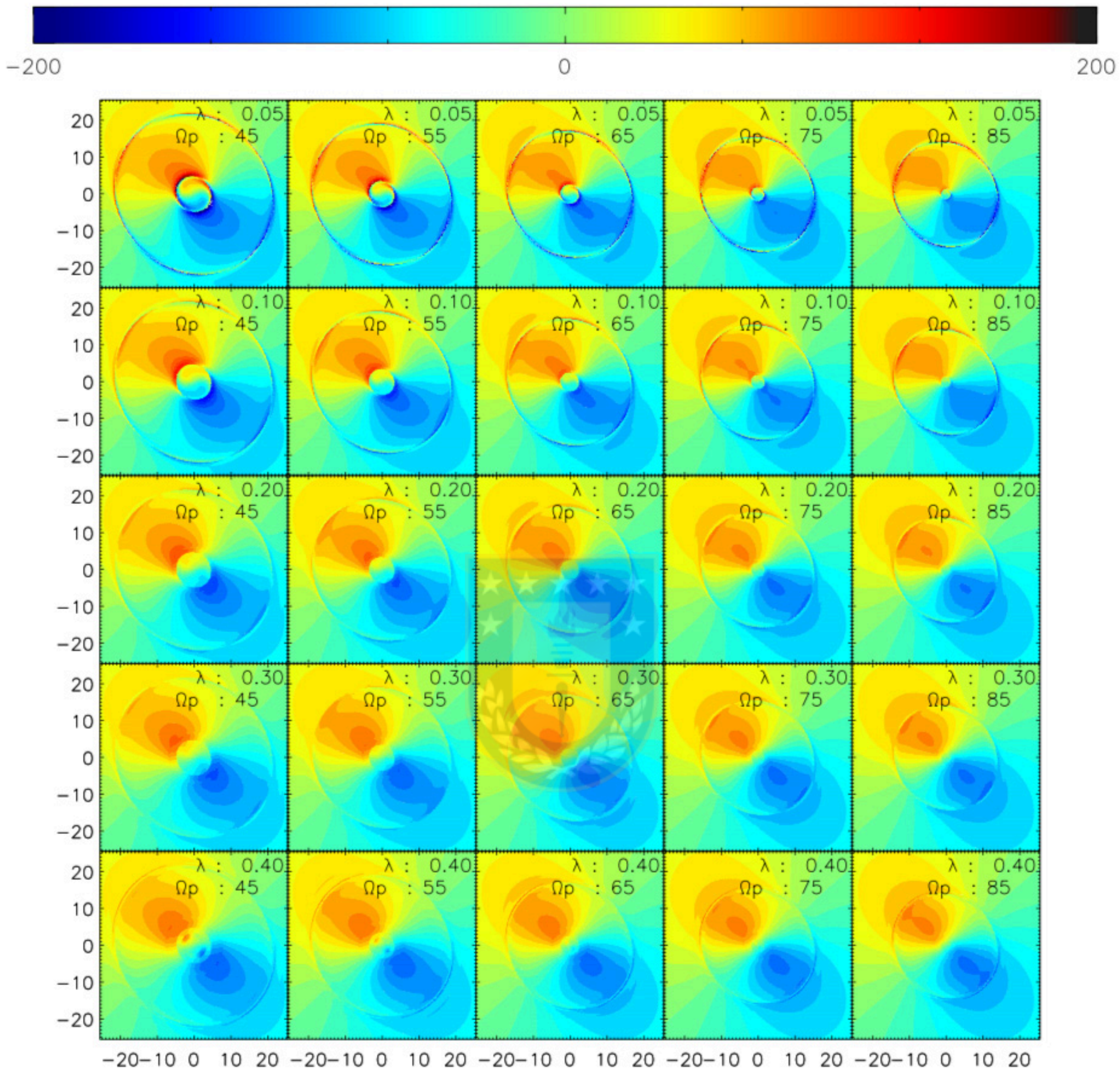

Figure 2.13: Velocity fields resulting from the bar perturbation model described in Sect. 2.4.3, when varying Ω_p (x-axis, values from 45 to 85 km/s/kpc, with a 10 km/s/kpc step), and λ (y-axis, values of 0.05, 0.1, 0.2, 0.3, and 0.4). All models use the intrinsic rotation curve derived from the best fit exponential disk model with parameters as explained in Sect. 2.3.3, and the bar parameters used were those of the large-scale bar: $PA_{bar} = 160°$ and $\epsilon = 0.15$. All panels follow the color bar shown at the top (units of km/s). Source: Finlez et al. (2018).

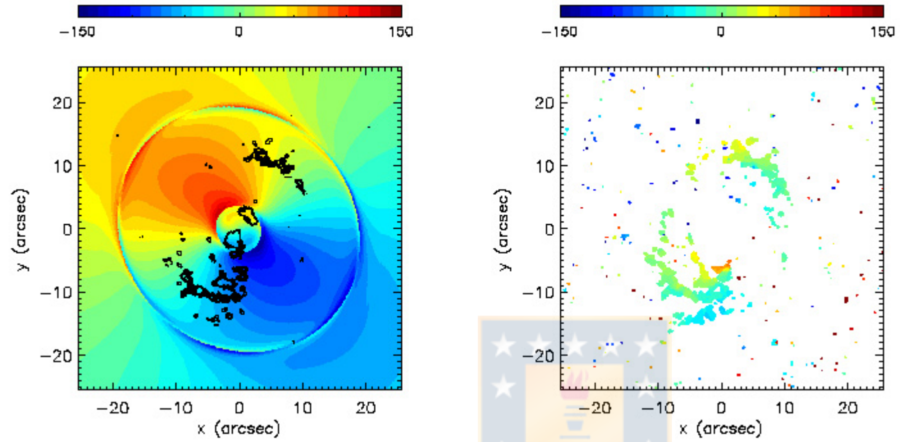

Figure 2.14: Left: velocity field of the best-fit bar perturbation model (see text) to the large scale ((outside the grey circle in Fig. 2.9)) CO velocity field following the color bar above the panel (units of km/s). The values of the exponential disk parameters, disk PA and inclination, were fixed to the values outlined in Fig. 2.10, and the bar PA ($PA_{bar} = 160°$) and ellipticity ($\epsilon = 0.15$) were set to the values of the large-scale bar. The best fit values for λ and Ω_p are 0.1 and 54 km/s/kpc, respectively. Overlaid black contours show the integrated intensity (moment 0) of CO J:2-1. Right: residual (observed - model) velocity map for the bar perturbation model following the color bar above the panel (units of km/s): only the large scale velocity residuals are shown. Source: Finlez et al. (2018).

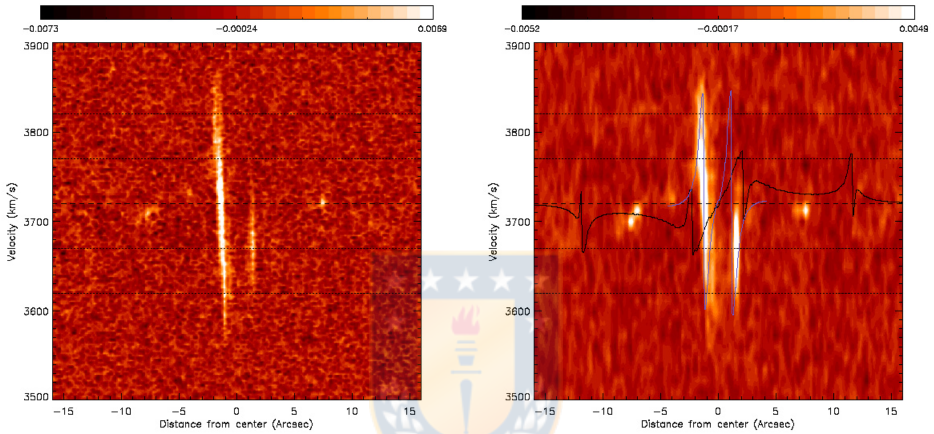

Figure 2.15: Top: pv-diagram centered on the SE component in the CO maps, extracted along a PA of −50°. Bottom: pv-diagram extracted from a natural weighted, 4 channel averaged cube with 10 km/s spectral resolution, with a slit centered on the galaxy nucleus and extracted along the minor axis. The black line shows the prediction of the large-scale bar perturbation model described in Sect. 2.4.4 (see Fig. 2.14) and the blue line shows the prediction of the nuclear bar model. Source: Finlez et al. (2018).

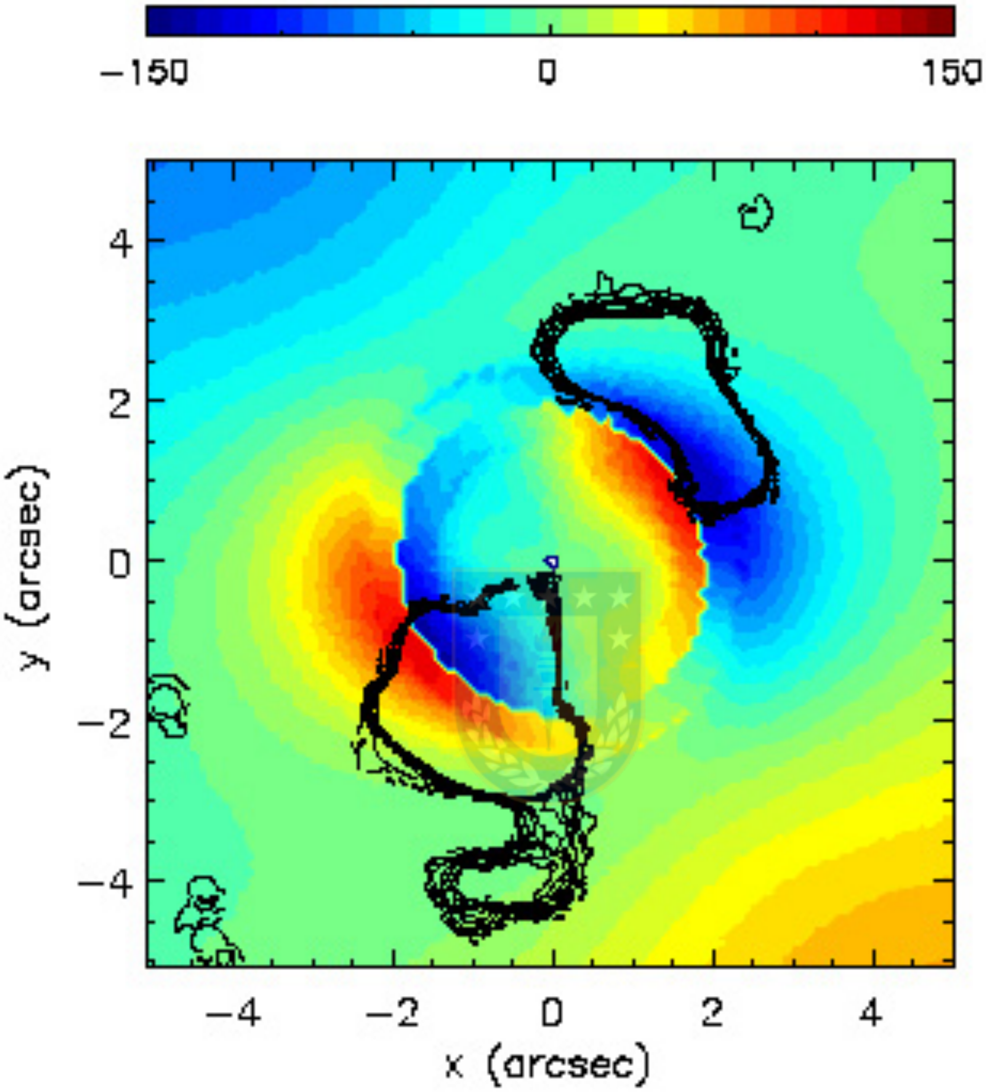

Figure 2.16: Velocity field of the best fit bar perturbation model for the nuclear bar shown in color following the color bar above the panel (units of km/s). Here the fit was made only to the inner region (inside the grey circle in Fig. 2.9) CO velocity field. The values of the exponential disk, disk PA and inclination, were fixed to the values outlined in Fig. 2.10. The best fit values obtained were $\theta_{obs} = -85°$, $\epsilon = 0.35$, $\lambda = 0.1$ and $\Omega_p = 73$ km/s/kpc. Source: Finlez et al. (2018).

Chapter 3

The kinematics of NGC 4945

3.1 Introduction

In this work we present an analysis of the kinematics of NGC 4945 using new data from ALMA (CO J:3-2 and HCO+ J:4-3). NGC 4945 is a nearby (3.82 ± 0.31 Mpc, Karachentsev et al. (2007)), edge-on, spiral (SB(s)cd or SAB(s)cd) galaxy (Webster et al. 1979) that extends over 17 arcmin diameter (in the optical, de Vaucouleurs (1964)).

This galaxy has been classified as a Seyfert 2 (Madejski et al. 2000), the presence of an AGN has been confirmed by X-ray (Iwasawa et al. 1993). NGC 4945 hosts a water maser (Greenhill et al. 1997), and a 100 pc -scale starburst ring, which has been observed in Paα with NICMOS on the HST (Marconi et al. 2000). This source is one of the brightest AGNs in the sky at 100 keV (Done et al. 1996). Hard X-ray observations of this source show that it is extremely variable and highly absorbed (Guainazzi et al. 2000; Madejski et al. 2000; Puccetti et al. 2014). NGC 4945 is a Compton-thick galaxy (Iwasawa et al. 1993), its nuclear region is highly obscured by gas and dust in the optical (Madejski et al. 2000), high density gas has been observed in this region (Cunningham & Whiteoak 2005, e.g.). The presence of a large scale bar that could extend up to 7 kpc is observed in neutral Hydrogen (Ott et al. 2001). Optical and IR observations show a wind-blown conical shaped cavity in the inner region (Moorwood et al. 1996).

Observations of the molecular gas of this source (e.g. Ott et al. 2001; Henkel et al. 2018) show an inclined disk with a major axis aligned with the large scale disk and the starburst ring. The galaxy distance allow for very high resolution observations (as $1'' \sim 19$ pc) and makes it an ideal source to study the kinematical signatures of feeding and feedback.

3.2 Observations

NGC 4945 was observed on July 06, 2017, with ALMA during Cycle 5 (project-ID 2016.1.01135.S; PI - Nagar). The observation was taken using the ALMA Band 7 receiver on fourty-four 12-meter antennas. Four spectral windows (SPWs), two in the lower sideband and two in the upper sideband were used. Three of these were configured to cover the following lines at relatively high resolution (~ 1.3 km s^{-1}): CO(3-2) (red; $\nu_{\rm obs} = 344.240826$ GHz) , CO(3-2) (blue; $\nu_{\rm obs} = 346.043722$ GHz) and HCO+(4-3) ($\nu_{\rm obs} = 356.095326$ GHz). The remaining SPW was set to lower spectral resolution in order to better detect the continuum emission.

The flux, bandpass and the phase calibrator used for the observation were J1307-5019, J1427-4206 and J1326-5256, respectively. The total observing time was ~ 37 min with about 19 min spent on the source. The data was calibrated using the standard pipeline offered by the ALMA and imaged using CASA 4.7.0 (McMullin et al. 2007). The continuum emission was subtracted using the task *uvcontsub* from all the SPWs before producing the final datacubes. The synthesized beam size is $0.''17 \times 0.''16$ along the position angle (PA) of 72°.

3.3 Results

3.3.1 Continuum emission

The 345 GHz continuum emission shows an elongated source with a clumpy distribution. We fitted a two-dimensional Gaussian profile to the continuum, the centre of the fit (marked as a blue triangle in Fig. 3.1) coincides with the position of the water maser found by Greenhill et al. (1997). The integrated flux of the fit is 380 mJy, while the flux peak is 25 mJy. The fit shows an elliptical shape with its major axis along PA 42°, the major axis extension is 1.3 arcsec and the minor axis 0.3 arcsec. This fit coincides well with the large disk PA 41° and the water maser PA 45 °.

3.3.2 Molecular gas distribution

We report ALMA observations of CO (J:3-2) and HCO+ (J:4-3). In Fig. 3.2 we show the integrated intensity (moment 0) maps at 3σ for both emission lines, the blue triangle marks the position of the water maser (Greenhill et al. 1997), we

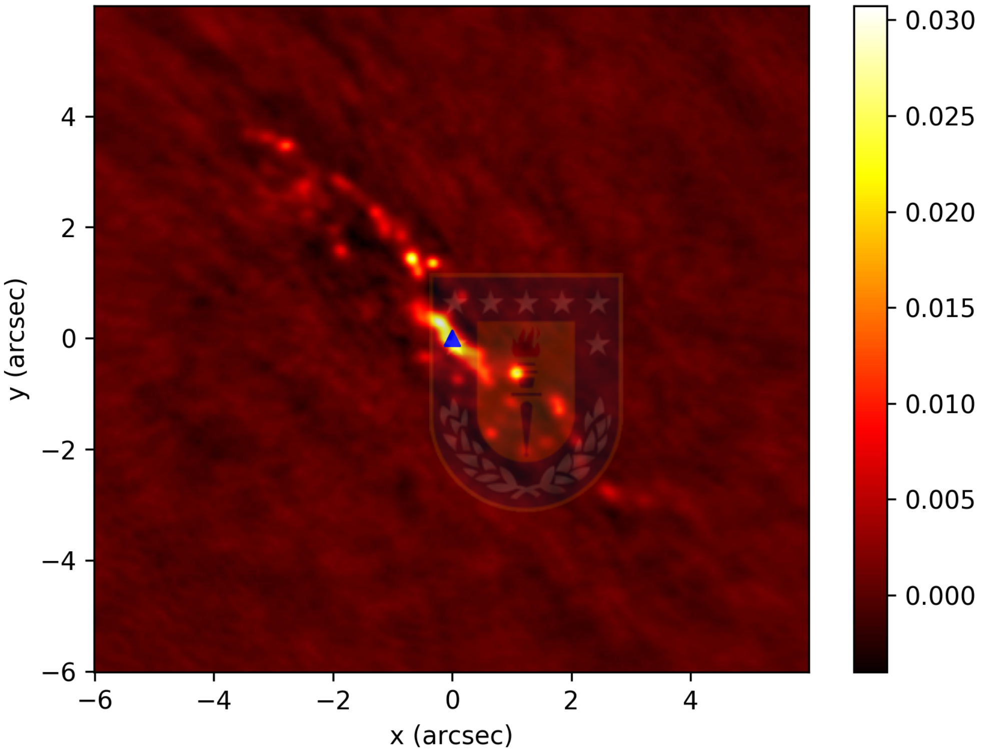

Figure 3.1: Image of the continuum emission from the central $\sim 12'' \times 12''$ (this corresponds to ~ 230 pc $\times 230$ pc). This map was created using the line-free frequencies of the 345 GHz window. Source: this work.

observe that both emission lines maps are off-centred, the centre HCO+(J:4-3) is more displaced NW than CO(J:3-2). The distribution of the molecular gas in HCO+ seems to be concentrated in a disk which projects as a highly eccentric ellipse due to the large inclination of the galaxy, and it is elongated along PA $\sim 42^\circ$ which is in agreement with the large scale galactic disk, water maser disk and the continuum image. This ellipse has a major axis of $\sim 5''.5$ and minor axis of $1''.4$, which corresponds to an unprojected disk of radius ~ 100 pc.

A flux profile along the major axis of the moment 0 for HCO+ (J:4-3) shows a depression in flux in the central region (Fig. 3.3), there is no presence of a hole in this line. For CO (J: 3-2) we can observe that the depression in flux is deeper and closer to zero, which indicates the possible presence of a hole in the centre of the moment 0 map for CO (J: 3-2). In Figures 3.4 and 3.5 we show the channel maps for both emission lines. We can observe clear signatures of absorption on some of the channels, near the centre.

3.3.3 The HCO (J:4-3) emission

The velocity (moment 1) map of the HCO J:4-3 (Fig. 3.6) shows that the dominant feature seems to be fairly ordered disk rotation, however the S-shaped zero velocity line indicates the presence of some non-circular components. Due to the clear presence of absorption observed in the channel maps we present the position-velocity (PV) diagram for this line for the major and minor axis in Fig. 3.7 and some example spectra along the major axis in Fig. 3.8.
In both the PV-diagrams and the spectra of the galaxies there are clear signatures of an absorption line, we fitted the cube with two Gaussian profile components, one absorption and one emission Gaussian (examples of this fit along the major axis can be observed in Fig. 3.9). We proceeded to subtract the absorption line to the data cube. In Fig. 3.10 we show a comparison of the PV-diagrams along the major axis for the normal data cube and the subtracted datacube. We can observe that the absorption line seems to follow a solid-body rotation (marked as solid black line), and the rotation curve keeps its overall shape when the absorption line is subtracted.

To obtain a model of the circular rotation of the galaxy, we fitted the rotation curve along the major axis using a spherical potential with pure circular rotation, the observed radial velocity from this potential as described in Bertola et al. (1991) is given by:

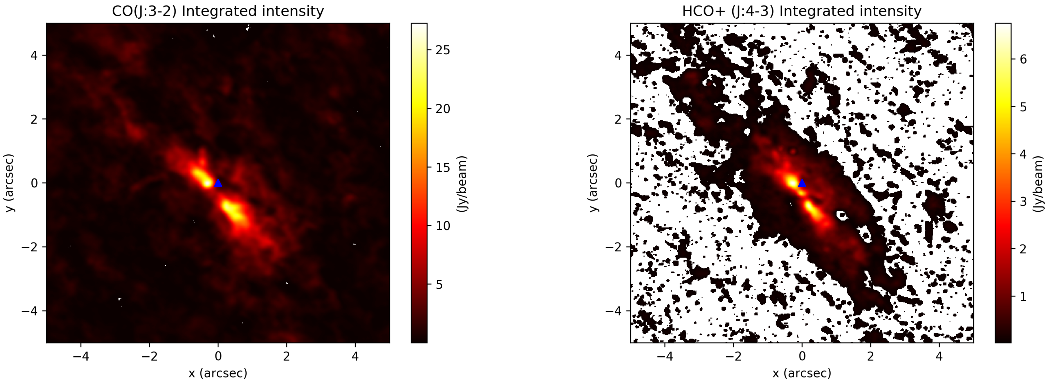

Figure 3.2: Integrated intensity (moment 0) maps for CO J:3-2 (left) and HCO+ J:4-3 (right). Blue triangle marks the position of the water maser (Greenhill et al. 1997). In all panels North is up. Source: this work.

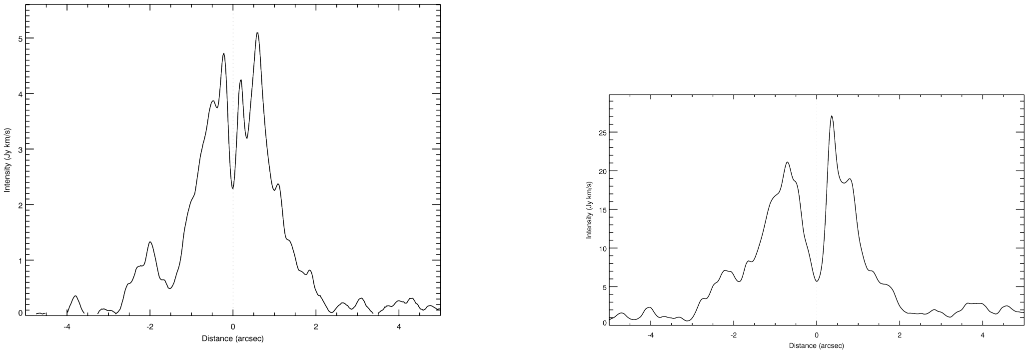

Figure 3.3: Flux profile taking along the major axis (PA 45°) from the moment 0 maps of HCO+ (J:4-3) and CO (J: 3-2), left and right maps respectively. Dashed grey line marks the position of the centre. Source: this work.

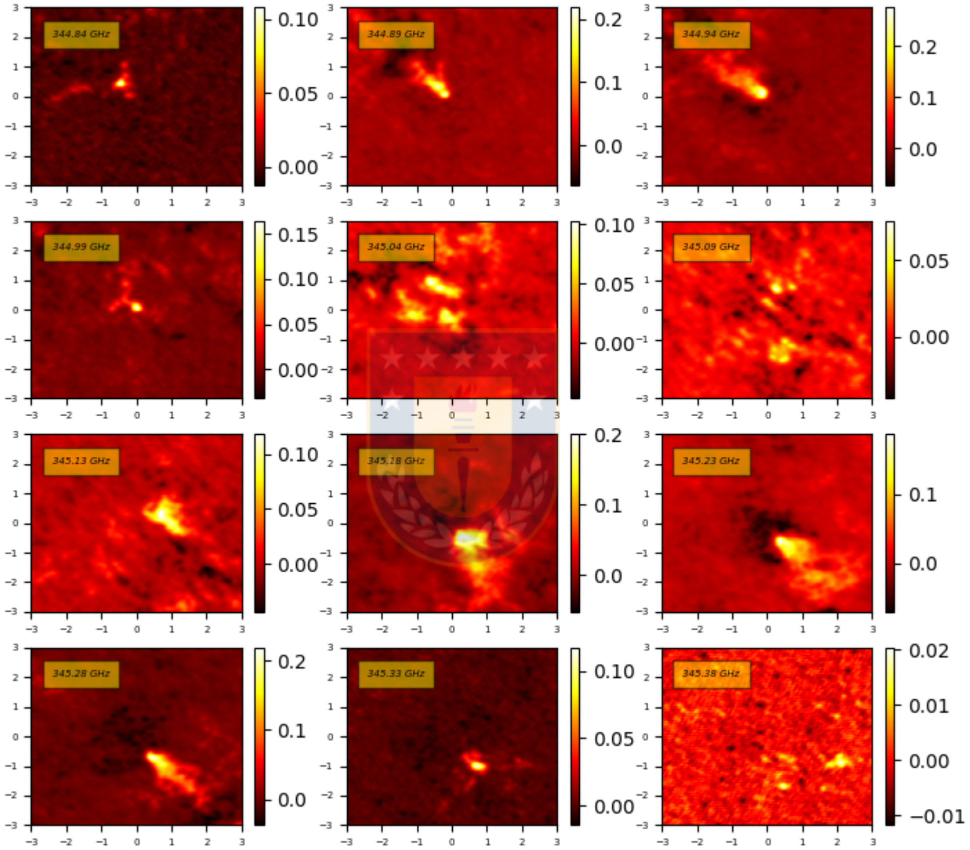

Figure 3.4: Channel maps for CO J:3-2. The frequency of every channel is indicated in the top left corner. Source: this work.

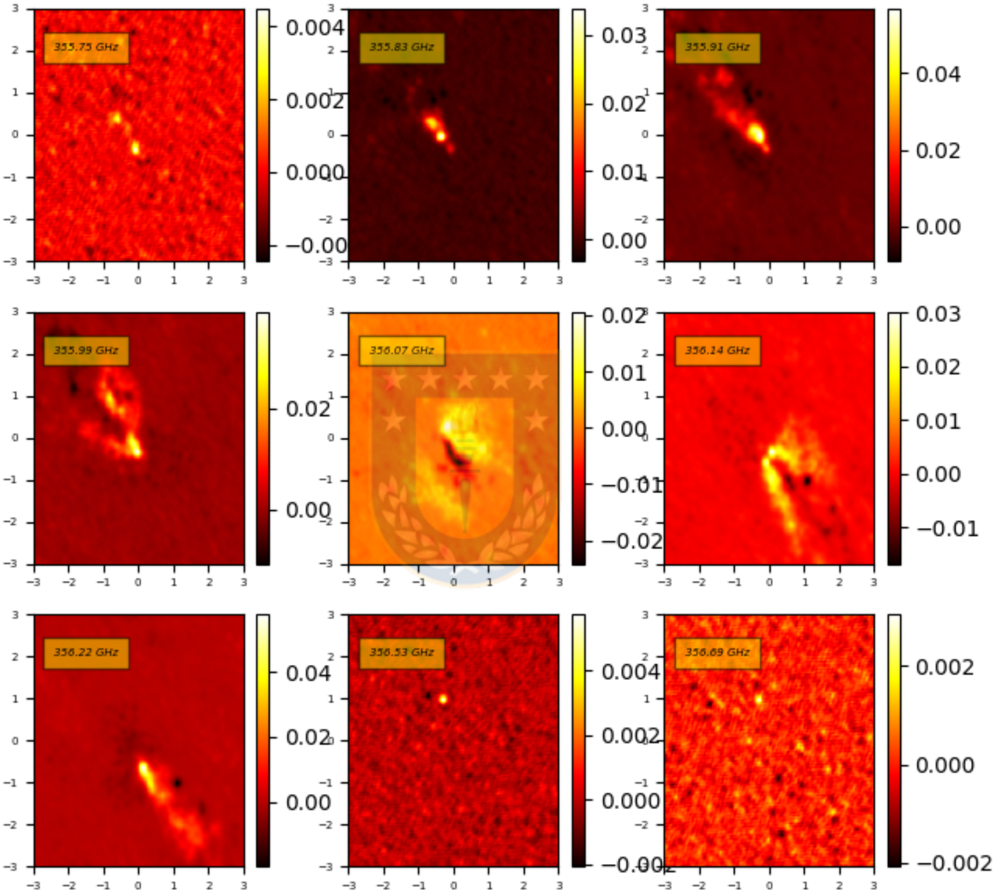

Figure 3.5: Channel maps for HCO+ J:4-3. The frequency of every channel is indicated in the top left corner. Source: this work.

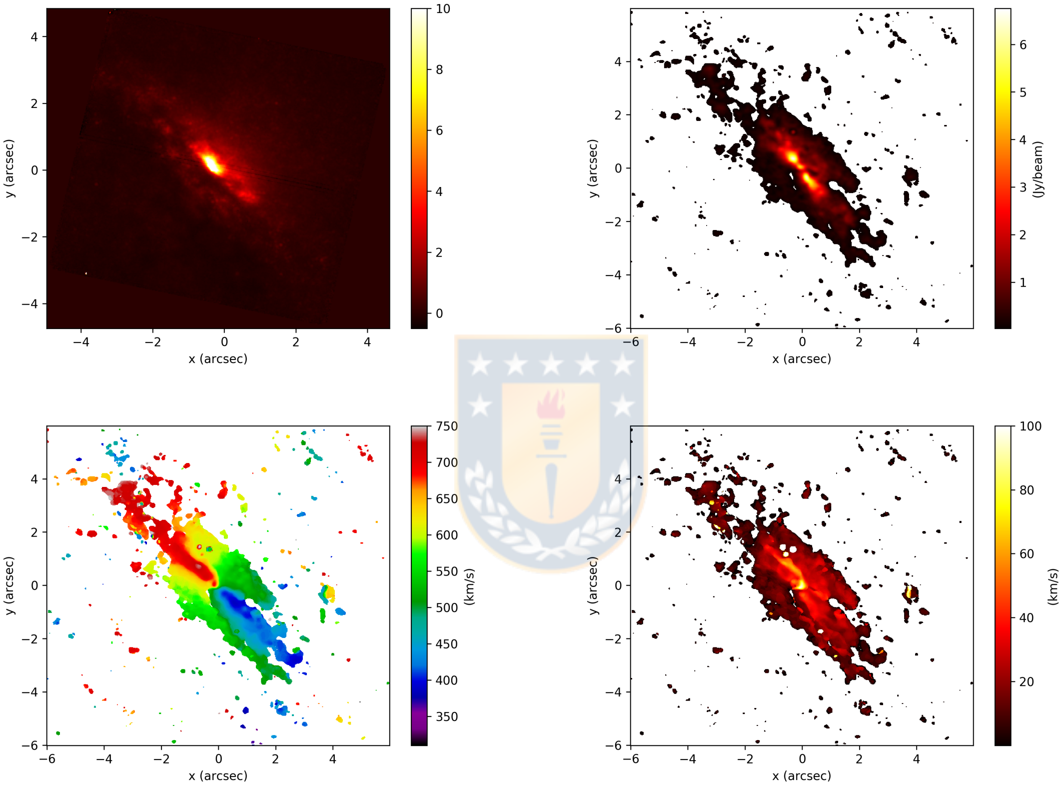

Figure 3.6: HST image and moment maps for the ALMA HCO+ (J:4-3) data. Top left: F212n HST image. Top right: integrated flux (moment 0) map. Bottom left: velocity map (moment 1). Bottom right: velocity dispersion (moment 2) map. In all panels North is up and East to the left. Source: this work.

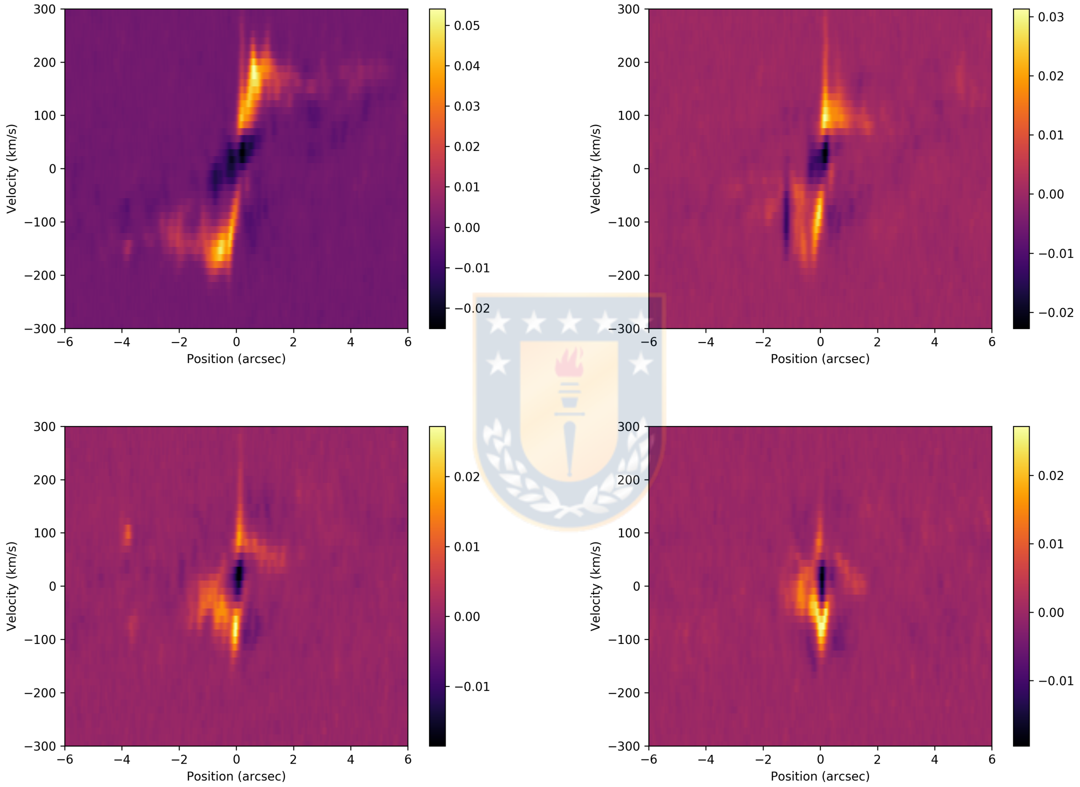

Figure 3.7: Position-velocity diagrams taken from a slit along PA 46° (top left), 66° (top right), 86° (bottom left) and PA 136° (bottom right). Source: this work.

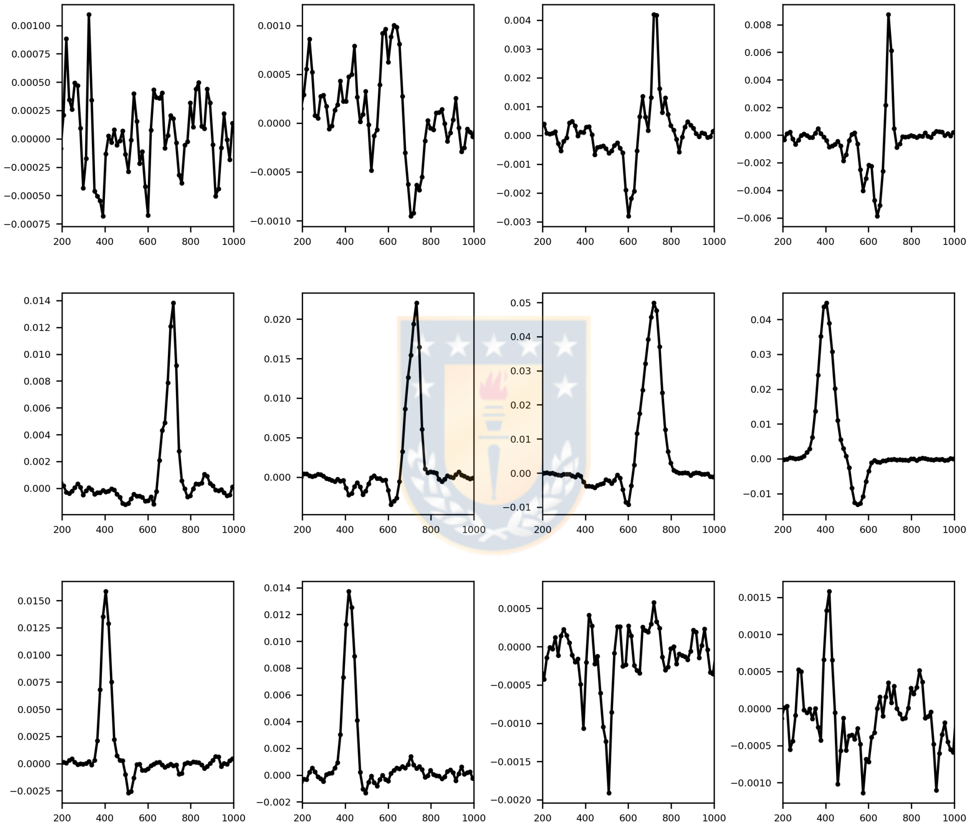

Figure 3.8: Example of spectra extracted from slit along PA 43°. X axis corresponds to velocity in km/s and Y axis to flux in Jy/beam. Source: this work.

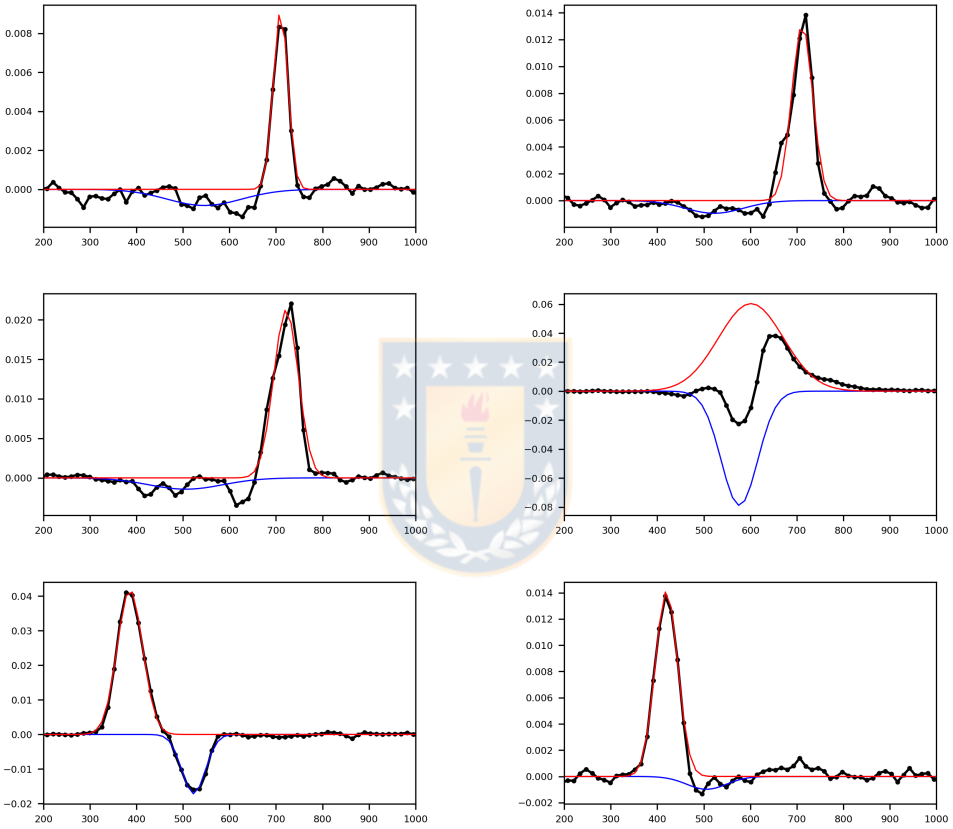

Figure 3.9: Example of spectra extracted along major axis, fitted with two Gaussian profiles. Absorption (emission) profile is marked in blue (red). X axis corresponds to velocity in km/s and Y axis to flux in Jy/beam. Source: this work.

$$V = V_{sys} + \frac{AR\cos(\psi-\psi_0)\cos^p(\theta)}{(R^2[\sin^2(\psi-\psi_0)+\cos^2(\psi-\psi_0)]+c^2\cos^2\theta)^{p/2}} \ ,$$

Where V_{sys} is the systemic velocity of the galaxy, R is the radius from the centre, $theta$ is the disk inclination, ψ_0 is the position angle at the line of nodes, A is the amplitude of the rotation curve, c the concentration parameter (regulates the compactness of the solid-body-like rotation) and p regulates the slope of the curve at larger radii. The fit was performed using least-square minimization along the major axis, keeping PA, inclination, centre position and V_{sys} as fixed parameters and varying A,c, and p. The best fitted values were $A = 182.39$, $c = 0.32$ and $p = 1.07$.

We show this model over-plotted to the moment 1 map and the residual map (subtraction of the model to the moment 1 map) in Fig. 3.11.

To compare the rotation model to the data cube we have used the KINematic Molecular Simulation (KinMS) routines of Davis et al. (2013), which creates a simulated cube that includes the effects of beam-smearing, disk-thickness, and velocity dispersion. In Fig. 3.12 we show PV-diagrams along major and minor axis of the data cube, with the KinMS simulated data cube from our model over-plotted in white, we can see some of the features and the width of the velocity dispersion is caused by beam-smearing and possibly due to the high inclination of the galaxy.

We can observe a Keplerian fall in the PV-diagrams extracted along different PAs, thus we added the effect of a SMBH to the model, starting with a mass of 1.4×10^6 $M_\odot$ as suggested by Greenhill et al. (1997), however this mass does not reproduce the observed fall and thus we fitted different values, a possible range of BH mass is $4-6\times10^7$ $M_\odot$. PV-diagrams along different PAs with the fitted Bertola model plus the Keplerian disk of a 5×10^7 $M_\odot$ mass over-plotted can be observed in Fig. 3.13.

Molecular outflow

The residuals map in Fig. 3.11 show excess blueshifted emission in the near side of the galaxy and excess redshifted emission on the far side along PA $\sim 26°$, which can be an indication of an outflow in the disk. Along PAs $\sim 15-36°$ (example in Fig. 3.13) the possible outflow can be seen as a feature that does not follow the rotation model.

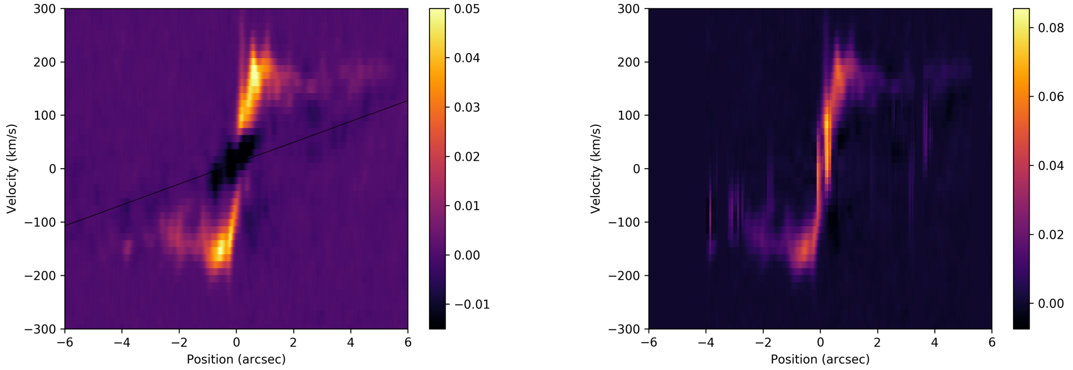

Figure 3.10: Left: PV-diagram for data cube along major axis (PA 46°), solid-body rotation model marked as solid back line. Right: PV-diagram along major axis for absorption line subtracted cube. Source: this work.

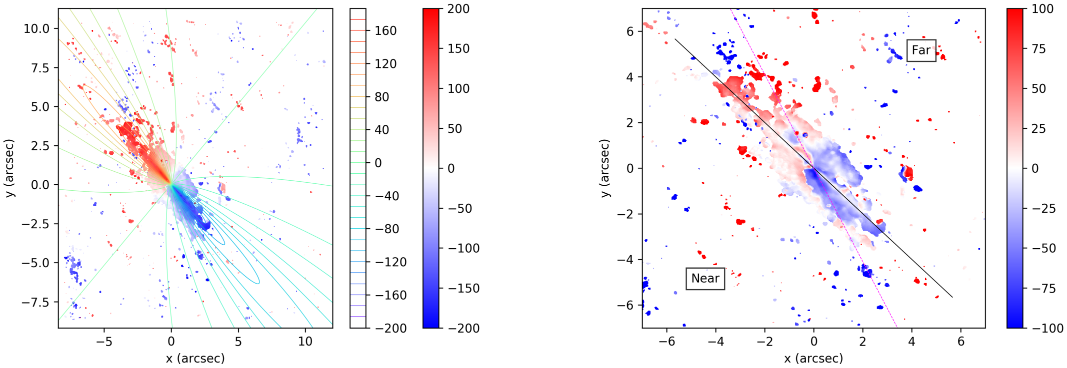

Figure 3.11: Left: moment 1 map in red-blue color scale, over-plotted is the fitted Bertola model to the disk rotation in color contours. Right: residuals map (Bertola model subtracted to moment 1 map), solid black line shows major axis PA 46°, dashed magenta line shows PA of excess emission, and text labels mark near and far sides of the galaxy. Source: this work.

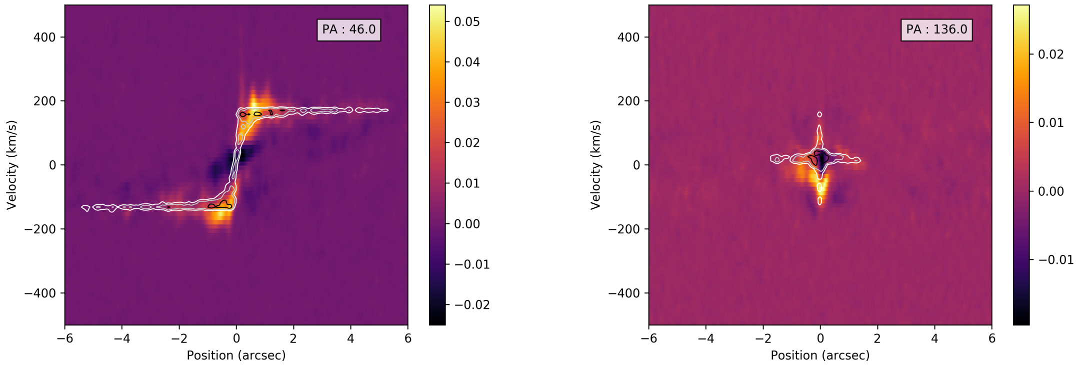

Figure 3.12: PV-diagram along major (left) and minor (right) axis. Over-plotted in white contours PV-diagram from KinMS simulated cube from best fitted Bertola model. Source: this work.

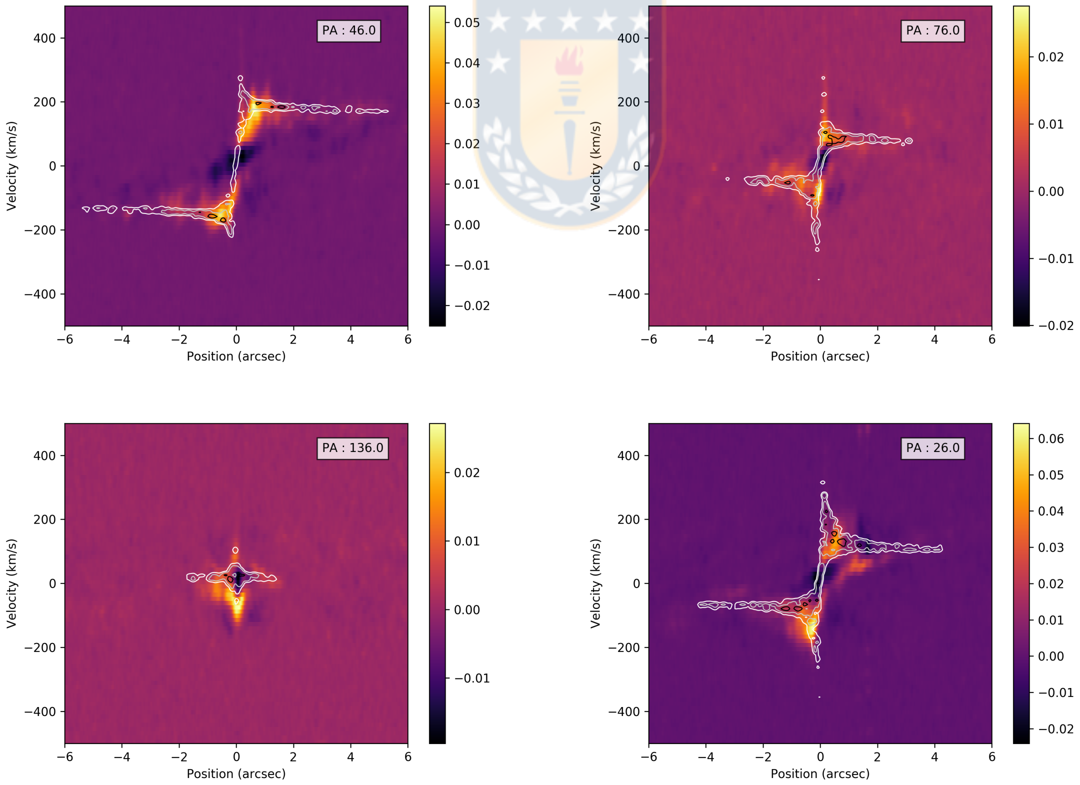

Figure 3.13: PV-diagram along different PAs (labelled on top right corner). Over-plotted in white contours PV-diagram from KinMS simulated cube from best fitted Bertola model and a Keplerian fall from a SMBH of 5×10^7 $M_\odot$. Source: this work.

In Fig. 3.14 we show apertures of $0\farcs2$ in radius following the posited outflow (marked in red and blue circles) and perpendicular to this where we also see some excess in redshifted emission (near side) and blueshifted emission (far side), this and the clear presence of an S-shaped zero velocity line are both indicators that other non-circular motions might be present on this galaxy. The spectra extracted from these apertures is shown in Fig. 3.15, where the grey line marks the systemic velocity ($V_{sys} = 563$ km/s) and the magenta line marks the expected velocity at the centre of the aperture from the fitted Bertola model. The blue apertures (indexes 1-4) show a wide emission line with multiple kinematic components, the emission is mostly blueshifted from systemic and from the expected model value and the difference with the model velocity increases with aperture number, and thus going further away from the nucleus. In the case of the red apertures (indexes 5-6) the emission has clear multiple components, with the main component being more redshifted than the systemic velocity and the expected model value, an absorption line seems to follow the rotation from the Bertola model and there seems to be a second absorption line that follows the systemic velocity. The green apertures (indexes 9-12) show emission lines with profiles less wide than both red and blue apertures. In apertures 9 and 10 we can again observe the absorption line that seems to follow the rotation of the Bertola model, the emission line in these apertures seem to be overall less complex than the red and blue spectra, although some indications of multiple components can still be observed. Where the absorption line is not very prominent (apertures 11 and 12) we can see the spectra follows more or less the rotation from the Bertola model.

The spectra of these apertures indicate the presence of an outflow. The blueshifted and redshifted components have a velocity of $\sim \pm 130$ km/s, and a component reaches up to ~ 170 km/s in aperture 7. The outflow seems to be slowing down as apertures 4 and 8 show an outflow velocity of $\sim \pm 50$ km/s.

Bar perturbations

The existence of non-circular motions besides the outflow described in the previous section is suggested by the presence of an s-shaped zero-velocity line and by the residuals shown in Fig. 3.11 along PA 80°, where we see redshifted (blueshifted) emission on the near (far) side, these residuals can be connected to the same s-shaped zero-velocity line which can be caused by the presence of a bar.
The presence of a bar was suggested by Ott et al. (2001) based on HI and CO (J:2-1) observations which showed non-circular motions and a s-shaped zero-velocity

line, the posited bar extends to ±150″ along a PA $\sim 40°$ connecting the inner spiral arms. Lin et al. (2011) conducted numerical simulations of the central region of NGC 4945, and found that a small, weak and fast rotating bar in the central region can excite spiral density waves which can explain the iso-velocity contours observed in the kinematics of the CO (J:2-1) emission line. Higher resolution of the molecular gas carried by Henkel et al. (2018) suggests the presence of a nuclear bar with a PA $\sim 90°$ and it connects to the nuclear spiral arms. They propose the presence of inflowing gas between $\sim 100 - 300$ pc along the bar.

To test this hypothesis we apply the bar perturbation model as described in Finlez et al. (2018), based on the harmonic decomposition formalism (Wong et al. 2004), where the line-of-sight velocity can be decomposed in a Fourier series as:

$$V_{LOS}(R) = c_0 + \sum_{j=1}^{n} [c_j \cos(j\psi) + s_j \sin(j\psi)] \sin i \ ,$$

where (R, ψ) are polar coordinates, i is the inclination of the disk, c_0 corresponds to the systemic velocity (V_{sys}), and j is the harmonic number. The coefficients c_j and s_j are a function of the circular velocity (V_c), the bar pattern speed (Ω_p), ellipticity of the potential (ϵ) and the bar viewing angle (θ_{obs}), which corresponds to the bar PA from the minor axis of the galaxy disk (see e.g. Fig. 2 of Wong et al. 2004, for a definition of this angle). A bar creates a bisymmetric gravitational potential which has a predominant $m = 2$ Fourier component, and thus we only consider the harmonics $j = m-1$ and $j = m+1$ (Schoenmakers et al. 1997a).

For the circular velocity (V_c) we use our fitted Bertola model for the rotation of the disk and for the bar we assume the PA given by Henkel et al. (2018), because if a nuclear bar is present at this scale it would dominate the kinematics. We use a usual value of $\lambda = 0.1$ for the damping parameter. With this we construct a library of models varying the parameters Ω_p and ϵ, a few examples of these models can be found in Fig. 3.16.

The pattern velocity of the bar (Ω_p) defines the resonances radii, and the ellipticity parameter influences the iso-velocity contours. Ott et al. (2001) suggests a bar velocity of 11 km/s/kpc while Lin et al. (2011) suggest a fast bar with a velocity of 233 km/s/kpc. Giving the uncertainty in the bar velocity, ellipticity and position angle of the bar a fit becomes difficult to achieve because of the amount of free parameters. We observed that the models that give the residuals with lower rms have low ellipticity ($0.9 < \epsilon < 0.25$). The residual maps are not largely affected by the rotation velocity of the bar as the velocities in the central region of the model and where the molecular gas is present remains similar, however a good indicator are the velocity twists generated by the resonances, smaller velocities create resonances at larger radii. Velocities ≤ 40 km/s/kpc define a resonance that is close to the molecular gas disk observed, velocities of ~ 200 km/s/kpc create a resonance on the edge of the observed disk.

We chose a model ($\Omega_p = 100$ km/s/kpc and *epsilon* = 0.1, Fig.3.17) to show the s-shaped zero-velocity line and the residuals of this model show a decrease in the redshifted and blueshifted excess along PA $\sim 80°$ observed in Fig. 3.11, which indicates it is possible this feature is caused by the bar, although some excess low-velocity blueshifted emission remains in the far side indicating a possible inflow of gas along the bar.

Further detailed modelling of the bar perturbations is needed to better clarify the role of the bar in the inner kinematics but our results agree with the scenario put forward by Henkel et al. (2018) and Lin et al. (2011) of a fast nuclear bar in the central region that is causing a low-velocity inflow of gas along the bar, and this bar is the cause of the s-shaped iso-velocity contours and some of the observed non-circular motions in the nuclear region.

3.3.4 The CO (J=3-2) emission

In Fig. 3.18 we present the moment maps for the CO (J:3-2) emission line. While the integrated flux (moment 0) map is rather similar than the HCO+ (J:4-3) moment 0 map, we found a larger depression of flux at the centre, as can be observed in the flux profile in Fig. 3.3. The velocity (moment 1) map seems more disturbed than the HCO+ equivalent. The velocity dispersion (moment 2) map shows a larger dispersion in the centre and in the NW region where the outflow is observed in HCO+ (J:4-3).

The PV-diagrams (Fig. 3.19) show an overall similar rotation curve than the observed in HCO+, however in CO (J:3-2) the gas seems to have suffered more self-absorption and the kinematics are more perturbed. The absorption line follows, more or less, the same solid-body-like rotation as observed in HCO+.

We fitted the rotation following the same procedure as described for the HCO+ (J:4-3) line. The fitted Bertola model was subtracted to the moment 1 map (Fig.

3.20), we can see that the residuals in CO (J:3-2) are more complex than those observed for HCO+ (J:4-3), however, some of the residuals are similar, we found redshifted (blueshifted) excess emission is found in the far (near) side in the same areas as observed for HCO+ (J:4-3).

Overall the results from HCO+ (J:4-3) seem to be consistent with the CO (J:3-2) observations, however the significant amount of absorption in this line makes a detailed analysis of the kinematics less reliable as this absorption can affect the velocity field and the fits to the models.

3.4 Conclusions

We have presented high resolution CO (J:3-2) and HCO+ (J:4-3) ALMA observations for the starburst Seyfert 2 galaxy NGC 4945. We presented results of the analysis of the kinematics of the dense molecular gas in the central region of this galaxy. From this analysis we conclude the following:

- The dense molecular gas is concentrated in an inclined disk of ~ 100 pc, which extends along PA $\sim 42^\circ$, aligned with the large scale disk and the starburst ring.
- Both CO (J:3-2) and HCO+ (J:4-3) emission lines are off-centred from the peak of the continuum emission and the megamaser position. With the peak of the HCO+ (J:4-3) emission being more displaced than CO (J:3-2).
- Both molecular lines are affected by absorption, with CO (J:3-2) being significantly more affected, thus we choose to carry the majority of the analysis on the less affected by absorption HCO+ (J:4-3) emission line.
- The overall kinematics of the HCO+ (J:4-3) show that the disk mostly follows the rotation of the large-scale disk. We fitted this rotation with a Bertola model.
- To explain the features observed in the PV-diagrams we added the effect of a SMBH to the rotation curve, which indicates the presence of a black hole with mass 5×10^7 M$_\odot$, a mass considerable larger than the suggested mass of 1.4×10^6 M$_\odot$ (Greenhill et al. 1997).
- We suggest the presence of an outflow in the disk along PA $\sim 26^\circ$ with velocities of ~ 150 km/s, based on the presence of features that do not follow

rotation in the PV-diagrams between PAs $\sim 15° - 36°$, the excess of blueshifted (redshifted) emission in the near (far) side of the galaxy in the residual map, and the spectra extracted from apertures along the regions where that excess emission was found.

- We test the hypothesis of a small and fast nuclear bar along PA 90°, and found that is likely such a bar can reproduce the features observed in the kinematics of the molecular disk, particularly the s-shaped iso-velocity contours, and it is possible this bar is leading a small inflow of $\sim$ 30 km/s to the nuclear region. Further modelling for the bar kinematics is necessary to completely disentangle the bar-provoked perturbations in the inner region of this galaxy.

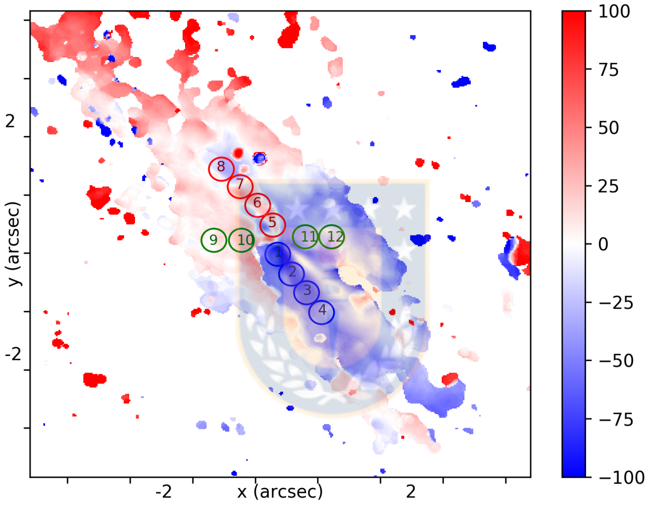

Figure 3.14: Residuals from Bertola model as in Fig. 3.11. Overplotted in blue and red circles are the $r = 0\farcs2$ apertures along the outflow and perpendicular to the outflow in green. Numbers indicate the index of every aperture. Source: this work.

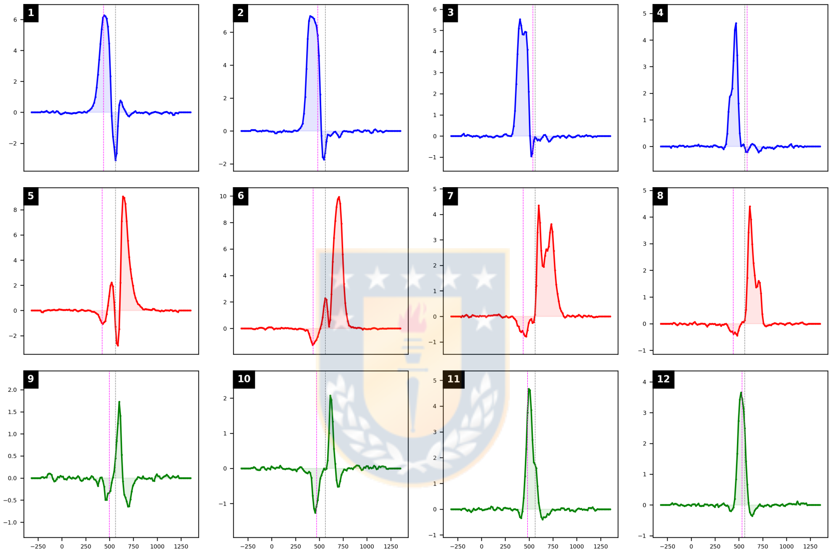

Figure 3.15: Spectra extracted from the apertures described and numbered in Fig. 3.14. Color of spectra coincides with color of apertures in Fig. 3.14. Grey dashed line marks the systemic velocity while the magenta dashed line shows the velocity expected at the centre of the aperture according to the fitted Bertola model. Source: this work.

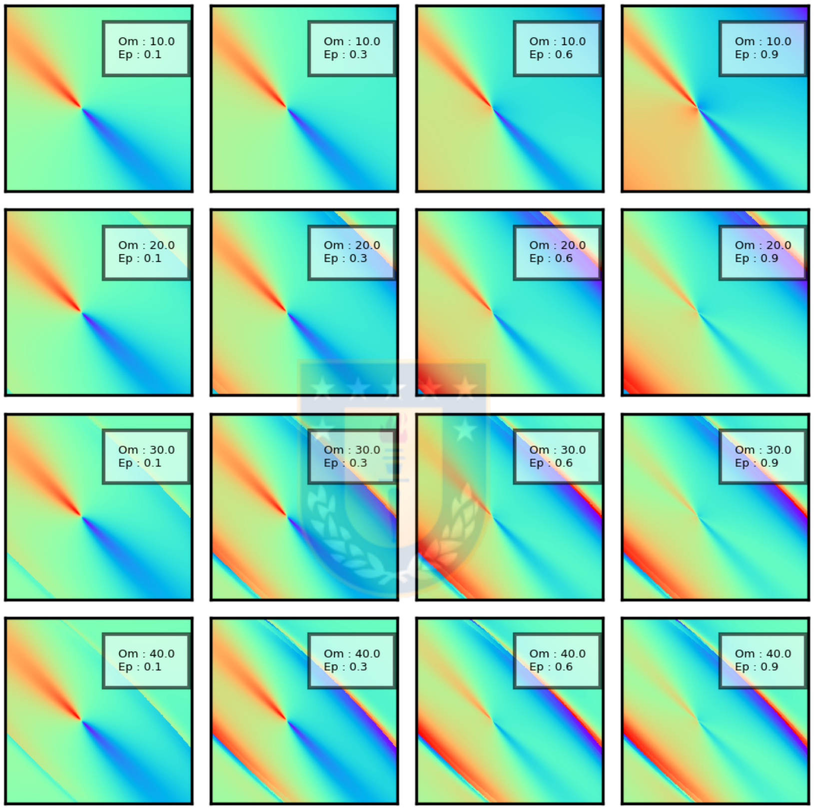

Figure 3.16: Example of multiple models of the bar perturbation model, changing in bar rotation velocity (Ω_p) in the x axis of the grid and ellipticity (ϵ) in the y axis. The base model is the fitted Bertola model, and we assume a bar orientation of PA 90° and a viscosity parameter (λ) of 0.1. Source: this work.

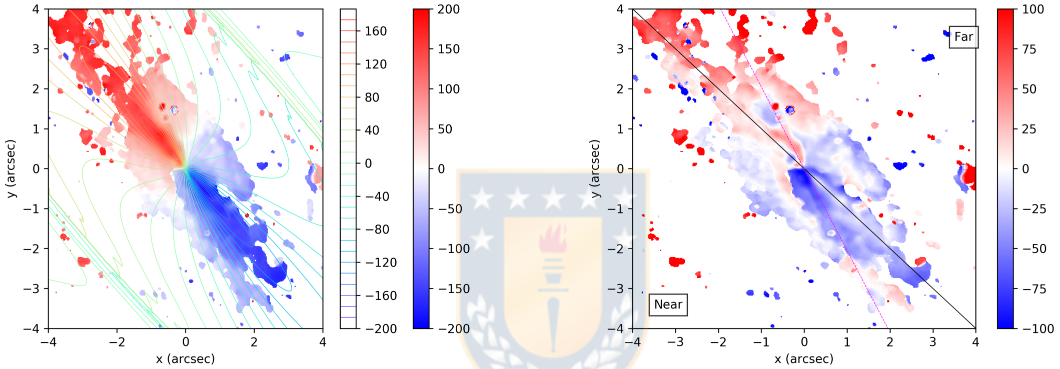

Figure 3.17: Example of bar perturbation model with parameters $\Omega_p = 100$ km/s/kpc, $\lambda = 0.1$, $\theta_{obs} = 134°$, and $\epsilon = 0.1$. Left: bar perturbation model overplotted on the moment 1 map. Right: residuals map (bar perturbation model subtracted to moment 1 map), solid black line shows major axis PA 46°, dashed magenta line shows PA of excess emission, and text labels mark near and far sides of the galaxy. Source: this work.

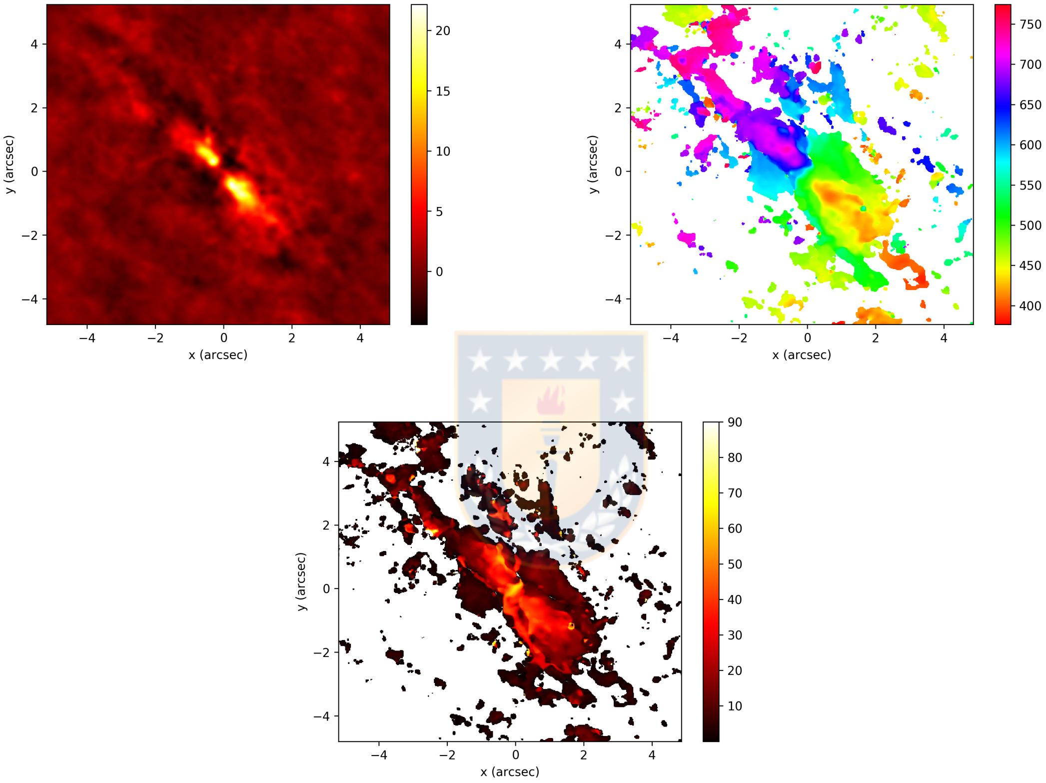

Figure 3.18: Moment maps for the ALMA HCO (J:3-2) data. Top left: integrated flux (moment 0) map. Top right: velocity map (moment 1). Bottom: velocity dispersion (moment 2) map. In all panels North is up and East to the left. Source: this work.

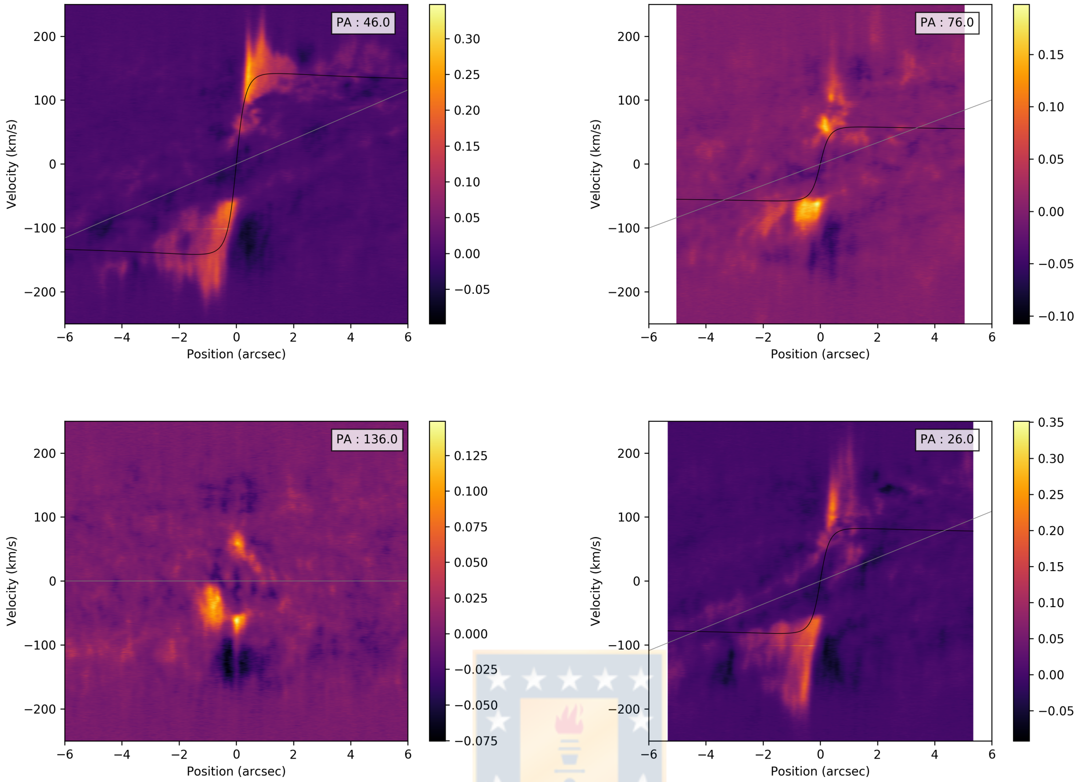

Figure 3.19: PV-diagram for data cube along PAs 46°, 76°, 136°, 26° (labeled in the top right corner). Solid-body rotation model marked as solid grey line, and fitted Bertola model marked as solid black line. Source: this work.

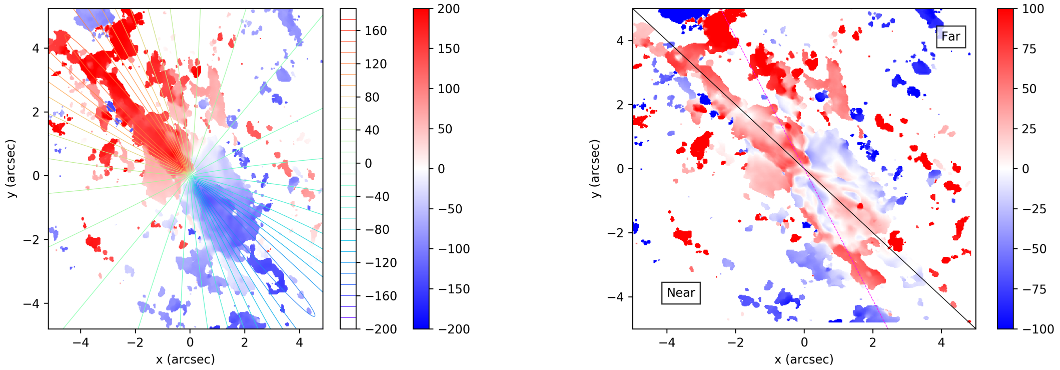

Figure 3.20: Left: moment 1 map in red-blue color scale for the CO (J:3-2) line, over-plotted is the fitted Bertola model to the disk rotation in color contours. Right: residuals map (Bertola model subtracted to moment 1 map), solid black line shows major axis PA 46°, dashed magenta line shows PA of excess emission found in HCO+ (J:4-3), and text labels mark near and far sides of the galaxy. Source: this work.

Chapter 4

Conclusions and future work

4.1 Summary and conclusions

In this thesis I have presented high resolution ALMA and IFS observations for two nearby active galaxies. The final product of these observations are 'data cubes', which have two spatial dimensions and one spectral dimension. This translates into obtaining an spectra for every spaxel of the image, a powerful tool that allows us to obtain detailed kinematics in every pixel of the observation. The observations were carried at high (sub-arcsecond) resolution.

The purpose of these observations is to study at great detail the kinematical signatures of the feeding and feedback processes in the inner kpc of nearby active galaxies.

Our observations of the inner few hundred parsecs of nearby active galaxies reveal the complexity of the kinematics in this region, as we can observe the kinematical signatures of different processes occurring simultaneously. We have observed the presence of different types of outflows, jet-induced outflows, equatorial outflows and nuclear outflows. It has been proposed that a variety of mechanisms acting on a variety of scales are needed to reproduced the needed feedback to successfully model structure formation and galaxy evolution. We have found signatures of ongoing modest feedback in the inner region of these galaxies.

During this thesis, particular attention was paid to the role played by bars in the kinematics of the inner region. A model of bar perturbations was developed and applied not only to the galaxies in this sample but also to some of the galaxies being analysed by our collaboration group (Slater et al. 2019; Vergara et al. 2019; Muñoz-Vergara et al. 2019), to which I contributed performing the bar perturbation analysis for these sources. We found that the presence of a stellar bar induces perturbations in the inner ∼ kpc of the galaxy, which is usually observed as an s-shaped zero-velocity contour. The pattern speed of the bar plays an important role in defining the radii of different resonances, which translate into different radial regime were orbit families have the same orientation, when these orbit families change orientation at the resonance, shocks are produced and the gas following these orbits loose angular momentum, allowing it to fall into the central region. When present, the ILR can define one of the most relevant resonances, as gas can get stalled in a ring around this resonance (commonly at ∼ 100 pc). The presence of a nuclear bar can help the gas get pass this ring and continue its journey to the centre. We found possible signatures of this process in the two galaxies analysed here, as both of them have been suggested to have a nuclear bar. In NGC 4945 the presence of a starburst ring indicates the possible location of the ILR and the kinematics inside this ring are consistent with the presence of a nuclear bar that can be driving an inflow to the SMBH. For NGC 3393 we found that a likely explanation of the kinematics observed in the molecular gas comes from the coupling between the large scale and the nuclear bar, even though we did not found direct detections of inflowing gas in this galaxy it is possible an inflow along the nuclear bar can exist and it is under our detection limit.

The work reported on this thesis presents a picture of the complexity of the inner region of active galaxies, where inflows, outflows, jet-induced shocks and bar perturbations co-exist and are often found to occur simultaneously and show a multi-phase behaviour with signatures of different kinematical components observed both on the ionised and molecular gas. The complexity of this interplay of components can only be unraveled by high-resolution observations.

4.2 Future work

Further work involving the modelling of the bar induced-kinematics is necessary to extend our knowledge of the mechanism that allows the bar to bring gas to the central region and be able to more accurately and confidently disentangle the bar contribution to the inner kinematics from the rest of the kinematical components observed. This modelling should be carried from high-resolution numerical simulations of the gas dynamics due to the bar potential.

Another aspect of future research is the development of tools that are able to deal with large datasets and can manage to model the datacube as a whole instead of collapsing it on one dimension (as it is the usual method of obtaining moment maps), this would prevent the loss of important information on each spaxel, taking full advantage of the three dimensional nature of datasets obtained from IFS and interferometry.

Following these detailed studies of nearby galaxies the next step moving forward to obtain a complete picture of the feeding and feedback processes and their contribution to the galaxy evolution is to obtain a complete, consistent and statistically significant sample of observations in which to search for correlations between the observed feeding and feedback signatures and the host galaxies properties.

References

Alatalo, K., Blitz, L., Young, L. M., et al. 2011, ApJ, 735, 88

Allington-Smith, J., Murray, G., Content, R., et al. 2002, PASP, 114, 892

Alonso-Herrero, A., Simpson, C., Ward, M. J., & Wilson, A. S. 1998, ApJ, 495, 196

Antonuccio-Delogu, V., & Silk, J. 2010, MNRAS, 405, 1303

Athanassoula, E. 1992, MNRAS, 259, 345

Baldry, I. K., Glazebrook, K., Brinkmann, J., et al. 2004, ApJ, 600, 681

Balogh, M. L., Baldry, I. K., Nichol, R., et al. 2004, ApJ, 615, L101

Barbosa, F. K. B., Storchi-Bergmann, T., Cid Fernandes, R., Winge, C., & Schmitt, H. 2009, MNRAS, 396, 2

Beckmann, V., & Shrader, C. 2012, in Proceedings of "An INTEGRAL view of the high-energy sky (the first 10 years)" - 9th INTEGRAL Workshop and celebration of the 10th anniversary of the launch (INTEGRAL 2012). 15-19 October 2012. Bibliotheque Nationale de France, 69

Bergmann, T. S. 2012, in Astronomical Society of the Pacific Conference Series, Vol. 460, AGN Winds in Charleston, ed. G. Chartas, F. Hamann, & K. M. Leighly, 133

Bertola, F., Bettoni, D., Danziger, J., et al. 1991, ApJ, 373, 369

Best, P. N., Carilli, C. L., Garrington, S. T., Longair, M. S., & Rottgering, H. J. A. 1998, MNRAS, 299, 357

Best, P. N., Kauffmann, G., Heckman, T. M., & Ivezić, Ž. 2005, MNRAS, 362, 9

Bianchi, S., Guainazzi, M., & Chiaberge, M. 2006, A&A, 448, 499

Cappellari, M. 2017, MNRAS, 466, 798

Cappellari, M., & Copin, Y. 2003, MNRAS, 342, 345

Cappellari, M., & Emsellem, E. 2004, PASP, 116, 138

Cavagnolo, K. W., McNamara, B. R., Nulsen, P. E. J., et al. 2010, ApJ, 720, 1066

Cheung, E., Trump, J. R., Athanassoula, E., et al. 2015, MNRAS, 447, 506

Cicone, C., Maiolino, R., Sturm, E., et al. 2014, A&A, 562, A21

Cisternas, M., Gadotti, D. A., Knapen, J. H., et al. 2013, ApJ, 776, 50

Combes, F. 2001, in Advanced Lectures on the Starburst-AGN, ed. I. Aretxaga, D. Kunth, & R. Mujica, 223

Combes, F., & Gerin, M. 1985a, A&A, 150, 327

—. 1985b, A&A, 150, 327

Cooke, A. J., Baldwin, J. A., Ferland, G. J., Netzer, H., & Wilson, A. S. 2000, ApJS, 129, 517

Couto, G. S., Storchi-Bergmann, T., & Schnorr-Müller, A. 2017, MNRAS, 469, 1573

Croton, D. J., Springel, V., White, S. D. M., et al. 2006, MNRAS, 365, 11

Cunningham, M. R., & Whiteoak, J. B. 2005, MNRAS, 364, 37

Das, V., Crenshaw, D. M., & Kraemer, S. B. 2007, ApJ, 656, 699

Dasyra, K. M., & Combes, F. 2012, A&A, 541, L7

Davies, R. I., Maciejewski, W., Hicks, E. K. S., et al. 2014, ApJ, 792, 101

Davis, T. A., Bureau, M., Cappellari, M., Sarzi, M., & Blitz, L. 2013, Nature, 494, 328

de Vaucouleurs, G. 1961, ApJS, 5, 233

—. 1964, ApJ, 139, 899

de Vaucouleurs, G., de Vaucouleurs, A., Corwin, Jr., H. G., et al. 1991, Third Reference Catalogue of Bright Galaxies. Volume I: Explanations and references. Volume II: Data for galaxies between 0^h and 12^h. Volume III: Data for galaxies between 12^h and 24^h.

Di Matteo, T., Springel, V., & Hernquist, L. 2005, Nature, 433, 604

Disney, M. J., Boyce, P. J., Blades, J. C., et al. 1995, Nature, 376, 150

Done, C., Madejski, G. M., & Smith, D. A. 1996, ApJ, 463, L63

Dumas, G., Mundell, C. G., Emsellem, E., & Nagar, N. M. 2007, MNRAS, 379, 1249

Elitzur, M. 2012, ApJ, 747, L33

Emsellem, E., Greusard, D., Combes, F., et al. 2001a, A&A, 368, 52

Emsellem, E., Greusard, D., Friedli, D., & Combes, F. 2001b, in Astronomical Society of the Pacific Conference Series, Vol. 230, Galaxy Disks and Disk Galaxies, ed. J. G. Funes & E. M. Corsini, 235–236

Eskridge, P. B., Frogel, J. A., Pogge, R. W., et al. 2000, AJ, 119, 536

Fabbiano, G., Wang, J., Elvis, M., & Risaliti, G. 2011, Nature, 477, 431

Faber, S. M. 1973, ApJ, 179, 731

Faber, S. M., Worthey, G., & Gonzales, J. J. 1992, in IAU Symposium, Vol. 149, The Stellar Populations of Galaxies, ed. B. Barbuy & A. Renzini, 255

Fabian, A. C. 2012, ARA&A, 50, 455

Fan, L., Han, Y., Fang, G., et al. 2016, ApJ, 822, L32

Fath, E. A. 1909, Lick Observatory Bulletin, 149, 71

Ferrarese, L., & Ford, H. 2005a, Space Sci. Rev., 116, 523

—. 2005b, Space Sci. Rev., 116, 523

Ferrarese, L., & Merritt, D. 2000, ApJ, 539, L9

Feruglio, C., Maiolino, R., Piconcelli, E., et al. 2010, A&A, 518, L155

Finlez, C., Nagar, N. M., Storchi-Bergmann, T., et al. 2018, MNRAS, 479, 3892

Fischer, T. C., Crenshaw, D. M., Kraemer, S. B., & Schmitt, H. R. 2013, ApJS, 209, 1

Franx, M., van Gorkom, J. H., & de Zeeuw, T. 1994, ApJ, 436, 642

Galloway, M. A., Willett, K. W., Fortson, L. F., et al. 2015, MNRAS, 448, 3442

García-Burillo, S., Combes, F., Schinnerer, E., Boone, F., & Hunt, L. K. 2005, A&A, 441, 1011

García-Burillo, S., Combes, F., Usero, A., et al. 2014, A&A, 567, A125

Gebhardt, K., Bender, R., Bower, G., et al. 2000, ApJ, 539, L13

Genzel, R., Eisenhauer, F., & Gillessen, S. 2010, Reviews of Modern Physics, 82, 3121

Ghez, A. M., Salim, S., Weinberg, N. N., et al. 2008, ApJ, 689, 1044

Goulding, A. D., Greene, J. E., Bezanson, R., et al. 2017a, ArXiv e-prints, arXiv:1706.07436

Goulding, A. D., Matthaey, E., Greene, J. E., et al. 2017b, ApJ, 843, 135

Granato, G. L., Silva, L., Monaco, P., et al. 2001, MNRAS, 324, 757

Greenhill, L. J., Moran, J. M., & Herrnstein, J. R. 1997, ApJ, 481, L23

Guainazzi, M., Matt, G., Brandt, W. N., et al. 2000, A&A, 356, 463

Hardcastle, M. J., Ching, J. H. Y., Virdee, J. S., et al. 2013, MNRAS, 429, 2407

Henkel, C., Mühle, S., Bendo, G., et al. 2018, A&A, 615, A155

Ho, L. C., Filippenko, A. V., & Sargent, W. L. W. 1997a, ApJS, 112, 315

—. 1997b, ApJ, 487, 591

Holt, J., Tadhunter, C. N., Morganti, R., & Emonts, B. H. C. 2011, MNRAS, 410, 1527

Hönig, S. F., Kishimoto, M., Tristram, K. R. W., et al. 2013, ApJ, 771, 87

Hook, I. M., Jørgensen, I., Allington-Smith, J. R., et al. 2004, PASP, 116, 425

Hopkins, P. F., Hernquist, L., Cox, T. J., et al. 2006, ApJS, 163, 1

Hopkins, P. F., Kocevski, D. D., & Bundy, K. 2014, MNRAS, 445, 823

Hoyle, F., & Fowler, W. A. 1963, Nature, 197, 533

Hunt, L. K., & Malkan, M. A. 1999, ApJ, 516, 660

Iwasawa, K., Koyama, K., Awaki, H., et al. 1993, ApJ, 409, 155

Jarvis, M. J., Rawlings, S., Lacy, M., et al. 2001, MNRAS, 326, 1563

Jogee, S., Baker, A. J., Sakamoto, K., Scoville, N. Z., & Kenney, J. D. P. 2001, in Astronomical Society of the Pacific Conference Series, Vol. 249, The Central Kiloparsec of Starbursts and AGN: The La Palma Connection, ed. J. H. Knapen, J. E. Beckman, I. Shlosman, & T. J. Mahoney, 612

Jungwiert, B., Combes, F., & Axon, D. J. 1997, A&AS, 125, astro-ph/9705175

Karachentsev, I. D., Tully, R. B., Dolphin, A., et al. 2007, AJ, 133, 504

Kay, L. E., Tran, H. D., & Magalhães, A. M. 2002, in Bulletin of the American Astronomical Society, Vol. 34, American Astronomical Society Meeting Abstracts #200, 646

Kenney, J. D. P., Wilson, C. D., Scoville, N. Z., Devereux, N. A., & Young, J. S. 1992, ApJ, 395, L79

Kewley, L. J., Groves, B., Kauffmann, G., & Heckman, T. 2006, MNRAS, 372, 961

Kim, W.-T., Seo, W.-Y., Stone, J. M., Yoon, D., & Teuben, P. J. 2012, ApJ, 747, 60

Kirhakos, S., Bahcall, J. N., Schneider, D. P., & Kristian, J. 1999, ApJ, 520, 67

Knapen, J. H., Shlosman, I., & Peletier, R. F. 2000, ApJ, 529, 93

Kondratko, P. T., Greenhill, L. J., & Moran, J. M. 2008, ApJ, 678, 87

Kormendy, J., & Gebhardt, K. 2001, in American Institute of Physics Conference Series, Vol. 586, 20th Texas Symposium on relativistic astrophysics, ed. J. C. Wheeler & H. Martel, 363–381

Kormendy, J., & Ho, L. C. 2013a, Annual Review of Astronomy and Astrophysics, 51, 511

—. 2013b, ARA&A, 51, 511

Kormendy, J., & Richstone, D. 1995, ARA&A, 33, 581

Koss, M. J., Romero-Cañizales, C., Baronchelli, L., et al. 2015, ApJ, 807, 149

Krolik, J. H., & Begelman, M. C. 1988, ApJ, 329, 702

Läsker, R., Greene, J. E., Seth, A., et al. 2016, ApJ, 825, 3

Lena, D. 2014, ArXiv e-prints, arXiv:1409.8264

Lena, D., Robinson, A., Storchi-Bergmann, T., et al. 2016, MNRAS, 459, 4485

Lena, D., Robinson, A., Storchi-Bergman, T., et al. 2015, ApJ, 806, 84

Levenson, N. A., Heckman, T. M., Krolik, J. H., Weaver, K. A., & Życki, P. T. 2006, ApJ, 648, 111

Li, J., Ostriker, J., & Sunyaev, R. 2013, ApJ, 767, 105

Lin, C. C., & Shu, F. H. 1964, ApJ, 140, 646

Lin, L.-H., Taam, R. E., Yen, D. C. C., Muller, S., & Lim, J. 2011, ApJ, 731, 15

Lindblad, B. 1964, Astrophysica Norvegica, 9, 103

Lindblad, P. A. B., Lindblad, P. O., & Athanassoula, E. 1996, A&A, 313, 65

Lindblad, P. O., & Lindblad, P. A. B. 1994, in Astronomical Society of the Pacific Conference Series, Vol. 66, Physics of the Gaseous and Stellar Disks of the Galaxy, ed. I. R. King, 29

Lynden-Bell, D. 1969, Nature, 223, 690

Madau, P., & Dickinson, M. 2014, ARA&A, 52, 415

Madejski, G., Życki, P., Done, C., et al. 2000, ApJ, 535, L87

Maiolino, R., Gallerani, S., Neri, R., et al. 2012, MNRAS, 425, L66

Maksym, W. P., Fabbiano, G., Elvis, M., et al. 2017, ApJ, 844, 69

Marconi, A., & Hunt, L. K. 2003, ApJ, 589, L21

Marconi, A., Oliva, E., van der Werf, P. P., et al. 2000, A&A, 357, 24

Markwardt, C. B. 2009, in Astronomical Society of the Pacific Conference Series, Vol. 411, Astronomical Data Analysis Software and Systems XVIII, ed. D. A. Bohlender, D. Durand, & P. Dowler, 251

Martin, D. C., Wyder, T. K., Schiminovich, D., et al. 2007, ApJS, 173, 342

Martini, P., Dicken, D., & Storchi-Bergmann, T. 2013, ApJ, 766, 121

Martini, P., & Pogge, R. W. 1999a, AJ, 118, 2646

—. 1999b, AJ, 118, 2646

McMullin, J. P., Waters, B., Schiebel, D., Young, W., & Golap, K. 2007, in Astronomical Society of the Pacific Conference Series, Vol. 376, Astronomical Data Analysis Software and Systems XVI, ed. R. A. Shaw, F. Hill, & D. J. Bell, 127

McNamara, B. R., Bîrzan, L., Rafferty, D. A., et al. 2008, in Astronomical Society of the Pacific Conference Series, Vol. 386, Extragalactic Jets: Theory and Observation from Radio to Gamma Ray, ed. T. A. Rector & D. S. De Young, 311

McNamara, B. R., & Nulsen, P. E. J. 2012, New Journal of Physics, 14, 055023

Meyer, M. J., Zwaan, M. A., Webster, R. L., et al. 2004, MNRAS, 350, 1195

Miller, J. S., & Antonucci, R. R. J. 1983, ApJ, 271, L7

Moorwood, A. F. M., van der Werf, P. P., Kotilainen, J. K., Marconi, A., & Oliva, E. 1996, A&A, 308, L1

Morganti, R., Oosterloo, T., & Tadhunter, C. N. 2005a, in Astronomical Society of the Pacific Conference Series, Vol. 331, Extra-Planar Gas, ed. R. Braun, 361

Morganti, R., Tadhunter, C., Oosterloo, T., Holt, J., & Emonts, B. 2007, in Astronomical Society of the Pacific Conference Series, Vol. 373, The Central Engine of Active Galactic Nuclei, ed. L. C. Ho & J.-W. Wang, 343

Morganti, R., Tadhunter, C. N., & Oosterloo, T. A. 2005b, A&A, 444, L9

Muñoz-Vergara, D., Nagar, N. M., Ramakrishnan, V., et al. 2019, MNRAS, 487, 3679

Müller-Sánchez, F., Prieto, M. A., Hicks, E. K. S., et al. 2011, ApJ, 739, 69

Mundell, C. G., & Shone, D. L. 1999, MNRAS, 304, 475

Nesvadba, N. P. H., Lehnert, M. D., Eisenhauer, F., et al. 2006, ApJ, 650, 693

Osterbrock, D. E. 1989, Astrophysics of gaseous nebulae and active galactic nuclei

Ott, M., Whiteoak, J. B., Henkel, C., & Wielebinski, R. 2001, A&A, 372, 463

Paturel, G., Theureau, G., Bottinelli, L., et al. 2003, A&A, 412, 57

Pounds, K. A., Reeves, J. N., King, A. R., et al. 2003, MNRAS, 345, 705

Puccetti, S., Comastri, A., Fiore, F., et al. 2014, ApJ, 793, 26

Ramos Almeida, C., Martínez González, M. J., Asensio Ramos, A., et al. 2016, MNRAS, 461, 1387

Rees, M. J. 1984, ARA&A, 22, 471

Riffel, R. A. 2010, Ap&SS, 327, 239

Riffel, R. A., Storchi-Bergmann, T., & Riffel, R. 2014, ApJ, 780, L24

—. 2015, MNRAS, 451, 3587

Riffel, R. A., Storchi-Bergmann, T., Winge, C., & Barbosa, F. K. B. 2006, MNRAS, 373, 2

Salpeter, E. E. 1964, ApJ, 140, 796

Sanders, D. B., Soifer, B. T., Elias, J. H., et al. 1988, ApJ, 325, 74

Schmitt, H. R., Antonucci, R. R. J., Ulvestad, J. S., et al. 2001, ApJ, 555, 663

Schmitt, H. R., Donley, J. L., Antonucci, R. R. J., Hutchings, J. B., & Kinney, A. L. 2003, ApJS, 148, 327

Schmitt, H. R., & Kinney, A. L. 1996, ApJ, 463, 498

Schnorr-Müller, A., Storchi-Bergmann, T., Nagar, N. M., Robinson, A., & Lena, D. 2017, MNRAS, 471, 3888

Schnorr-Müller, A., Storchi-Bergmann, T., Nagar, N. M., et al. 2014, MNRAS, 437, 1708

Schnorr-Müller, A., Storchi-Bergmann, T., Robinson, A., Lena, D., & Nagar, N. M. 2016, MNRAS, 457, 972

Schödel, R., Ott, T., Genzel, R., et al. 2002, Nature, 419, 694

Schoenmakers, R. H. M., Franx, M., & de Zeeuw, P. T. 1997a, MNRAS, 292, 349

—. 1997b, MNRAS, 292, 349

Schwarz, M. P. 1981, ApJ, 247, 77

Sellwood, J. A. 1981, A&A, 99, 362

Sellwood, J. A., & Wilkinson, A. 1993, Reports on Progress in Physics, 56, 173

Sheth, K., Regan, M. W., Scoville, N. Z., & Strubbe, L. E. 2003, ApJ, 592, L13

Shlosman, I., Begelman, M. C., & Frank, J. 1990, Nature, 345, 679

Shlosman, I., Frank, J., & Begelman, M. C. 1989, Nature, 338, 45

Silk, J., & Nusser, A. 2010, ApJ, 725, 556

Silk, J., & Rees, M. J. 1998, A&A, 331, L1

Simões Lopes, R. D., Storchi-Bergmann, T., de Fatima Saraiva, M., & Martini, P. 2007, ApJ, 655, 718

Slater, R., Nagar, N. M., Schnorr-Müller, A., et al. 2019, A&A, 621, A83

Springel, V., Di Matteo, T., & Hernquist, L. 2005, MNRAS, 361, 776

Storchi-Bergmann, T., Dors, Jr., O. L., Riffel, R. A., et al. 2007a, ApJ, 670, 959

—. 2007b, ApJ, 670, 959

Storchi-Bergmann, T., Lopes, R. D. S., McGregor, P. J., et al. 2010, MNRAS, 402, 819

Strateva, I., Ivezić, Ž., Knapp, G. R., et al. 2001, AJ, 122, 1861

Treister, E., Schawinski, K., Urry, C. M., & Simmons, B. D. 2012, ApJ, 758, L39

Treu, T., Ellis, R. S., Liao, T. X., & van Dokkum, P. G. 2005, ApJ, 622, L5

Valdes, F., Gupta, R., Rose, J. A., Singh, H. P., & Bell, D. J. 2004, ApJS, 152, 251

van Dokkum, P. G., Franx, M., Förster Schreiber, N. M., et al. 2004, ApJ, 611, 703

Vergara, D. M., Nagar, N. M., Ramakrishnan, V., et al. 2019, MNRAS, 1476

Véron-Cetty, M.-P., & Véron, P. 2003, A&A, 412, 399

Wada, K. 1994, PASJ, 46, 165

—. 2012, ApJ, 758, 66

Wagner, A. Y., & Bicknell, G. V. 2011, ApJ, 728, 29

Wagner, A. Y., Bicknell, G. V., & Umemura, M. 2012, ApJ, 757, 136

Webster, B. L., Goss, W. M., Hawarden, T. G., Longmore, A. J., & Mebold, U. 1979, MNRAS, 186, 31

Wong, T., Blitz, L., & Bosma, A. 2004, ApJ, 605, 183

Yates, M. G., Miller, L., & Peacock, J. A. 1989, MNRAS, 240, 129

Young, S., Axon, D. J., Robinson, A., Hough, J. H., & Smith, J. E. 2007, Nature, 450, 74

Yu, Q., & Tremaine, S. 2002, MNRAS, 335, 965

Zheng, X. Z., Bell, E. F., Somerville, R. S., et al. 2009, ApJ, 707, 1566

Ziegler, B. L., Thomas, D., Böhm, A., et al. 2005, A&A, 433, 519